Turbulence Measurements in Flows with Particles

Lagrangian Particle Tracking and a Robust Hot-Wire for Environmental Measurements.

Dissertation

for the award of the degree
“Doctor rerum naturalium"
at the Georg-August-Universität Göttingen

within the doctoral degree programme
Physics of Biological and Complex Systems
of the Göttingen Graduate School of Neurosciences, Biophysics, and
Molecular Biosciences (GGNB)
of the Georg-August University School of Sciences (GAUSS)

submitted by

Antonio Ibáñez Landeta
from Santiago, Chile
Göttingen, 2021

Thesis Committee

Prof. Dr. Dr. h.c. Eberhard Bodenschatz
Max-Planck-Institut für Dynamik und Selbstorganisation
Georg-August-Universität Göttingen

Prof. Dr. Andreas Janshoff
Institut für Physikalische Chemie
Georg-August-Universität Göttingen

Prof. Dr. Konrad Samwer
I. Physikalisches Institut
Georg-August-Universität Göttingen

Members of the Examination board

Referee: Prof. Dr. Dr. h.c. Eberhard Bodenschatz
Max-Planck-Institut für Dynamik und Selbstorganisation
Georg-August-Universität Göttingen

2^{nd} Referee: Andreas Dillman
Deutsches Zentrum für Luft- und Raumfahrt
Georg-August-Universität Göttingen

Other Members of the Examination Board

Prof. Dr Andreas Janshoff
Institut für Physikalische Chemie
Georg-August-Universität Göttingen

Prof. Dr. Konrad Samwer
I. Physikalisches Institut
Georg-August-Universität Göttingen

Prof. Dr. Ulrich Parlitz
Biomedical Physics Group
Max-Planck-Institut für Dynamik und Selbstorganisation

Prof. Dr. Stefan Klumpp
Institut für Dynamik komplexer Systeme
Georg-August-Universität Göttingen

Abstract

Despite the ubiquity of turbulent flows in nature, a general solution to the governing equations of motion remain elusive. These equations are nonlinear and nonlocal, and they describe a chaotic system with multi-scale characteristics, making its theoretical analysis difficult. One viable way of investigating high Reynolds number turbulence is by experimental methods, either in laboratory conditions or environmental measurements. The latter, however, are difficult. In one hand, environmental flows have a high Taylor scale Reynolds number ($\geq$ 10000) with a high mean velocity flow. This demands a high temporal and spatial resolution anemometer in order to adequately observe the smaller scales. High resolution anemometers, however, require very specific conditions to operate or are very delicate, being able to break even if a sand particle collides with them. These characteristics are in direct opposition to the uncontrolled, particle laden environmental conditions usually found in several types of flows of interest (e.g. inside ice clouds and sandstorms). Laboratory setups offer a viable alternative, albeit at a reduced turbulence intensity. For example, the Max Planck Variable Density Turbulence Tunnel (VDTT) allows for turbulent flows of Taylor scale Reynolds number $\mathrm{Re}_\lambda \sim 6000$ [1]. This Re_λ is generated by an active grid and kinematic viscosity tuning of the working gas achieved by changing the operating pressure. This allows great flexibility at modulating the turbulence over a wide and continuous range of Re_λ values. This setup, in particular, offers the possibility of not only obtaining single point Eulerian statistics, but also to obtain high Re Lagrangian statistics via particle tracking, which cannot be easily performed on atmospheric conditions. This allows not only to complement and corroborate atmospheric Eulerian statistics with more controlled experiments in laboratory, but also to study Lagrangian statistics (which is a field with much less experimental data available) and to analyze certain properties of the VDTT, such as its isotropy.

In this thesis, a novel hot-wire sensor which uses a carbon nanotube based material as its sensing element is developed and tested. This device shows

a frequency response larger than 20kHz, as well as superior mechanical resistance when compared to conventional Pt-tungsten anemometers of similar dimensions. This would allow the acquisition of high resolution Eulerian statistics on a wide range of environmental flows previously inaccessible due to technological constraints. This thesis also shows, as a separate chapter, the improvements performed on the already existing Lagrangian particle tracking (LPT) setup on the VDTT. The system has been improved to have a Stokes number 4 times smaller than the previous iteration. This thesis also demonstrates, by two independent but complementary methods, that the particles in the system are not electrostatically charged, but inertial. By comparing the Eulerian statistics obtained from both LPT and a pre-existing hot-wire statistics database [2], it was found that the turbulence intensity from LPT is consistently lower than before, pointing to the existence of sampling biases. A measure of the anisotropy of the system is measured from the LPT statistics, and it is found that the flow is mostly isotropic, even at the inertial range.

Contents

List of Tables

List of Figures

Chapter 1

Introduction

1.1 Motivation

Turbulence is an ever present phenomenon in life: smoke coming out of a chimney, the water flow on a strong river or the vigorous shaking of an airplane. It is also a very evocative term: the mere mention of turbulence makes the listener imagine irregular, chaotic flows with one or more eddies. However, despite its ease of qualitative description and being an apparent ubiquitous phenomena, as of yet there is no general theory of turbulence that fully describes its behavior and structure [3]. The classic way to determine whether a flow is turbulent first appeared in 1883, and it is the Reynolds Number.

Reynolds Number

The Reynolds number was first defined by Osborne Reynolds [4], as he observed the shape of a water flow on a glass pipe of diameter D by means of a small ink injection system. By controlling both the velocity of the flow U (with a valve) and the viscosity of the water ν (by changing its temperature) Reynolds defined a dimensionless number based on these experimental parameters with an associated critical value. This value separates the region where the flow on his experiment would transition from a predictable, smooth laminar behavior to a turbulent one. This quantity, now known as the Reynolds number, is defined as:

$$\mathrm{Re} = \frac{UD}{\nu} \tag{1.1}$$

While this critical value depends on the geometry of the phenomena studied, it exists for every type of flow. This hints to something that will be

shown later in this thesis: the Reynolds number is the relevant parameter in the equation of motion that governs incompressible Newtonian fluids.

1.1.1 Relevance of Turbulence

As mentioned before, turbulence is a phenomena which can be found in a wide range of flows. It can be a hint of heart disease [5]. Turbulence appears in engineering as one of the main contributors of mixing different elements, and therefore being relevant in, for example, understanding combustion processes [6]. It is also a relevant factor in both the energy yield of wind turbines [7] [8] and its mechanical stability [9].

The atmosphere itself is a fluid in permanent turbulent motion. Turbulence is one of the largest uncertainties in climate prediction due to its not yet fully quantified effect on cloud droplet growth [10], having a direct impact on the yearly rainfall and the earth energy budget.

Environmental flows

In the previous section, some examples were given that emphasize the relevance of turbulence in nature, making it an important field of study. Measuring environmental turbulence such as the atmospheric one is, however, not straightforward. The flow clouds move in is different from the flow normally found close to the surface of the earth, as the latter is dominated by the boundary layer effects. This results in different statistics when compared to the free-shear turbulence found in the upper atmosphere. Thus, the experiments have been designed to be realized as separated as possible from the surface. Some examples include measuring on tall antenna-like structures [11], atop tall mountains [12], in a measuring platform on a tethered balloon [13], drones and airplanes [14], among others. Measuring in these conditions, however, is challenging. In order to resolve the small scales of turbulence, a sub millimetric spatial resolution, coupled with high frequency (of more than ~ 10 kHz) is required.

The problem is further constricted by the need to protect the sensible electronic devices from harsh weather conditions or the many micrometric to millimetric particles carried by the atmosphere, such as pollen, ice, and dust, among others. Several different types of anemometers exist, with their own advantages and disadvantages. Examples include mechanical anemometers, supersonic anemometers, hot-wire anemometry, pressure anemometers and light-based anemometry such as laser doppler velocimetry and particle image

velocimetry. Devices like supersonic anemometers, mechanical anemometers and Pitot tubes have a low time resolution, no larger than 20 Hz[15] which is not fast enough to resolve the finer scales of turbulence. Faster and more accurate devices, such as laser doppler velocimetry or particle image velocimetry are an alternative. However,they require a complex, expensive and delicate setup which is not well suited for field campaigns.

Another disadvantage of these techniques is that they require the introduction of tracer particles in the flow, with the corresponding environmental and material costs as well as unsuitability for long-term measurements. In comparison hot-wires are a cheaper, simpler alternative with a frequency response is on the order of 10 kHz, making them a suitable candidate. High resolution hot-wires, however, depend on a thin wire, with a thickness of at most a few micrometers to operate. This makes them susceptible to failure, as they would be operating on a flow laden with particles that can be millimetric in size. On this front, one of the best prospects is the nano scale thermal anemometry probe (NSTAP,) a micromachined hot-wire with a free standing sensing element of pure Pt of length 30 – 60 μm and thickness 100 nm [16]. While their small size ensures both a fast response and a very low chance of particle impingement due to their small cross-section [17], they are both not straightforward to manufacture and very delicate, which makes their handling and operation difficult. It is desired, then, to have a reliable, robust anemometry probe with an adequate temporal and space resolution for environmental measurements in harsh conditions.

Laboratory flows

The alternative to measuring flows in nature is to do either laboratory experiments or simulations. In order to properly compare turbulence in nature and in an experiment or simulation, a scale-independent version of Equation (1.1) is required. This is the Taylor-scale Reynolds number Re_λ, defined by the R.M.S velocity, the kinematic viscosity of the fluid and the Taylor length scale λ [18]. The length scale λ is defined as function of the velocity autocorrelation function, but it is easier to understand as the smallest eddy in the flow that it is not strongly affected by viscous forces. Of note is the fact that this length scale only makes sense when the large-scale phenomena is sufficiently distinct from the smallest possible eddy.

The characteristic Re_λ of the atmosphere is $\mathrm{Re}_\lambda \sim 10^4$ [19]. Current high resolution DNS can only reach $\mathrm{Re}_\lambda \approx 1300$ [20] [21] [22], which means they are not ideal to study atmospheric-like flows. This motivates the design and

construction of experimental setups able to generate high Re, free shear laboratory flows. These setups, however, are challenging: as $Re \sim \frac{L}{\nu}$ the experimental setup must either be very large, minimize ν or a combination of both. Small setups usually rely on using a fluid with a very low kinematic viscosity ν, which allows the existence of tiny eddies, such as liquid helium turbulence experiments [23]. Minimizing ν, however, poses a different challenge: These experiments can reach $\mathrm{Re}_\lambda = 20000$ [24] but measuring the smaller scales η can be difficult, as $\eta \sim 10\mu$m. Also, while allowing to study high Reynolds number turbulence, performing these measurements at the operating temperature (1.6 – 5 K) is both a difficult and expensive endeavor [25] [26].

On larger experiments, the forefront in terms of costs and range of Re_λ for isotropic turbulence are the wind tunnel experiments. The wind tunnel studied on this thesis is the Max Planck Variable Density Turbulence Tunnel (VDTT), which offers a versatile range of Taylor scale Reynolds number, going from $\mathrm{Re}_\lambda \approx 700$ to $\mathrm{Re}_\lambda \approx 6000$ according to a previous study performed by C. Kuechler et. al [2]. While their work includes a very detailed analysis on hot-wire data, as well as the implementation of a Lagrangian particle tracking (LPT) setup, for the latter only exploratory measurements were taken, being more akin to a proof of concept. Furthermore, on this LPT setup, only high Stokes number ($\mathrm{St} > 1$) particles could be used, which means that accurate turbulent flow statistics could not be obtained. A comprehensive Lagrangian dataset of the turbulent flow is necessary not only to complement the already existing Eulerian dataset, but also because (to the best of the author's knowledge) there is no other setup yet capable of producing Lagrangian data at the operating Re of the VDTT.

In summary, in order to measure environmental flows, a suitable measurement device is required. This device should have a high spatial ($\geq$ 1mm) and temporal ($\sim$ 10kHz) resolution. Furthermore, they should be able to withstand rough atmospheric flows. The obtained atmospheric measurements should be complemented with precise 3D laboratory measurements at similarly Re_λ values.

1.2 This thesis

The work in this thesis is framed under the measurement of atmospheric or atmospheric-like flows. It is structured in four chapters.

Chapter 1 (this chapter) corresponds to the introduction. In the following sections, a brief introduction on the necessary theory to understand this work

is presented. This includes the equations of motions of a fluid, some statistical quantities and properties of turbulent flows and the characteristic time-scale of a particle flow.

Chapter 2 is centered on the design, construction and testing of an easy to manufacture, fast hot-wire which is able to withstand harsh environmental conditions. This hot-wire is both compatible with existing, commercially available electronic driving systems and has a frequency response comparable to that of commercially available, more fragile sensors of similar characteristics.

Chapter 3 focuses on the acquisition of high turbulence data in the VDTT via Lagrangian particle tracking (LPT). In order to accomplish this, the already existing LPT setup was modified in order to be able to operate with smaller particles that better capture the flow dynamics. From the resulting position vs time data, the velocity statistics were obtained and compared with previously acquired hot-wire measurements

Chapter 4 presents the conclusions of the results obtained in the previous two chapters, as well as offering a summary and a brief outlook.

1.3 Fundamentals

This section consists of general turbulent theory which is the basis of the theory presented and discussed in subsequent chapters. This is, for the most part, a summary of the first and sixth chapter of the book written by Pope [27], although a similar introduction can be found in any other introductory book for fluid mechanics.

1.3.1 On the continuity of a flow

When observing a fluid in motion, there are some basic assumptions to be made: The most elementary one is that the fluid is a continuous substance instead of a collection of many discrete particles. While by now it is well known that this is not true, for many interesting physical phenomena this assumption works extremely well for finding equations that neatly describe them, as there is a clear separation of scales between the very small phenomena and the typical small scales involved in a turbulent flow. For example, the distance an air molecule can travel before colliding with another one (the mean free path) at a pressure of 1 atmosphere and a temperature of $T = 300K$ is $\mathrm{M}_{fp} \approx 65\mathrm{nm}$. In comparison, the smallest swirl (or eddy) which can be found in a cloud would have a size of $\eta \approx 500\mu\mathrm{m}$. If there is a very large separation between the two scales, that is, if $\mathrm{L} \gg \mathrm{M}_{fp}$, it is possible to "forget" the particularities of molecular properties at large scales, and instead consider the expectation value of these properties. The separation of these scales is described by the Knudsen number Kn, which is defined as:

$$\mathrm{Kn} = \frac{M_{fp}}{L}. \tag{1.2}$$

Where L is a characteristic scale of the phenomena that it is studied. It is said that, if $Kn < 1 \cdot 10^{-2}$ the fluid, as well as and all of its associated properties, can be assumed to be continuous for the whole position field domain. In the previous example $Kn = 1.3 \cdot 10^{-4}$, which places atmospheric phenomena well into the continuous regime.

1.3.2 Eulerian and Lagrangian fields

There are two ways to measure changes in properties of a moving fluid: One possibility is to define a stationary frame and measure from a fixed point in space. One example would be when measuring the wind velocity on a

classic cup anemometer. In this example, the velocity $\vec{U}(\vec{x}, t)$ evolves only as a function of time, as $\vec{x} = \vec{x}_0$ is fixed in space and corresponds to the position of the anemometer. This reference frame, which assumes a static observer or, equivalently, a fixed control volume in space is called an Eulerian frame of reference.

An alternative way of measuring would be to instead follow a particular air parcel, or a very small tracer (e.g. a smoke particle [28]). This small parcel is, by definition, a point that moves with the local fluid velocity. It is possible to define $\vec{r}^L(t, r_0)$ the position the at time t of this small parcel that, at time t_0, was located at position r_0. The position of this *fluid particle* is defined by the following equations:

$$\vec{r}^L(t_0, r_0) = r_0 \tag{1.3}$$

$$\vec{U}^L(t, r_0) = \frac{\partial \vec{r}^L}{\partial t}(t, r_0) \tag{1.4}$$

This is known as the Lagrangian frame. As both Lagrangian and Eulerian frames describe the same properties, transformation relations between the two of them must exist. In the case of the Lagrangian velocity field $\vec{U}^L$:

$$\vec{U}^L(t, r_0) = \vec{U}(\vec{r}^L(t, r_0), t) \tag{1.5}$$

Note that $\vec{U}^L$ is not indexed by the current position of the fluid particle $\vec{r}^L$ but by its position r_0 at the reference time t_0. For a fixed r_0, $\vec{r}^L$ defines a trajectory known as the fluid particle path. Its partial derivative would correspond to the rate of change of velocity at fixed $\vec{r}_0$, that is, the acceleration of the fluid parcel labelled by $\vec{r}_0$. From Equation 1.5

$$\begin{aligned}
\frac{\partial \vec{U}}{\partial t}(\vec{r}^L(t, r_0), t) &= \frac{\partial \vec{U}}{\partial t}(\vec{r}^L(t, r_0), t) \\
&= \frac{\partial \vec{U}}{\partial t}(\vec{r}, t)\bigg|_{\vec{r}=\vec{r}^L(t,\vec{r}_0)} + \frac{\partial \vec{r}^L}{\partial t}(t, r_0) \left(\frac{\partial \vec{U}}{\partial \vec{r}}(\vec{r}, t) \right)_{\vec{r}=\vec{r}^L(t,\vec{r}_0)} \\
&= \left(\frac{\partial \vec{U}}{\partial t}(\vec{r}, t) + \vec{U} \cdot \frac{\partial \vec{U}}{\partial \vec{r}}(\vec{r}, t) \right)_{\vec{r}=\vec{r}^L(t,\vec{r}_0)} \\
&= \frac{D}{Dt}\vec{U}(\vec{r}^L, t)
\end{aligned} \tag{1.6}$$

Where the material derivative $\frac{D}{Dt}$ is defined as:

$$\frac{D}{Dt} = \frac{\partial}{\partial t} + U_i \frac{\partial}{\partial r_i} = \frac{\partial}{\partial t} + \vec{U} \cdot \nabla \tag{1.7}$$

Thus, the acceleration of the fluid parcel is given by the partial time derivative of the Lagrangian velocity field and by the material derivative of the Eulerian velocity field ($\frac{D}{Dt}\vec{U}$). Note that no special properties of the velocity field was used on Equation (1.6), therefore this analysis is applicable to any quantity measured.

1.3.3 Navier-Stokes equation

By Newton's second law, the rate of change of momentum an infinitesimal part of the fluid is equal to the total sum of forces $\vec{\sigma}$. In mathematical terms, one analyzes the continuity of the momentum density $\rho\vec{U}$:

$$\begin{aligned}
\frac{\partial(\rho U_i)}{\partial t} + \frac{\partial(\rho U_i U_j)}{\partial x_j} &= \sigma_i \\
U_i \frac{\partial \rho}{\partial t} + \rho \frac{\partial U_i}{\partial t} + U_j \rho \frac{\partial U_i}{\partial x_j} + U_i U_j \frac{\partial \rho}{\partial x_j} + \rho U_i \frac{\partial U_j}{\partial x_j} &= \sigma_i \\
U_i \left(\frac{\partial \rho}{\partial t} + U_j \frac{\partial \rho}{\partial x_j} + \rho \frac{\partial U_j}{\partial x_j} \right) + \rho \left(\frac{\partial U_i}{\partial t} + U_j \frac{\partial U_i}{\partial x_j} \right) &= \sigma_i \\
U_i \left(\frac{\partial \rho}{\partial t} + \frac{\partial(\rho U_j)}{\partial x_j} \right) + \rho \left(\frac{\partial U_i}{\partial t} + U_j \frac{\partial U_i}{\partial x_j} \right) &= \sigma_i
\end{aligned} \tag{1.8}$$

Where Einstein's notation is used. The first term corresponds to the continuity equation, which follows:

$$\frac{\partial \rho}{\partial t} + \frac{\partial(\rho U_i)}{\partial x_j} = 0, \tag{1.9}$$

as mass is a conserved quantity. Thus, Equation (1.8) reduces to:

$$\rho \left(\frac{\partial U_i}{\partial t} + U_j \frac{\partial U_i}{\partial x_j} \right) = \sigma_i. \tag{1.10}$$

The forces of interest in this thesis, and therefore contribute to σ_i, can be either shear stresses, which stem from molecular interactions in the fluid, or body forces applied to the whole fluid, like gravity. In the same way gravity can be expressed as the gradient of a potential, the shear stresses can be represented as a vectorial derivative of an order 2 tensor, which is aptly named stress tensor τ. In a Newtonian fluid (like air or SF_6), the stress tensor

depends on both the (constant) fluid dynamic viscosity μ, having the shape:

$$\tau_{ij} = \mu \left(\frac{\partial U_i}{\partial x_j} + \frac{\partial U_j}{\partial x_i} \right) \tag{1.11}$$

As mentioned before, the shear stress applied on the direction i would be the gradient of τ in that direction, that is:

$$f_i^{stress} = \frac{\partial \tau_{ij}}{\partial x_j} \tag{1.12}$$

On the other hand, external forces (such as gravity) apply to the fluid in the form of a pressure exerted over a certain area:

$$F = \oiint_{\vec{A}} P d\vec{A} = \int_V -\nabla P dV \tag{1.13}$$

Where the divergence theorem has been used to re-write the surface integral as a volume integral. By combining Equation (1.13) with Equations (1.12) and (1.10), the Navier-Stokes equation is obtained:

$$\frac{\partial U_i}{\partial t} + U_j \frac{\partial U_i}{\partial x_j} = -\frac{1}{\rho} \frac{\partial P}{\partial x_i} + \nu \left(\frac{\partial^2 U_i}{\partial x_i \partial x_j} + \frac{\partial^2 U_i}{\partial x_j \partial x_j} \right) \tag{1.14}$$

Where $\nu = \frac{\mu}{\rho}$ is the kinematic viscosity of the fluid. From Equation (1.9), it is possible to obtain:

$$\begin{aligned} \frac{\partial \rho}{\partial t} + U_i \nabla_i \rho &= -\rho \nabla_i \cdot U_i \\ \frac{1}{\rho} \left(\frac{D\rho}{Dt} \right) &= \nabla \cdot U \end{aligned} \tag{1.15}$$

If the fluid is incompressible $\frac{D\rho}{Dt} = 0$, which means $\nabla \cdot U = 0$ and the fluid is solenoidal as well. In this case, Equation (1.14) simplifies to:

$$\frac{\partial U_i}{\partial t} + U_j \frac{\partial U_i}{\partial x_j} = -\frac{1}{\rho} \frac{\partial P}{\partial x_i} + \nu \frac{\partial^2 U_j}{\partial x_j \partial x_j} \tag{1.16}$$

It is possible to define $u(\vec{r}) = \vec{U} - \left\langle \vec{U} \right\rangle$ the turbulent fluctuations term. Since $\frac{\partial \langle \vec{U} \rangle}{\partial x_i} = \frac{\partial \langle \vec{U} \rangle}{\partial t} = 0$, the turbulent fluctuations term satisfies the Navier Stokes equation (1.16) and will have the same statistics of $\vec{U}$

1.3.4 Energy

Equation (1.16) is, essentially, a force balance. By multiplying this equation by u_i, it is possible to obtain an equation for the infinitesimal energy rate (per time unit):

$$\begin{aligned} u_i \frac{\partial u_i}{\partial t} + u_i u_j \frac{\partial u_i}{\partial x_j} &= -\frac{1}{\rho}\frac{\partial P}{\partial x_i} u_i + \frac{\mu}{\rho} u_i \frac{\partial^2 u_j}{\partial x_i \partial x_i} \\ \frac{\partial \frac{u_i^2}{2}}{\partial t} + u_j \frac{\partial \frac{u_i^2}{2}}{\partial x_j} &= -\frac{1}{\rho}\frac{\partial P}{\partial x_i} u_i + \frac{\partial}{\partial x_i} u_j \frac{\tau_{ij}}{\rho} - 2\nu \frac{\partial u_i}{\partial x_j}\frac{\partial u_i}{\partial x_j} \end{aligned} \tag{1.17}$$

All terms on Equation (1.17) can be identified. From left to right, these terms correspond to:

- Evolution of the kinetic energy as a function of time,
- Convection of the kinetic energy at the boundary of the control volume,
- Deformation of the boundary due to pressure forces,
- Interaction between boundaries of adjacent control volumes due to viscous forces,
- dissipation of energy into heat.

It is noted that only the last term on (1.17) is a dissipative term. This motivates the definition of the energy dissipation rate ϵ as:

$$\epsilon = 2\nu \left\langle \frac{\partial u_i}{\partial x_j}\frac{\partial u_i}{\partial x_j} \right\rangle, \tag{1.18}$$

where the brackets $\langle \cdot \rangle$ denote a spatial average.

1.4 Pressure

On the previous section, the body forces applied on the fluid have been collected in the variable P, which is named pressure. This means that the pressure P is different from the pressure defined by thermodynamics. In order to understand what P is, one takes the divergence of Equation (1.14), obtaining:

$$\frac{DG}{Dt} - \nu \frac{\partial^2 G}{\partial x_j \partial x_j} = -\frac{1}{\rho} \frac{\partial^2 P}{\partial x_j \partial x_j} - \frac{\partial U_i}{\partial x_j} \frac{\partial U_j}{\partial x_i} \tag{1.19}$$

For $G = \frac{\partial U_i}{\partial x_i}$. If we consider the fluid to be incompressible, $G = 0$. This, in turn, means that:

$$\frac{\partial^2 P}{\partial x_j \partial x_j} = -\rho \frac{\partial U_i}{\partial x_j} \frac{\partial U_j}{\partial x_i} \tag{1.20}$$

P satisfies the Poisson equation, and can be solved using the Green's function:

$$P(x) = \frac{\rho}{4\pi} \iiint \frac{\partial U_i}{\partial x_j} \frac{\partial U_j}{\partial x_i} \frac{1}{|x - y|} dy \tag{1.21}$$

By replacing equation (1.21) on (1.16), it is possible to obtain a closed system. However, the equation is also nonlocal: if the fluid is incompressible, any force applied at one point will be felt by the entire flow.

1.4.1 Vorticity

As previously mentioned, one of the essential features of turbulents flows is the fact that they have eddies. This fluid rotation is quantified by the vorticity $\omega(x)$, defined as the curl of the velocity:

$$\omega(x) = \nabla \times \vec{U} \tag{1.22}$$

The equation that governs the time evolution of ω is obtained by taking the curl of equation (1.51):

$$\frac{D\omega}{Dt} = \nu \nabla^2 \omega + \omega \cdot \nabla \vec{U} \tag{1.23}$$

1.5 Turbulence statistics

This section lists some fundamental properties of the statistics of turbulent flows, as well as some statistical tools and hypotheses that will be used on this thesis.

1.5.1 The Energy Cascade and Kolmogorov's hypotheses

The concept of the energy cascade was first postulated by Richardson in 1922 [29]. He claimed that turbulence had a defined structure of large eddies (or whorls) of a characteristic length l_0 and characteristic velocity u_0, that break down into smaller ones (of characteristic length l_1 and velocity u_1). This generation of smaller and smaller eddies continues until a critical size, where viscosity dissipates the energy into heat. This simple description implies that, in any turbulent system, there is a "largest" eddy with characteristic size L. This eddy will break down, transferring its kinetic energy to smaller eddies at a rate ϵ. In this case, the relevant velocity for an eddy would be its R.M.S velocity u_0, which makes possible the definition of a timescale $\tau_L = \frac{L}{u_0}$, defined as the turnover time of the eddy. The total kinetic energy of this eddy would be of order u_0^2. Thus, it's possible to define the (constant) energy transfer rate (from largest to smaller) ϵ as:

$$\epsilon \sim \frac{u_0^2}{\tau_L} = \frac{u_0^3}{L} \tag{1.24}$$

This description of turbulence states that there is only one energy source, which corresponds to the energy source that is generating the largest structure of length L, which is injecting energy into the system at a rate of transfer ϵ. It also postulates that the only energy sink in the system is the conversion of eddies smaller than η into heat. It stands to reason that, once the system reaches a dynamic equilibrium, the energy rate of transfer ϵ has to be equal to the energy dissipation rate defined in Equation (1.18).

Kolmogorov further refined this description by his famous K41 theory [30]. It can be stated in the form of three hypotheses:

- **Local Isotropy and homogeneity** The small-scale turbulent motions ($l \ll L$) are statistically isotropic and homogeneous if sufficiently far away from any boundaries.

- **First similarity hypothesis** The statistics of the small-scale turbulence ($l \ll L$) are only governed by the kinematic viscosity ν and the energy dissipation rate ϵ.

- **Second similarity hypothesis** The statistics of the small-scale turbulence in the range $\eta \ll l \ll L$ (where η is the characteristic size of the scale where viscous dissipation is dominant) are only governed by ϵ, being independent of ν.

From the second hypothesis, by dimensional analysis, one can build three different quantities η, u_η and τ_η them being respectively length, velocity and time scales. These scales, named Kolmogorov scales are respectively:

$$\eta = \left(\frac{\nu^3}{\epsilon}\right)^{\frac{1}{4}} \tag{1.25}$$

$$u_\eta = (\epsilon\nu)^{\frac{1}{4}} \tag{1.26}$$

$$\tau_\eta = \left(\frac{\nu}{\epsilon}\right)^{\frac{1}{2}} \tag{1.27}$$

The Reynolds number defined by these scales is quite small:
$\mathrm{Re}_\eta = \frac{u_\eta \eta}{\nu} = 1$. As this is a small value of Re, the flow at these scales cannot be considered turbulent. This coincides with the statement given by Kolmogorov, that the smallest scale of the turbulent flow is proportional to η [31]. This result, alongside Kolmogorov's second similarty hypothesis postulates that, if η is small enough, there is an intermediate range between the smallest dissipation scales of order η and the largest scales L. This inertial range does not depend on the fluid viscosity or the flow geometry. By combining Equations (1.27) and (1.24), one obtains the following:

$$\begin{aligned}\frac{\eta}{L} &= \frac{(\frac{\nu^3}{\epsilon})^{1/4}}{L} \\ &\sim \left(\frac{\nu^3}{u_0^3 L^3}\right)^{1/4} \\ &\sim \mathrm{Re}^{-3/4}\end{aligned} \tag{1.28}$$

Which relates the smallest scales with the largest scales and the Reynolds number. This means that, if a flow has a high Re, the largest scale L will be very distinct from the smallest scales proportional to η, and so the inertial range can be easily identified. Conversely, it means that a large Re is achieved if $\eta \ll L$, and if one could decrease the value of η while keeping L constant, the flow would be more turbulent. This is characteristic used by all setups that use low viscosity fluids to generate high turbulence flows.

1.5.2 Second order structure function

The time averaged second order structure function $D_{ij}(r)$ is defined as the correlation function between the velocity at two points separated by a distance

$\vec{r}$, that is:

$$D_{ij}(\vec{r},\vec{x}) = \left\langle [u_i(\vec{x}+\vec{r}) - u_i(\vec{x})][u_j(\vec{x}+\vec{r}) - u_j(\vec{x})] \right\rangle . \tag{1.29}$$

For the next calculations, a turbulent flow with large Re is considered, where the Kolmogorov hypotheses of similarity, local isotropy and local homogeneity apply. For these conditions, Equation (1.29) becomes an isotropic function of r, being independent of $\vec{x}$. It is possible, then, to rewrite it as:

$$D_{ij}(r) = D_{NN}(r)\delta_{ij} + (D_{LL}(r) - D_{NN})\,\frac{r_i r_j}{r^2}, \tag{1.30}$$

where D_{LL} and D_{NN} are called, respectively, the longitudinal and transverse structure functions. If the coordinate system is redefined such that one of its axis (for example, $\hat{e}_1$) is aligned to the inter-particle distance vector, D_{ij} simplifies to:

$$D_{11} = D_{LL}, \tag{1.31}$$

$$D_{22} = D_{33} = D_{NN}, \tag{1.32}$$

$$D_{ij} = 0 \qquad \text{for } i \neq j. \tag{1.33}$$

In homogeneous turbulence with $\langle U \rangle = 0$, D_{NN} is determined by D_{LL} according to the following relation:

$$D_{NN}(r) = D_{LL}(r) + \frac{r}{2}\frac{\partial}{\partial r} D_{LL}(r). \tag{1.34}$$

As mentioned in Section 1.3.3, one can define $\vec{u} = \vec{U} - \left\langle \vec{U} \right\rangle$. $\vec{u}$ satisfies the condition necessary to use Equation (1.34) while having the same turbulent statistics that $\vec{U}$. Under these conditions, it is sufficient to study only the longitudinal component of the structure function to observe the complete structure function. This motivates the rewriting of the longitudinal structure function of order 2, S_2, as:

$$S_2(r) = \left\langle (u_1(x+r) - u_1(x))^2 \right\rangle , \tag{1.35}$$

where x can be any point in the measurement volume.

Power law relation for S_2

According to Kolmogorov's similarity hypotheses, if $\eta \ll r \ll L$, S_2 is independent of ν. By dimensional analysis, S_n has to be a law of the shape $(\epsilon r)^{n/3}$. For S_2, one obtains:

$$S_2(r) = C_2 \left(\epsilon r\right))^{2/3}, \tag{1.36}$$

with $C_2 \approx 2$ [27]

By combining equations (1.36) and (1.34), one arrives to the following relation:

$$D_{NN}(r) = \frac{4}{3} S_2(r). \tag{1.37}$$

Note that Equations (1.36) and (1.37) are only valid for statistically homogeneous isotropic turbulence.

1.5.3 Two-point velocity correlation

The two-point velocity correlation is defined as:

$$R_{ij}(\vec{x}, \vec{r}, t) = \left\langle u_i(\vec{x}, t) u_j(\vec{x} + \vec{r}, t) \right\rangle \tag{1.38}$$

And it is one of the simplest statistic that contains some information on the spatial structure of the random field. In the same way that the second order structure function can be decomposed into D_{LL} and D_{NN} (being L the direction of $\vec{r}$) if the turbulence is homogeneous and isotropic, the two-point correlation can be decomposed into a longitudinal component R_{11} and transverse components $R_{22} = R_{33}$ as well, and $R_{ij} = R_{11} + R_{22} + R_{33}$, with $R_{ij} = 0$.

1.5.4 The velocity-spectrum tensor

If the turbulence is homogeneous, the velocity-spectrum tensor is the Fourier transform of the two-point correlation vector R_{ij}

$$\Phi_{ij}(\vec{k}) = \frac{1}{2\pi^3} \int_{-\infty}^{\infty} R_{ij} \mathrm{e}^{-i\vec{k}\cdot\vec{r}} d\vec{r} \tag{1.39}$$

From (1.39) it follows that, for $\vec{r} = 0$:

$$R_{ij}(0) = \int_{-\infty}^{\infty} \Phi_{ij}(k) d\vec{k} = \left\langle u_i u_j \right\rangle \tag{1.40}$$

If the fluid is incompressible, then $k_i\Phi_{ij}(\vec{k}) = k_j\Phi_{ji}(\vec{k}) = 0$

1.5.5 The energy spectrum

The energy spectrum is defined as:

$$E(k) = \oint \frac{1}{2}\Phi_{ii}(\vec{k})dS(\vec{k}) \tag{1.41}$$

The integral over all $\vec{k}$ that have a magnitude $\|\vec{k}\| = k$. If the flow is isotropic and homogeneous, it can be demonstrated that:

$$\Phi_{ij}(\vec{k}) = \frac{E(k)}{4\pi k^2}\left(\delta_{ij} - \frac{k_i k_j}{k^2}\right) \tag{1.42}$$

One dimensional spectrum

In the scope of hot-wire measurements, which only measure one velocity component, the one dimensional spectrum $E_{ij}(k_1)$ is defined as two times the one dimensional Fourier transform of $R_{ij}(\hat{e_1}r_1)$

$$E_{ij}(k_1) = \frac{1}{\pi}\int_{-\infty}^{\infty} R_{ij}(\hat{e_1}r_1)\mathrm{e}^{-ik_1r_1}dr_1 \tag{1.43}$$

For example, for E_{11}:

$$\begin{aligned} E_{11}(k_1) &= \frac{1}{\pi}\int_{-\infty}^{\infty} R_{11}(\hat{e_1}r_1)\mathrm{e}^{-ik_1r_1}dr_1 \\ R_{11} &= \frac{1}{\pi}\int_{0}^{\infty} E_{11}(k_1)\cos(k_1r_1)dk_1 \end{aligned} \tag{1.44}$$

With these relations, and using Equation (1.39), it is possible to rewrite $E_{11}(k_1)$ as:

$$E_{11}(k_1) = 2\iint_{-\infty}^{\infty}\Phi_{11}(\vec{k})dk_2dk_3 \tag{1.45}$$

And, by combining with Equation (1.42):

$$\begin{aligned} E_{11}(k_1) &= \iint_{-\infty}^{\infty}\frac{E(k)}{2\pi k^2}\left(\delta_{ij} - \frac{k_1^2}{k^2}\right) \\ &= \int_{k_1}^{\infty}\frac{E(k)}{k}\left(1 - \frac{k_1^2}{k^2}\right)dk. \end{aligned} \tag{1.46}$$

Equation (1.46) can be inverted, which establishes a relation between the full energy spectrum of isotropic turbulence in terms of the one dimensional spectrum E_{11}. It is also possible, for isotropic flows, to relate the spectrum E_{11} with E_{22}

If the inertial range is considered, it is possible to find a power law relation for $E(k)$ using the Kolmogorov hypotheses and dimension analysis, in a way which is similar to the one used to obtain the power law for S_2. The spectrum scales with:

$$E = C\epsilon^{\frac{2}{3}}k^{-\frac{5}{3}} \tag{1.47}$$

With C being a (presumably) universal constant [32]. Provided that k is in the range $\eta^{-1} \ll k \ll L^{-1}$, this is an universal equation independent, up to a constant, of the flow properties. From Equations (1.46) and (1.47), it is easy to find the power law for E_{11}:

$$E_{11} = \frac{18}{55}C\epsilon^{\frac{2}{3}}k^{-\frac{5}{3}} \tag{1.48}$$

The constant $C_1 = \frac{18}{55}C$ is said to be ≈ 0.49 [27], which means $C \approx 1.5$.

1.5.6 Different expressions for the energy dissipation rate

If the turbulence if both isotropic and homogeneous, it is possible to rewrite Equation (1.18) as [33]:

$$\epsilon = 15\left\langle\left(\frac{\partial u_1}{\partial x_1}\right)^2\right\rangle \tag{1.49}$$

In spectral space, Equation (1.49) becomes [27]:

$$\epsilon = 15\int_0^\infty k_1^2 E_{11}(k_1)dk_1 \tag{1.50}$$

Equations (1.49) and (1.50), if the turbulence is both homogeneous and isotropic, allow the calculation of ϵ from experiments that only provide one dimensional velocity components, such as hot-wire measurements.

1.5.7 Reynolds Number

The Reynolds number presented in Equation (1.1) can also be deduced from the Navier Stokes equation (1.16). By transforming the variables to its

non-dimensional versions, defined by a characteristic length L and a velocity scale U:

$$\hat{x} = \frac{x}{L}$$
$$\hat{t} = \frac{tU}{L}$$
$$\hat{U} = \frac{\vec{U}}{U}$$
$$\hat{p} = \frac{P}{\rho U^2}$$

Equation (1.14) then simply becomes:

$$\frac{\partial \hat{U}_i}{\partial t} + \hat{U}_i \frac{\partial \hat{U}_i}{\partial \hat{x}_i} = \frac{1}{\mathrm{Re}} \frac{\partial^2 \hat{U}_i}{\partial \hat{x}_i \partial \hat{x}_i} - \frac{\partial \hat{p}}{\partial \hat{x}_j} \tag{1.51}$$

On this adimensional Navier Stokes equation, the only parameter is Re. This means that, if Reynolds experiment is repeated with two pipes with different diameters L_a and L_b but the flow velocities U_a and U_b are chosen in such a way that $Re_a = Re_b$ are the same, then the scaled velocity fields $\hat{U}$ would have the same governing equation. This justifies relating results obtained from experiments to different phenomena, as long as they have a similar Reynolds Number and border conditions for the equation system.

Taylor scale Reynolds number

As previously mentioned in Section 1.1, Taylor [18] first defined a length scale λ that permits the definition of a geometry independent Reynolds number Re_λ. Originally, Taylor defined this value over the correlation function, but a more practical definition is:

$$\lambda = \sqrt{\frac{u_{rms}^2}{(\frac{\partial u}{\partial x})^2}} = \sqrt{\frac{15 \nu u_{rms}^2}{\epsilon}}. \tag{1.52}$$

And the Taylor scale Reynolds number:

$$\mathrm{Re}_\lambda = \frac{\lambda u_{rms}}{\nu}, \tag{1.53}$$

where $\lambda = \sqrt{15 \frac{\nu}{\epsilon}} \langle u_{rms} \rangle$ is the Taylor microscale.

1.5.8 Taylor's frozen flow hypothesis

A wide range of devices (pressure anemometers, hot-wires, laser doppler anemometry, ultrasonic anemometers) measure velocity fluctuations in one point only as a function of time. However, the aim of these devices is to resolve the turbulence in a flow in space. This conundrum was solved by an approximation, first stated by Taylor [18]. If the mean flow $\left\langle \vec{U}(t) \right\rangle$ is much larger than the turbulent fluctuations $\sqrt{\langle u(t)^2 \rangle}$, where $u = \vec{U}(t) - \left\langle \vec{U}(t) \right\rangle$ and it is unidirectional $\left\langle \vec{U} \right\rangle = U\hat{e_1}$, then the one-point measurements are equivalent to that of a sensor moving at a velocity $V_s = -U\hat{e_1}$. In essence, the fluctuating part of the velocity is "frozen", and its being passively advected past the sensor. This allows to convert the variable t to a position variable $x = t \langle U \rangle$, and it is used in single point measurements (such as hot-wire anemometry) to convert time series to position series, which permits to analyse this data with all the mathematical tools listed in this section.

1.5.9 Intermittency

The K41 theory establishes η as a constant that is closely related to the smallest scales in turbulence. Further studies, however, found out that ϵ is not a constant, but instead an intermittent function of space and time [34] [33], which means that the proposed averages are but a simplification. Equation (1.18) relates the (averaged) ϵ with the square of the velocity gradient. As ϵ fluctuates, then the velocity gradients also fluctuate in time, and high velocity gradients must appear in the flow. As intermittency increases at larger Re, [35] [36], these extreme gradients also become larger.

1.6 Equation of motion of particles in a flow

A particle-laden flow can be seen as a two-phase flow, where one phase is made up of fluid while the other is made up of the movement of the immiscible, solid particles.
This is a coupled system where both fluid and particle phase interact with each other: part of the momentum carried by the fluid is transferred to the particles. The equation of motion would have the shape

$$\frac{\partial U_i}{\partial t} + U_j \frac{\partial U_i}{\partial x_j} = \frac{1}{\rho_f} \frac{\partial P}{\partial x_i} + \nu \frac{\partial^2 U_j}{\partial x_i \partial x_j} + \frac{1}{\rho_f} S_i, \tag{1.54}$$

where Equation (1.54) is simply the Navier-Stokes equation with the added term S_i, which is the momentum transfer from the fluid to the particles. S_i, for a particle of mass m_p would be:

$$m_p S = m_p \frac{dV}{dt} F_D + F_{G-L} + F_p + F_{add} \tag{1.55}$$

Where the terms on the left side of the equation are all the forces that are exerted on the particle in the flow. They are F_D the viscous drag force, F_{G-L} the lift and gravitational forces, F_p the fluid pressure force and F_{add} the "added mass force", a term that appears due to the fluid mass being displaced by the acceleration of the particle. While the drag force scales with the surface of the particle, all other forces scale with its volume. That means, for a sufficiently small ($d_p \sim 10\mu$m) particle the drag force is the only relevant force in the equation of motion. This force has the shape:

$$F_D = \frac{24}{Re} \frac{1}{8} \pi d_p^2 \rho_f \|U - V\|(U - V), \tag{1.56}$$

with d_p the diameter of the particle, ρ_f the density of the fluid, V the velocity of the fluid and Re $= \frac{U - V d_p}{\nu}$ the Reynolds number of the particle. For a micrometric sized particle, Equation (1.55) simplifies to:

$$\begin{aligned} m_p S = \frac{\pi}{6} d_p^3 \frac{dV}{dt} &= F_D \\ \frac{\pi}{6} d_p^3 \frac{dV}{dt} &= \left(\frac{24\nu}{d_p \|U - V\|} \right) \frac{1}{8} \pi d_p^2 \rho_f \|U - V\|(U - V) \\ \frac{dV}{dt} &= \frac{18\nu\rho_f}{d_p^2 \rho_p} (U - V) \\ &= \frac{1}{\tau_p} (U - V), \end{aligned} \tag{1.57}$$

where $\tau_p = \frac{d_p^2}{18\nu} \frac{\rho_p}{\rho_f}$ is defined as the particle relaxation time. This term represent the time the particle's velocity decays due to drag force, giving us a measure of the intrinsic particle response time to changes in the flow. A good tracer particle in a turbulent flow must have a relaxation time τ_p smaller than the characteristic turnover time at the small scales. This turnover time is $\tau_\eta = \frac{\eta^2}{\nu}$. The ratio between these two quantities is defined as the Stokes number St:

$$\mathrm{St} = \frac{\tau_p}{\tau_\eta} = \frac{1}{18}\frac{\rho_p}{\rho_f}\left(\frac{d}{\eta}\right)^2 \tag{1.58}$$

As expected, heavier and/or larger particles are worse tracers than lighter and smaller ones. Particles with $\mathrm{St} > 1$ are mostly unaffected by the small-scale motions of the flow. [37], while it is expected that particles with $\mathrm{St} \ll 1$ have a velocity field almost similar to the velocity field of the flow.

1.6.1 Preferential concentration and radial distribution function

As stated on the previous subsection, the Stokes number distinguishes between particles that have a velocity field very similar to the one of the flow (tracer particles) and particles that do not. For homogeneous and isotropic turbulence, tracer particles are expected to be randomly distributed. However, there is a range of Stokes number $\mathrm{St} < 1$ where the particles concentrate preferentially in regions of low vorticity and high strain. This preferential concentration scales with the Stokes number, reaching its maximum value at $\mathrm{St} \approx 1$ [38] [39]. The radial distribution function (RDF), is a measure of how the particle density varies as function of the distance of one particle, that is:

$$\mathrm{g(r)} = \sum_i \frac{N_i}{\rho V_i} \tag{1.59}$$

where N_i is the number of particles which can be found inside a sphere of volume V_i (and radius r), centered on the particle i. $\rho = \frac{N}{V}$ is the average number density of particles in the entire volume.

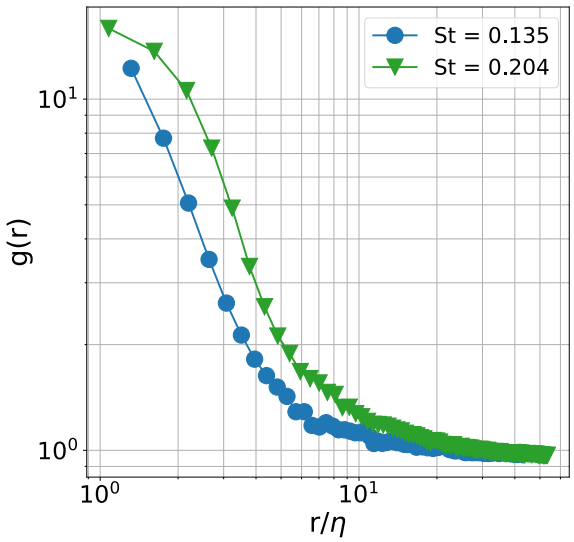

Figure 1.1: Typical RDF calculated from experimental data at St = = 0.135 (blue ●) and St = 0.204 (green ▲). The data was obtained from the Variable Density Turbulence Tunnel LPT setup by varying the turbulence intensity while using the same particles.

A value of $g(r_0) = 1$ indicates that the inter-particle distance conforms to a Poisson distribution, and the particles at a distance r_0 are randomly spread in the volume. A value of $g(r_1) > 1$ shows an above uniform concentration of particles with an inter-distance r_1, while $g(r_2) < 1$ means that particles preferentially are not found at a distance r_2 from each other. An example RDF can be seen in Figure 1.1. Note that $g(r)$ is larger for a higher Stokes number, which means a stronger preferential concentration.

Chapter 2

Hot-wire Anemometry

2.1 Principle of operation

A hot-wire is a type of anemometer that works via advective cooling. It consists of a small sensing element, usually metallic and cylindric, which is heated by Joule effect to some temperature well above the fluid's temperature. As the flow passes through the heated part, the wire cools down via forced convection, at a cooling rate dependent of the velocity of the flow. If the electric resistance of the wire depends on the temperature (which holds true for many materials) it is possible to find a relation between the resistance of the wire and the velocity of the incoming flow. A schematic drawing of a hot-wire can be seen in Figure 2.15. Here, several parts of the wire are named. The prongs of the hot-wire are two comparatively massive bodies holding the wire in place. They are usually made out of a material with poor thermal conductivity but good electric conductivity, and should be long enough so that the sensing element is not disturbed by the ceramic body. The stubs are the connecting element between the sensing element and the prongs (i.e. solder). Ideally, they have a good mechanical connection between every part and a negligible electric resistance and thermal conduction, while having a large thermal mass. The body of the hot-wire is the supporting structure of the whole system, and it should have both an aerodynamic shape to disturb the flow as little as possible and be from an insulating material to protect the prongs, which are usually embedded onto them.

2.1.1 King's Law

As previously described, hot-wire anemometry measures temperature changes due to convective cooling. Thus, a relevant ratio to study is the fraction of heat

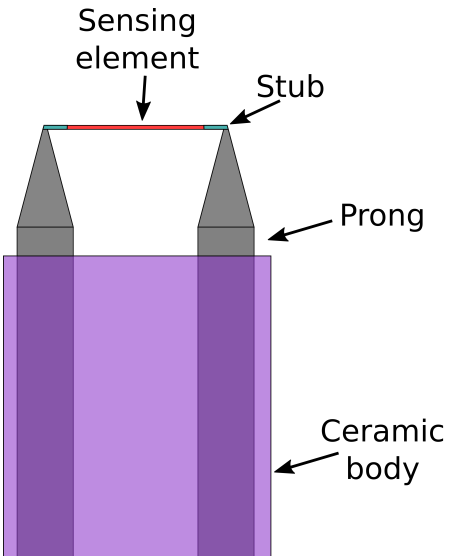

Figure 2.1: Schematic representation of the elements of a hot-wire. The sensing element (in red) is connected to the prongs by the stubs (blue). The prongs (grey) are sheated on a ceramic body (purple) which shields them from electric noise. Typical dimensions for a sensing element are $L = 1$mm, $d = 5\mu$m t, corresponding to length and diameter, respectively.

that is advected away by the flow and the amount of heat that is dissipated due to conduction with said flow. This ratio is represented by the Nusselt number:

$$\mathrm{Nu} = \frac{hL}{k_f}, \tag{2.1}$$

where h is the convective heat transfer coefficient, a proportionality constant dependent on the geometry of the wire and the flow conditions, L is the characteristic length of the body considered (in this case, the diameter of the wire d_w) and k_f is the thermal conductivity of the fluid. This term compares the convective heat transfer (represented by h) to the conductive heat transfer (represented by k_f/L). In general, the larger Nu is, the more prevalent convection (natural or forced) is.

A wire of length L, diameter d_w and electric resistance R_w which is subjected to a voltage difference of V_w, will be heated by Joule effect at a heating rate $J = \frac{V_w^2}{R_w^2}$. Now, if this heated wire is placed on a flow of mean velocity U such that the convection term is dominant, the heat balance at thermal equibrium is:

$$\dot{Q} = \frac{V_w^2}{R_w} - hA\Delta T = 0. \tag{2.2}$$

where $A = L\pi d_w^2$ the surface of the wire and h the previously mentioned convective heat transfer coefficient. By combining this with Equation (2.1),

one arrives at:

$$\mathrm{Nu} = \frac{V_w^2}{R_w k_f \pi d_w \Delta T}. \tag{2.3}$$

In literature, there are several expressions that link the Nusselt number with the wire's Reynolds number [40] [41], assuming that the forced convection term is dominant. All of them have the shape of a power law:

$$\mathrm{Nu} = A_0 + B_0 \mathrm{Re}^n. \tag{2.4}$$

Where A_0 and B_0 are a function of the fluid properties (and, for some models, the temperature of the fluid surrounding the hot-wire $T_{film} = \frac{T_w + T_f}{2}$.), and n is a constant. The mathematical definitions of A_0 and B_0, as well as the value of n, differ depending on the model, geometry of the experiment, Reynolds number and Knudsen number (defined in Equation (1.2)). For simplicity, in this thesis a model similar to [41] will be used. Here, and for air at ambient conditions, $A_0 = 0.39$ and $B_0 = 0.51$ are constants independent of T_{film}, while n was left as a fitting parameter.

Finally, by combining Equations (2.3), (2.4) one arrives at King's Law [42]:

$$\begin{aligned} \frac{V_w^2}{R_w k_f \pi d_w \Delta T} &= A_0 + B_0 \left(\frac{d_w}{\nu}\right)^n U^n, \\ V_w^2 &= A_1 + B_1 U^n, \end{aligned} \tag{2.5}$$

Where $A_1 = k_f \pi L R_w \Delta T A_0$ and $B_1 = k_f \pi L R_w \Delta T \left(\frac{d_w}{\nu}\right)^n B_0$ depend exclusively on the temperature and diameter of the wire as well as the properties of the flow. If the resistance has a linear dependence with its temperature: $R_w = R_0(1 + \Delta T \alpha)$, with α the temperature coefficient of resistivity, then it is possible to rewrite ΔT as,

$$\Delta T = \frac{R_w - R_0}{\alpha R_0}. \tag{2.6}$$

By combining Equation (2.6) with the equations for A_1 and B_1, it is possible to rewrite these coefficients as a function of a constant and experimental parameters only

$$A_1 = \frac{k_f \pi L R_w (R_w - R_0)}{\alpha R_0} A_0.$$
$$B_1 = \frac{k_f \pi L R_w (R_w - R_0)}{\alpha R_0} \left(\frac{d_w}{\nu}\right)^n B_0. \tag{2.7}$$

and thus relating U to the (constant) wire properties and the instantaneous values $V(t)$ and $R(t) = \frac{V(t)}{I(t)}$. In this way, the velocity of the flow can be deduced as long as both the voltage and current passing through the wire are measured during operation.

2.2 Heat Transfer considerations

The basis of King's law is that the forced convection caused by the flow is the main factor cooling down the wire. However, this is not the only effect involved in the system's thermal equilibrium. While the Joule effect is the only source of thermal energy in the system, there are several different energy sinks in this system. Besides forced convection, natural convection and thermal conduction from the wire itself to its supporting structure (named end-conduction effect) are the other relevant energy dissipating factors. It is necessary, then to find in which conditions forced convection dominates over the other energy sinks, and to constrain the wire to these conditions.

2.2.1 Natural convection

The term that distinguishes between the dominance of forced vs natural convection is the Richardson number Ri, defined as [43]:

$$\mathrm{Ri} = \frac{g\beta\Delta T d_w}{U^2} \tag{2.8}$$

Where g is gravity, $\Delta T = T_{wire} - T_{fluid}$ the temperature difference between fluid and wire, $\beta = \frac{1}{V}\frac{dV}{dT}$ the coefficient of thermal expansion of the gas ($\beta = 1/T$ for an ideal gas), and U the mean velocity of the flow. Forced convection dominates if $\mathrm{Ri} \ll 1$. Considering that the diameter of hot-wires are of order $d_w \sim 10^{-5}$ m, and usually heated at temperatures $\mathrm{T}_w \sim 600$ K, a good estimate would be $\mathrm{Ri} \sim 10^{-5}/U^2$. This means that, for the purpose of this thesis, forced convection dominates over natural convection as all studied cases have a mean

velocity larger than 3 m/s.

2.2.2 End-conduction effects and temperature distribution

End-conduction effects, as stated before, refer to the heat loss of the sensing element via conduction to the supports connecting the wire to the rest of the circuitry. This effect has been studied in great detail by Perry et. al. [44], who start by doing a theoretical analysis of the temperature distribution along the wire.

The most simple reasoning goes as follows: Consider a wire of length $L = 2l$ and diameter d_w, whose instantaneous relative temperature $\theta = \frac{T_w - T_0}{T_0}$ as a function of the normalized position on the wire $a = x/L$. The meaning of a can be seen schematically on the left image on Figure 2.2. This wire is connected to a pair of stubs that act as a perfect heat sink. The partial differential equation describing this system would be:

$$\tau \frac{\partial \theta}{\partial t} = \frac{\partial^2 \theta}{\partial a^2} + (J - \chi)\theta + \frac{J}{\alpha}. \tag{2.9}$$

With τ, J and χ constants, having the following expressions:

$$\begin{aligned} \tau &= \frac{\rho_w C_w L^2}{k_w}, \\ J &= \frac{R_0 I^2 \alpha}{L \pi k_w} \left(\frac{L}{d}\right)^2, \\ \chi &= \mathrm{Nu} \frac{k_f}{k_w} \left(\frac{L}{d}\right)^2, \end{aligned}$$

with $R_0 = R(T_0)$ at $T = T_0$ the ambient temperature, C_w and ρ_w the specific heat capacity and density of the wire. The thermal conductivity is denoted as k_i, where the subscript i can be either w or f referring, respectively, to wire and flow properties.

The term J corresponds to the heat generated due to resistive heating. χ is the convection term, while $\frac{\partial^2 \theta}{\partial a^2}$ is the heat conduction through the wire. Here, it has been assumed that convection is the predominant heat transfer mechanism between wire and medium, which is usually the case as discussed before.

The steady state solution of Equation (2.9) is:

$$\theta_s(a) = \frac{J_0}{\Omega^2} \left(1 - \frac{\cosh(\Omega a)}{\cosh(\Omega)}\right) \tag{2.10}$$

With $\Omega = \sqrt{\chi - J} = \frac{L}{d}\sqrt{\mathrm{Nu}\frac{k_f}{k_w} - \frac{I^2 R_{0,L}\alpha}{\pi k_w}}$. $R_{0,L}$ corresponds to R_0/L the resistance by unit length, which is constant for constant d_w.

Figure 2.2 shows $1 - \frac{\cosh\left(K\frac{L}{d}a\right)}{\cosh(K)}$ for varying L, $K = 0.1$ and $d = 1$. It can be seen that $l/d \gg 1$ is desirable in order to have a uniform temperature in most of the wire. As K depends on the wire (and flow) properties, the ideal l/d ratio also depends on the experimental conditions, as well as the material the sensing element is made of. A more complete analysis can be found in literature by Samie et. al [45]. In this work, the prongs of the wire are considered as perfect heat sinks, while the stubs are considered to have a linear relative temperature profile. The resulting temperature profile, in this analysis, is also expressed in terms of hyperbolic functions with a natural frequency Ω. This means that Equation (2.10) has a qualitatively similar behavior, for large l/d. For smaller values of l/d, Samie et. al. show that the signal, depending on the exact value of l/d, can be either attenuated or amplified.

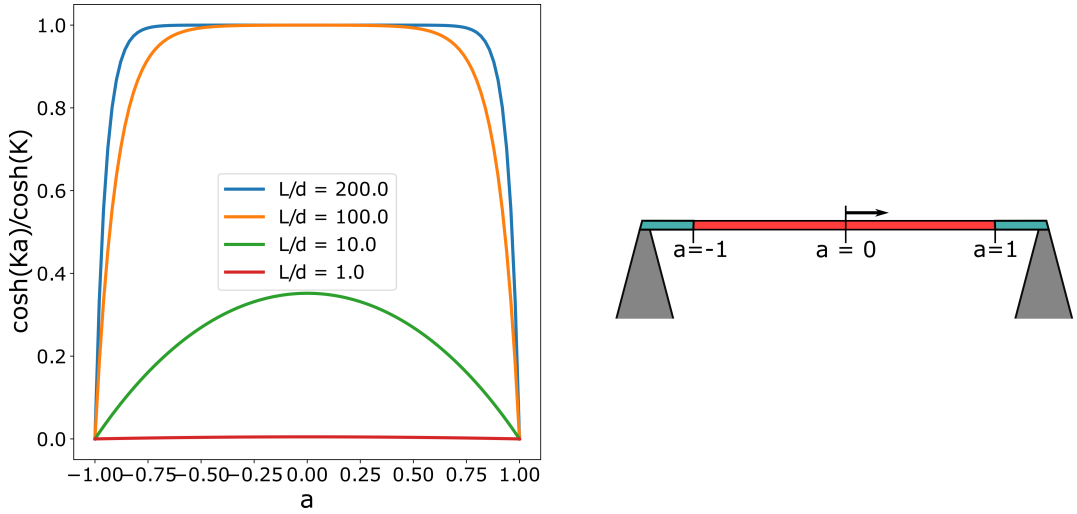

Figure 2.2: Left: Plot of $\frac{\cosh\frac{L}{d}Ka}{K}$ versus a, representing the theoretical distribution of the temperature on a hot-wire at various L/d ratios. K and d are constant. Right: Schematic representation of a hot-wire with the coordinate system used to parametrize Equation (2.10)

Ligrani et. al. [46] recommend the empirical value of $L/d > 200$. While this is a single constraint, there is evidence that other parameters (for example, the thermal conduction of the wire) are relevant. In fact, a study shows that this ratio is only valid for Pt wires [47]. A more general constraint is introduced by Hultmark et. al [48], in the shape of the quantity Γ:

$$\Gamma = \frac{L}{d_w}\sqrt{4\chi\frac{\bar{k}_f}{k_w}\mathrm{Nu}} \tag{2.11}$$

Where $\chi = \frac{R(T_w)}{R(T_0)} = 1 + \alpha\Delta T$ is the resistance ratio and $\bar{k}_f$ is the heat transfer coefficient of the fluid evaluated at $T_f = \frac{T_0+T_{wire}}{2}$. Hultmark et. al. proposes that, in order for end conduction effects to be neglected, $\Gamma > 14$.

Further studies by Li et. al. [49] indicate that the end-conduction effect manifests as a frequency-dependent signal attenuation which starts at the cut-off frequency ω_p:

$$\omega_p = \frac{40}{\tau} = \frac{40k_w}{\rho_w C_w L^2} \tag{2.12}$$

This signal attenuation is only significant when the end-conduction effects cannot be neglected. That is, when $\Gamma < 14$.
These results were calculated by assuming Equation (2.9).

2.3 Hot-wire electronics

Equation (2.5) shows a relationship between flow velocity U, voltage V and the temperature T on the wire, which can be observed by measuring the wire's resistance $R(T)$. The most commonly used circuits designed to operate hot-wires keep either current or resistance constant, while recording resistance and current, respectively. These setups have the descriptive name of constant current anemometry or constant temperature anemometry.

2.3.1 Constant Current Anemometry

A constant current anemometry circuit (CCA), keeps a constant electric current on the sensing element while measuring the voltage as function of time on a reference resistor connected in series to the sensing element. The resistance of the wire is calculated via Ohm's law. It's main advantage is the ease of design and analysis, as it behaves like a linear system. Figure 2.3 shows a simple diagram of a CCA designed with an instrumentation amplifier, with an operational amplifier to increase the signal.

Its drawbacks are a poor frequency response and low sensitivity to flow changes. Both of these issues stem from the fact that the system frequency response is dominated by the wire's natural frequency τ due its thermal inertia. These problems can be alleviated by electronic compensation [50]. An alternative to reduce the thermal inertia is to use a shorter (and thus, thinner) wire, although this makes for a more fragile wire, which is a concern in flows

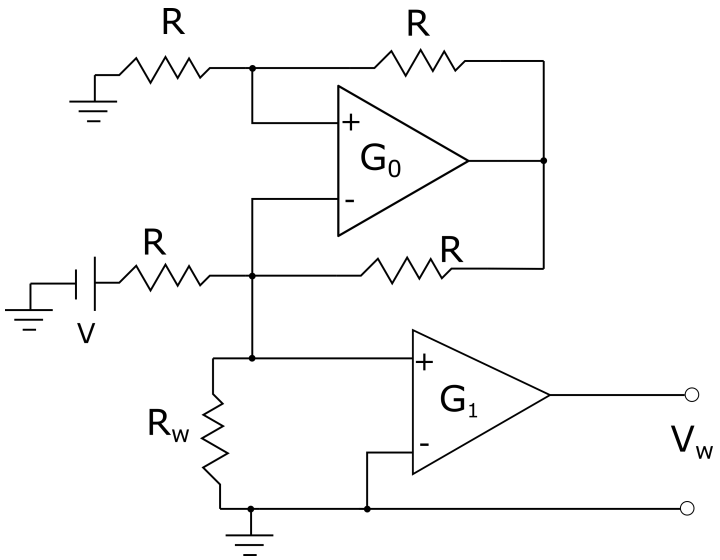

Figure 2.3: Diagram of a simple CCA. Here G_0 is a high current operational amplifier that supplies a constant current to the system, while G_1 is an instrumentation amplifier which amplifies the voltage difference on R_w by a known gain factor.

with particles. As the CCA is essentially a constant heating circuit, the wire is prone to burning if the mean flow velocity has a sudden decrease, which can be the case on environmental flows.

2.3.2 Constant Temperature Anemometer

A constant temperature anemometer device (CTA) keeps the resistance of the sensing element constant during operation. This is done via a more complex electronic driving unit. A simplified version can be seen on Figure 2.4.

The Wheatstone bridge is configured depending on a chosen overheat ratio, defined as:

$$a = \frac{R_w - R_0}{R_0} \tag{2.13}$$

The system, then, will balance the current and voltage in order for the hot-wire resistance to be equal to R_w or, equivalently, keeping the overheat ratio a constant. If the resistance has a linear relationship with the temperature, the temperature of the hot-wire is set as $T_w = T_0 + \frac{a}{\alpha}$. As the electronic system maintains the wire's temperature at its nominal sensing temperature T_w, the time response of the sensor is not strongly dependent on the thermal mass, but instead of the driving electronics. This, in turn, usually means that the transfer function of the system is not as straightforward as, for example, the low-pass filter behavior a CCA shows. The frequency response has been

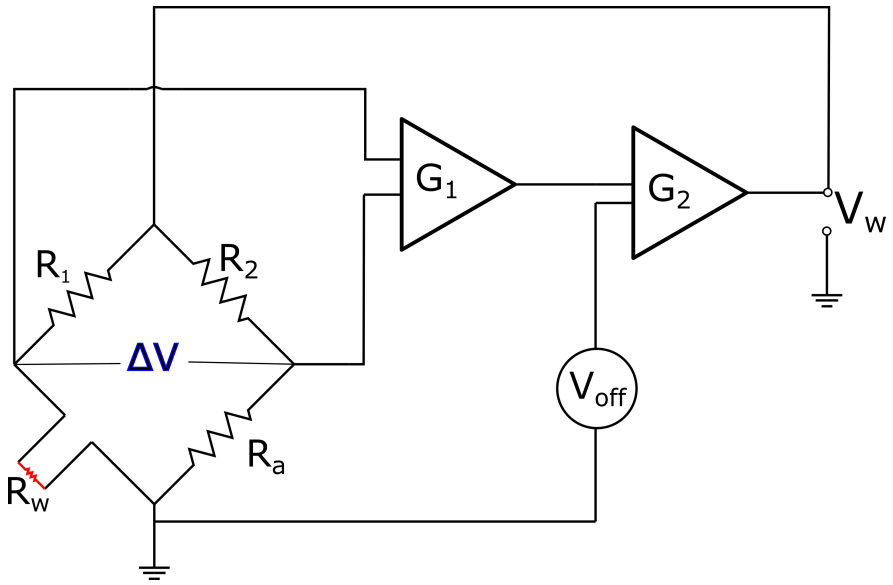

Figure 2.4: Diagram of a simplified CTA. The Wheatstone bridge made out of the resistors R_1,R_2,R_a and R_w, is balanced ($\Delta V = 0$, where ΔV is measured between the terminals $R_1 - R_w$ and $R_2 - R_a$) by means of the instrumentational amplifier G_1. R_a is a variable resistor which is used to tune the overheat ratio of the hot-wire with resistance R_w. In general, $R_1 = R_2$ and $R_a = 1 + \alpha R_0$ the target resistance of R_w. The second instrumental amplifier G_2 is used to control the offset voltage V_{off} on the output voltage V_w

shown to be non linear [51] [52], and so the data acquired would need to be compensated in order to have correct statistics. The frequency response is obtained by heating or cooling the wire at various, controlled frequencies. This can be achieved, for example, by passing a square-wave electric pulse through the CTA-controlled hot-wire. This procedure was originally postulated by Freymuth [53], and it goes as follows: The response of the circuit to either the rising or falling edge of square-wave pulse is recorded. From this data, the time τ_c is estimated from the start of the edge to the point where the response has decayed to 3% of its maximum value. In order to the system to be adequately dampened, the undershoot after the pulse should not exceed 15% of the maximum value. A graphical depiction of this can be seen on Figure 2.5

From τ_c the cut-off frequency can be estimated to be $f_c = \frac{1}{1.3\tau_c}$. Studies indicate that this technique is not necessarily the best indicator of a hot-wire actual cut-off frequency [52]. Nevertheless, it is a widely used characterization technique due to its simplicity in both execution and analysis. More complete (but complex) alternatives would be scanning the complete frequency range of interest, either by purely electric means (such as using sine waves) or by physical means. Examples of this include generating heat pulses on the wire via a pulsed laser [54] or by creating actual "fluid square waves" [55].

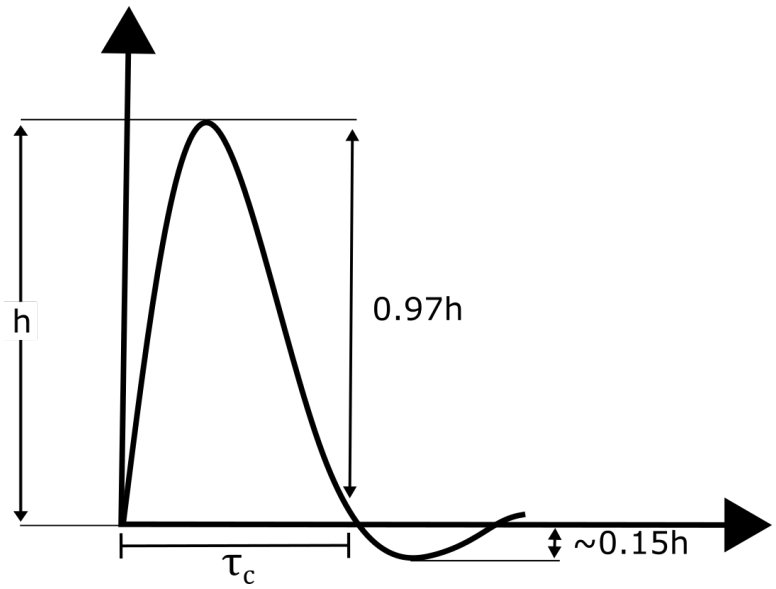

Figure 2.5: Drawing of a typical square-wave test result. The signal rises when the pulse passes through the hot-wire, reaching a maximum amplitude h. Then, it decays as the circuit adjusts the parameters to reach the equilibrium resistance. The characteristic time τ_c is measured from the start of the circuit response to the point where the measured amplitude is 0.03h. In order to ensure the system has the right amount of dampening, the following undershoot should be around 0.15h.

Another way to estimate the frequency response of the hot-wire is to apply a Fourier transform to the output voltage of the square wave test. if $F(\omega) = \mathcal{F}(V(t))$ is the Fourier transform of the output voltage, it is possible to calculate the gain G of the system as:

$$G(\omega) = 10\frac{\log\left(F\left(\omega\right)\right)}{\log 10}, \tag{2.14}$$

where G is in dB. The cut-off value ω_c is given by $F(\omega_c) = -3.01dB$

2.4 Material and size constraints

When designing a hot-wire, the properties of the flow (in this case, atmospheric air) must be taken into account in order to ensure an appropriate spatial and temporal resolution. In order to avoid spatial averaging of the smallest scales so that they are fully resolved, L has to be comparable to the Kolmogorov length η [56]. As seen on Figure 2.2, a large aspect ratio L/d_w is desired. Taking these two conditions into account, and considering that $\eta_{air} \sim 10^{-4}$ m, means that the hot-wire diameter necessarily has to be, at least, micrometric in size. Commonly used hot-wires, such as DANTEC's commercial anemometers can have a length of 1.25 mm and a diameter of

5 μm. For research, the Princeton-made Nano Scale Thermal Anemometry Probe (NSTAP [16] uses a rectangular beam as a sensing element, of length of either 30 or 60 μm, a thickness of 100 nm and a width of 2.5 μm. Recently, the university of Twente has developed their own version of these micro-machined hot-wires, that have a similar length but a smaller cross section of (300 nm width and 100 nm thickness). However, a small, thin wire can be quite fragile, so a material with a high tensile strength (e.g. tungsten) is required. This is particularly relevant for environmental measurements, where collision with particles such as pollen, sand, water droplets or ice crystals are likely.

Ideally, the wire properties remain constant during operation. High temperatures can make an otherwise inert material react with various chemicals. Tungsten, while being chemically inert to air at room temperature, it starts to react with N_2 and O_2 if heated at 300°C [57]. Other components present in the flow (for example, salt in a coastal environment) only increase the chances of an unwanted reaction in our sensor. These reactions can either change the properties of the wire in an unexpected way or permanently destroy it.

A high value of the thermal coefficient of resistivity α is desired, as it would mean a high sensitivity to velocity fluctuations without the use of electric amplifiers. For reference, the thermal coefficient of resistivity of DANTEC probes is that of Pt, $\alpha = 3.6 \cdot 10^{-3} °C^{-1}$. Common CTAs work under the assumption that α is both constant with respect to temperature (at least at the operational range) and larger than zero. If α does not meet these criteria, the CTA might be unable to properly balance the temperature on the wire, in particular if $R(T)$ is not monotonously increasing. While a model for a digital CTAs which could work without these assumptions exists, its frequency response is worse than the traditional ones [58].

Another important parameter is the temporal response of the anemometer. On a CTA, this is limited either by the driving circuit or, if $\Gamma < 14$, by the cut-off frequency ω_p. Ideally, the system is able to resolve frequencies of at least $\omega \sim \frac{U}{\eta}$. In the case of atmospheric flows, where the mean velocity can easily range from 10 to 20 m/s, ω can be as high as 200 kHz for $\eta \sim 10^{-4}$ m.

A common choice of material that meets most these criteria is Pt and some of its alloys (most notably, Pt/Rh). These wires can be either free-standing (as is the case of NSTAPs) or being supported by a stronger element, such as tungsten.

2.5 Carbon Nanotube hot-wires

2.5.1 Introduction

Carbon nano tubes (CNT) are small cylindrical tubes which can either be single walled or multi-walled. Single walled CNTs are, essentially a cylinder made out of a rolled over two dimensional sheet of carbon atoms arranged in a honey-comb structure (Graphene). Multi-walled CNTs are either several single-walled CNTs sheated onto each other, or a single graphene sheet rolled into the shape of a scroll. Depending on how the conforming graphene sheet is shaped, a single-walled CNT can show either a metallic or semi-conducting electric behavior [59]. Single walled CNTs can have a tensile strength of up to 0.15 TPa [60], which is about 5.5 times larger than tungsten whiskers [61].

Single walled CNTs have a diameter of only $3 - 5$nm [62], which is well below or too similar to the molecular mean free path of the fluids to be studied in this thesis. This means that, in most cases, Kn ≥ 1 and the wire would be observing a molecular flow, which falls outside our initial assumption of a continuous flow.

Their small size poses two other disadvantages: First, they require machinery with nanometric precision, which increases the difficulty of manufacturing these theoretical "CNT hot-wires" Second, the CNTs are too thin to withstand strong forces, even with their (comparatively) large tensile strenght. Multi-walled CNTs are thicker, but they are also less than ideal due to them being semiconductors [63].

Recently, a method to synthesize a fiber made out of CNT was developed [64]. These fibers are synthesized via wet spinning. Wet spinning is manufacturing process used to creat polymeric fibers. It consists on dissolving the base ingredient of the fiber (CNTs) in a solvent (chlorosulfonic acid). This mixture is then extruded through a spinneret. A spinneret is simply a solid block with several small holes. This spinneret is submerged in a coagulant solution (water), This coagulant bath causes the mixture to reform in fiber form, which then is grabbed and stretched by some spinning drums to give it the right fiber shape. The resulting CNF is rinsed with water after passing by the spinning drums. The objective is to remove the remaining solvent off the fiber, although traces of the acid stay inside the fiber, acting as a dopant. A more complete description of the process can be found in [65].

The resulting fibers are micrometric in diameter ($10 - 100\mu$m) while being several centimeters long. They not only possess the electric and heat conductivity of CNTs, but also have the strength of carbon fibers. Due to these

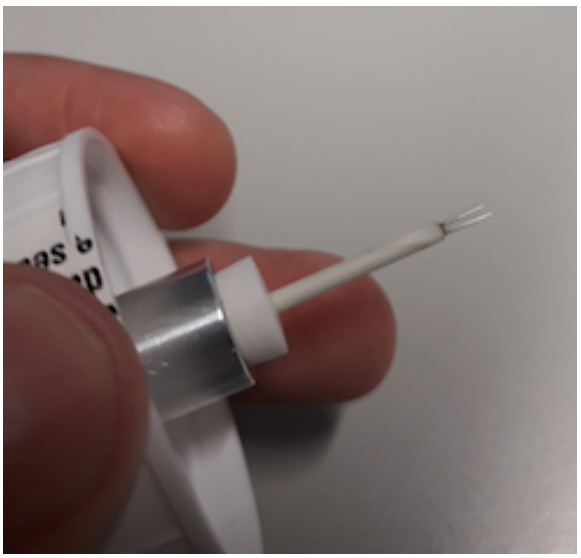

Figure 2.6: Photograph of a DANTEC 55P11 prong on a plastic holder for ease of transport.

properties, this material has been selected to be used as the sensing element of a hot-wire.

In the following sections, the design of the in-house built hot-wire is shown, as well as a short study of the suitability of this sensor in terms of tensile strength and the quantities Γ and ω_p previously introduced. Afterwards two experiments, showcasing both its imperviousness to collisions with heavy particles as well as the effects of water on the wire's signal are shown. Finally, the hot-wire is connected to a CTA and both the resulting square wave and voltage vs wind speed calibration curves are presented.

2.5.2 Hot-wire design

The hot-wire designed in this thesis consists on a CNF soldered onto the prongs of a 55P11 DANTEC hot-wire sensor, with its original sensing element removed. The 55P11 consist of two 20 mm long stainless steel prongs spaced $L = 1.25$ mm apart. These prongs are held by a 1.9 mm diameter ceramic tube body, with gold connectors on the other end. These gold connectors allow for the hot-wire to be connected onto a $\sim$ 200 mm probe support, which is connected to the CTA system via a coaxial cable of variable length (1 to 20 m). A sample picture of a 55P11 can be seen on Figure 2.6.

Physical properties and suitability of the CNF

The CNF used was commercially acquired from Dexmat Incorporated, with a nominal diameter of 10 μm. While the CNF itself has metallic be-

havior, some residual elements from the wet-spinning process are left on the wire that act as a semiconductor phase. They also state that these dopants are usually not removed during normal production as they increase the conductivity of the wire. In order to eliminate these residues, the manufacturer recommends to anneal the fiber a $500°C$ for at least 4 hours in an oxygen-free environment to avoid oxidation of the fiber.

A list of the nominal parameters of the CNF that are relevant for the calculation of Γ , ω_p are shown in Table 2.1, alongside the same values for W, Pt, Graphite and CNTs for comparison.

	Material				
Property [unit]	W	Pt	CNF	Graphite	CNT
Tensile Strength [GPa]	0.58 – 1.47	$0.125 - 0.15$	1.0	$0.048 - 0.076$	150
Density [g/cm^3	19.25	21.5	1.3	2.26	$0.9 - 9.9$
Electric Resistivity [$\mu\Omega$·m]	0.053	0.011	0.173	$0.08 - 0.11$	$0.005 - 800$
Thermal Conductivity [W/ mK]	175	71.6	450	$8.7 - 2195$	$10 - 375$
Specific heat Capacity [J/gK]	0.134	0.133	–	$0.7 - 0.77$	0.5,0.65
Thermal coef. of resistivity [10^{-3}/°C]	4.5	3.93	–	-0.45	$3 - 8$ (metallic)

Table 2.1: Physical properties of CNF and other materials (at room temperature) that are relevant for the calculation of both end-conduction and ultimate strength. Properties of tungsten come from [61] [66] [67], [68],[69]. Properties of Pt come from [70] [71], Properties of CNF come from [72], [65],[73]. Values for graphite from [74] [75] [76]. Values for CNTs from [77] [78] [79] [80] [81] [82] [83]. Values that could not be found in literature are marked as a dash.

Of note is the fact that the tensile strength T is similar for both tungsten and CNF materials. This means a $10\mu m$ CNF can withstand a tensile force 3 to 7 times larger than a 5μm tungsten wire before breaking. While the stress a wire is subjected to when a force is applied to its mantle is not solely tensile [84], it is nevertheless a good first indicator that motivated further study of the CNF as a candidate for more robust hot-wires.

By using the values in Table 2.1, an estimate for Γ and ω_p can be calculated. To be noted is that both the specific heat capacity and the thermal coefficient

of resistivity of the CNF were neither provided by the supplier nor found in the current literature at the moment of both writing and realizing this experiment. As such, the parameters for multi-walled CNTs and Graphite were taken as a reference point. Since both quantities are dependent on the material-specific properties such as the electronic configuration, there is no clear indication that these values are comparable to the ones of the CNF, so the resulting quantities Γ and ω_p are not accurate, but it is expected for them to give a qualitative idea of the behavior of the wire.

The end-conduction constraint Γ is in the range (5.84 – 7.73) and $\omega_{p,CNF}$ lies within 12500 and 17700 Hz. While $\Gamma_{CNF} < 14$, and therefore the wire is likely to suffer from end-conduction effects, they would only affect the signal at frequencies larger than at least $\sim$ 12500 Hz. This is larger than the advertised bandwidth of 10 kHz for a DANTEC 5μm Pt plated tungsten wire, although still lower than the desired 20 kHz from atmospheric turbulence.

Manufacturing

The manufacturing process starts with annealing the CNF to remove the dopants and ensure a proper metallic conductivity. As stated before, the annealing must be done on an oxygen free environment to avoid oxidation of the wire. Afterwards, the fiber is soldered onto the stainless steel prongs.

The annealing process was done on an Rapid Thermal Processing Furnace AnnealSys AS100 tower located at the clean-room facilities of the Goettingen University. This furnace allows for rapid temperature cycling (with a ramp of 200° C/min) by using quartz halogen lamps for heating and a water system for cooling. The fiber was sandwiched between two 4 inches Si-wafers, and the temperature of the system was monitored by a K-type thermocouple in contact with one of the wafers. The wafer-CNF system is situated inside a small (130 mm diameter, 25 mm height) airtight cylindrical chamber. The chamber is connected both to a rotary vane and turbomolecular pump setup and to a nitrogen evaporator, which in turn is connected connected to a 10000 L liquid nitrogen tank. This setup produces gaseous nitrogen with a purity rating of 5.0 (99.999% purity). The turbomolecular pump allows the generation of high vacuum, with a lower limit of $\sim 10^{-4}$ Pa for the pressure in the chamber. The connected nitrogen evaporator permits the constant injection of N_2. These two devices together are used to purge the chamber of any unwanted reactive gases.

In this thesis, the AS100 furnace was used to anneal the fiber at a temperature of 500°C for 150000 seconds (4 hours and 10 minutes). Before the

annealing, the chamber was purged from oxygen via vacuum pumping and subsequent N_2 filling. After this, the chamber was flooded with N_2 at a rate of 50 sccm (standard cubic centimeter per minute or, equivalently for N_2, $6.25 \cdot 10^{-2}$ g/min), while being simultaneously pumped by the previously described pumps.

Once annealed, the CNF had to be electrically connected to the 55P11 prongs. The method of choice was to solder the wire. A lead free, tin-based solder provided by GoodFellow GmbH (C-solder) was used to solder the CNF onto the stainless steel prongs. The solder has solidus temperature of 232 °C, and a density of $\sim 7.4 g/cm^3$. The solidus temperature is the temperature where the solder starts to melt, and both solid and liquid phases can coexist. The soldering was done using a temperature controlled soldering iron station, at a temperature of 300 °C. After the soldering process, the wire was cut using standard hairdresser scissors. A typical end result can be seen on Figure 2.7.

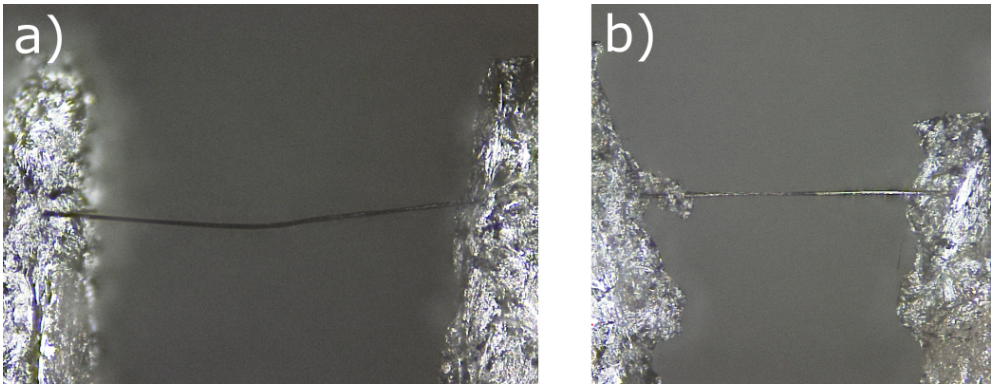

Figure 2.7: Images of CNF soldered onto Dantec prong. Image **a)** shows a properly soldered wire, while Image **b)** is an example of poor soldering quality. Note how in **b)** part of the solder covers the sensing part of the wire. The apparent size difference is due to the pictures having different scales.

The soldering process might contaminate the sensing element with metal. It can be seen in the right side of 2.7 **b**) that part of the solder has wetted the CNF. Also, a small piece of solder is connecting part of the sensing element to the prongs on the left side, creating a shorter effective sensing element. All hot-wires were inspected in the same way with a microscope after soldering. If the sensing element was found to have traces of solder, the prongs had the solder and CNF removed, and the entire manufacturing process was restarted.

The contact resistance induced by the soldering was estimated by measuring the total resistivity of a non-annealed CNF soldered onto the 55P11 prongs. The soldered hot-wire was mounted onto a 55H20 probe support, and its total resistance was then measured by a Brymen BM805s multimeter. A mean value of $(7.3 \pm 0.4)\Omega$ was obtained over 6 soldered CNFs. Consid-

ering that the length of the wire is 1.25 mm long, and using the supplied value for the nominal resistance found on Table 2.1, the non-annealed wire has an estimated resistance of 2.75Ω. Since the prongs have, according to the manufacturer, a resistance of 0.5Ω, the contact resistance is of 4.0Ω, which indicates non-ideal bonding between carbon wire, solder and stainless steel. On the other hand, a hot-wire made from annealed CNF has a total average resistance of $(13.6 \pm 0.8)\Omega$, which means the resistance of the annealed CNF is $R = 9.1\Omega$, approximately 3.3 times higher than the unannealed one.

Other methods to bond the CNF and a larger metal structure have been attempted, but the results were unsatisfactory. One attempt entailed passing the CNF through the inside of a 26G (0.45 mm outer diameter, 0.26 mm inner diameter) hypodermic needle, followed by deforming the needle by using a pair of pliers until both ends touch. The end result was either a broken wire, a not properly fixed wire or, in the best case scenario, a measured total resistance of order 1kΩ. Another mechanical bonding attempt entailed using a Kulicke and Soffa 4523 Wire Wedge Bonder to crimp the wire between a pair of flattened, Au coated stainless steel and a 50μm wide Au or Al wire. In this case, a good mechanical contact could not be achieved. Another attempt has been done using a MG Chemicals 8331-A Silver Conductive Epoxy Adhesive. After placing glue on top of the prongs, the wire was set inside and the system was cured on an electric furnace at 80°C for 30 minutes. The resulting bonding between wire and glue was mechanically weak, as the CNF easily slid off the dry glue when attempting to cut the wire with the scissors.

Robustness

As previously stated, there is a strong interest on high frequency measurements in environments which are hostile for thin wires, such as inside an ice cloud or during a wind storm. The CNF, with a high tensile strength and larger diameter, is nominally stronger than the typical 5 μm Pt-coated tungsten wire. Its robustness has been regularly observed during the manufacturing process, where the CNF was routinely tugged by tweezers. Furthermore, the wire had to be tensed by hanging a small piece of tape in one edge in order to be cut, as otherwise the scissors would only deform it. As an informal experiment, a thin syringe needle was passed in between the prongs of a 55P11 with soldered CNF in order to let the weight of the probe hang on the CNF. The wire did not break, and the electric resistance of the probe remained unchanged after the process. Attempting the same with a DANTEC miniature wire probe resulted in a broken wire.

In another test, silica particles of various sizes (gravel) were dropped from a height of approximately 50 cm onto a CNF hot-wire. The process was recorded by a single Phantom v12.1 high-speed camera, recording at a speed of 2.5 kHz with a resolution of 1280 x 800 px. The setup was illuminated by a Thorlabs M455L3 high power LED, $455nm$, > 900 mW focused at the measurement area by a 2 inches, $f = 35$ mm Thorlabs ACL50832U-A condenser lens. A long distance microscope objective (Questar Q100 Maksutov-Cassegrain) was used to reach the right magnification to observe the wire. The resulting images of one impact of a millimetric sized particle on the CNF hot-wire are shown on Figure 2.8. The resistance of the hot-wire before and after the experiment remained the same, at 13.6Ω. This experiment was not repeated with a DANTEC miniature wire probe.

2.6 CNF as a hot-wire

The results presented in this section were obtained from the hot-wires manufactured by the process described on Section 2.5 (DCHW). These hot-wires were connected to a 55H20 probe support, and then to a DANTEC StreamLine Pro Constant Temperature Anemometer via a 4 m long RG223 BNC cable. This anemometer allows for the configuration of custom-made hot-wires, as well as a square-wave test in order to correctly set the amplification and gain of the anemometer. A standalone calibrator unit was used to calibrate the wire. This unit permits the calibration of probes over a velocity range of over 10 m/s. It produces a jet of compressed air, whose velocity is controlled by a nozzle inside the system and is monitored digitally.

The overheat ratio $\frac{R_w - R_0}{R_0}$of the hot-wire was set to 0.4, with a voltage gain of 32 and a voltage offset of approximately $3.1V$. Larger values of overheat ratio produced a constant increase of the wire's resistance. As the resistance of the hot-wire recovers its original value after some time, this points towards the solder reaching the solidus temperature.

2.6.1 Square wave test

After the Wheatstone bridge is properly balanced (see Section 2.3.2), a square-wave test is performed with the software provided by DANTEC. The sofware produces the cut-off frequencies and a graph for each test. The resulting graphs were converted to data by using WebPlotDigitizer [85], and plotted together, as shown on the left side of Figure 2.9. The data labeled CHW02 cor-

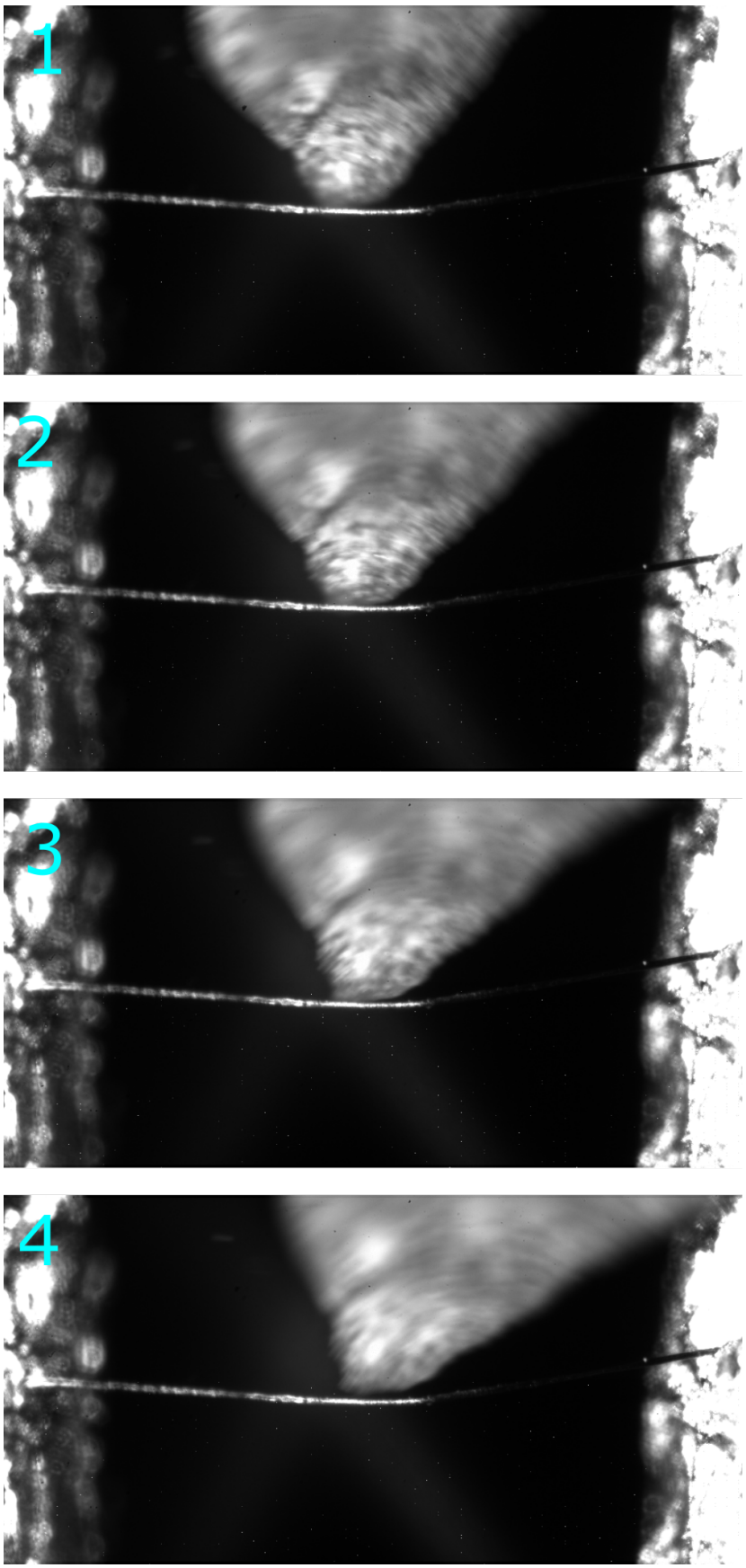

Figure 2.8: Snapshots of the moment when the gravel hits the wire, as recorded by the Phantom v12.1 camera at a framerate of 2.5 kHz.

responds to the square-wave test of the poorly soldered wire (seen in Figure 2.7 **b)**), while the other two dataset correspond to two different hot-wires. The cut-off frequencies, according to the square wave test, are $f_{01} = 18.5$kHz, $f_{02} = 21,1$kHz and $f_{03} = 27.5$kHz for the hot-wires CHW01, CHW02 and CHW03, respectively. On the right side of Figure 2.9, the frequency response G of the hot-wires, calculated by using Equation (2.14) on the square-wave response data, is plotted. For the other two wires, it was estimated to be the point where frequency response stopped being flat. Note that, for wires CHW01 and CHW02, the region where the signal has an artificial increase corresponds to the oscillations observed on the square wave test. **The cut-off values obtained are $\omega_{c,01} = 7700$ Hz, $\omega_{c,02} = 3800$ Hz, and $\omega_{c,03} = 26000$ Hz for CHW01, CHW02 and CHW03 respectively**. There is a good agreement between f_c and ω_c, provided that the system is not underdamped.

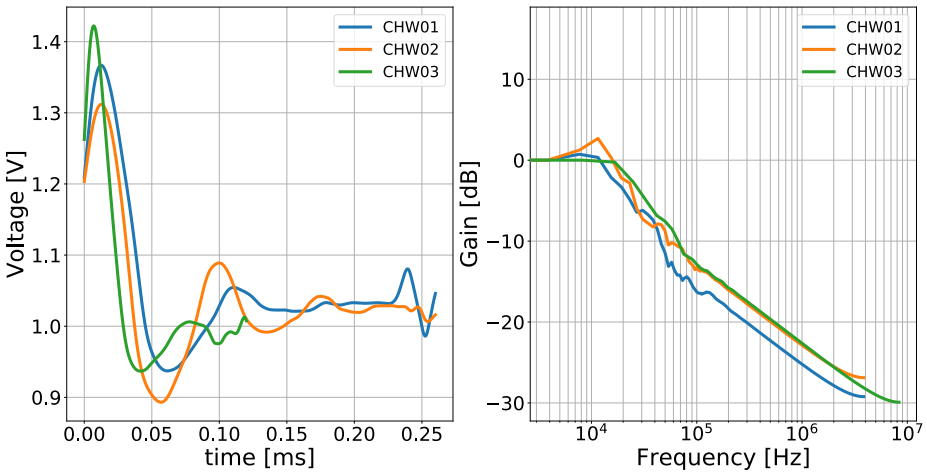

Figure 2.9: Left: Square wave tests for different hot-wires and bridge configurations. Right: Frequency response of the hot-wires. CHW02 corresponds to the square wave test of a poorly soldered wire (see Figure 2.7) **b**.

It is observed in the left plot of Figure 2.9 that there are some oscillations after the first zero crossing, which indicate an underdamped system. These oscillations could not be further reduced by modifying the configuration of the anemometer's bridge. As CHW02 corresponds to the wire shown on Figure 2.7 **b**, the underdamping is attributed to the presence of solder on the sensing part of the wire. As the solder has different properties (i.e. density, but also is likely to have different thermal conductivity and specific heat capacity). Figure 2.9 **c** does not show these oscillations, and it also has a higher cut-off frequency.

2.6.2 Calibration curve

The calibration data of two CNF hot-wires can be seen in 2.10 with their respective Kings Law Fit $V^2 = A_1 + B_1 U^n$ represented as a full line. All of them were taken in the velocity range $1 - 10$ m/s, although one of them (blue circle) reached the maximum value of +10V due to having a too high offset voltage. The average value of the coefficients (as shown on Equation (2.5)) taken over 5 calibrations are:

$$\begin{aligned} A_1 &= 5.0 \pm 0.1 \\ B_1 &= 2.8 \pm 0.1 \\ n &= 0.36 \pm 0.03 \end{aligned} \tag{2.15}$$

By using the relation presented in Equation (2.7) it is possible to estimate the value of the thermal coefficient of resistivity α. For this, $A_0 = 0.39$, $B_0 = 0.51$, $R_0 = 7.6\Omega$ and $R_w = 1.45R_0 = 11\Omega$ and $k_f = 26.24 \cdot 10^{-3}$ W/mK the thermal conductivity of air at room temperature. The value obtained are similar depending on whether A_1 or B_1 is used: $\alpha_{A_1} = (1.5 \pm 0.1) \cdot 10^{-4} {}^{\circ}\mathrm{C}^{-1}$ while $\alpha_{B_1} = (3.0 \cdot \pm 0.2) \cdot 10^{-4} {}^{\circ}\mathrm{C}^{-1}$.

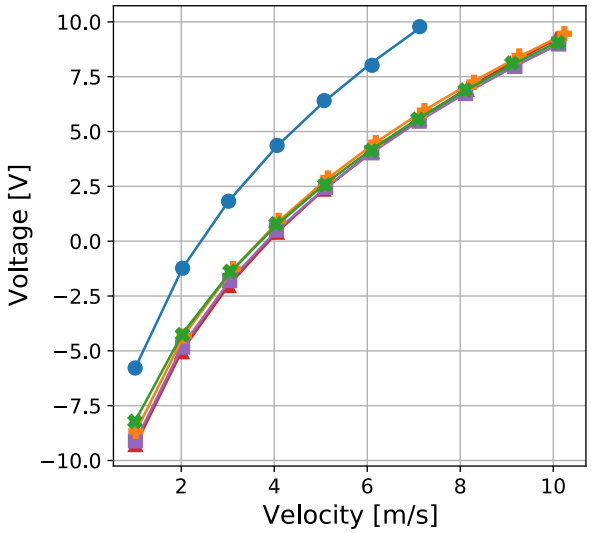

Figure 2.10: Five calibration curves for different hot-wires. The full lines correspond to the plotted King's Law fit.

The hot-wire shows a small drift when operated for too long. Figure 2.11 shows two calibration procedures done on the same wire, but with a 30 minutes difference. A small shift is observed, which can be attributed to the previously discussed change in the contact resistance of the wire. Another

possibility, which has been already reported in literature alongside a correction [86], is that the effect is caused by changes in the properties of the fluid (usually temperature and/or humidity).

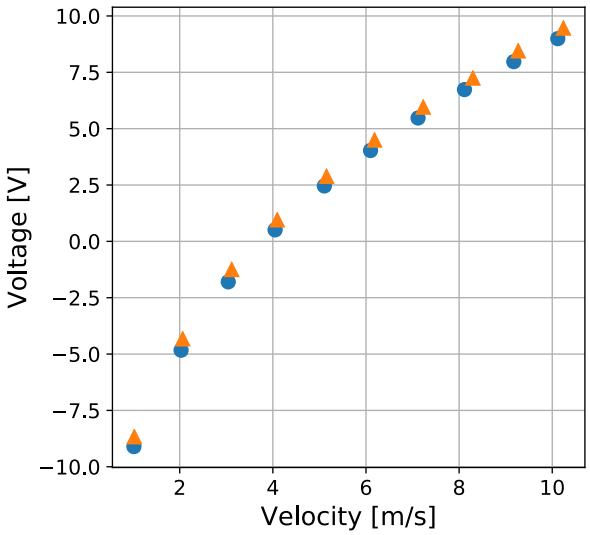

Figure 2.11: Calibration curves for one hot-wire taken at $t = t_0$ mins (blue ●) and at $t = t_0 + 30$ mins (orange ▲).

2.6.3 Bluff body test

A preliminary experiment was made on bluff body turbulence in order to test the behavior of the hot-wire. A frequency spectra was obtained, and from here the energy dissipation rate was estimated.

Experimental setup

For this experiment, the Prandlt wind tunnel was used. This tunnel was originally built by Fritz Schulz-Grunow from 1936 to 1938, and then reshaped in the 1970s [87]. The tunnel is an approximately 10m long, open return wind tunnel. The flow is driven by a direct current electric motor connected to an eight-bladed propeller. The motor has a maximum rotation rate of 1500 rpm, which translates to a maximum mean flow velocity of 12 m/s. Inside the tunnel, three grids of decreasing mesh sizes of 20, 0.35 and 0.15mm are placed downstream of the propeller in order to laminarize the turbulent flow. This tunnel has an irregular octagonal cross-section (see Figure 2.12), which is 1.15 m wide at the bottom, while having a base-to-roof distance of 1.25 m and a 1.5 m wall to wall distance. Further details can be found on [88].

Figure 2.12: Picture of the open end of the Prandtl wind tunnel

A CNF hot-wire was placed inside the Prandlt wind tunnel, aligned to the major axis of the tunnel approximately 5 m upstream from the end of the tunnel. In between the hot-wire and the laminarizing grid system a plastic box of dimensions 80 by 50 by 43 cm placed to act as a source of bluff body turbulence. The box was placed 2.8 meters upstream from the hot-wire, with its longest side placed perpendicular to the tunnel's major axis. The fan speed was set at 640 RPM, which nominally corresponds to 5 m/s. The hot-wire was placed aligned to the center axis to the tunnel, displaced laterally by 15 cm. The hot-wire was calibrated using DANTEC Streamline Pro CTA, using the setup described in Section 2.6. A National Instruments PCI-6123 16 bit data acquisition card was used to record the voltage time series, which then was converted to a velocity time series by using Kings law Equation (2.5) and the coefficients obtained from the calibratino curves, shown in (2.15). Two sampling rates of 20 and 40 kHz were used, recording data for 10 seconds for both frequencies. Afterwards, the data was filtered using an 8th order butterworth low pass filter. As filtering introduces edge effets, the first and last 60 values of the dataset are discarded. The energy spectrum $E(k)$ is calculated by the following equation:

$$E(k) = \frac{2\pi}{< U >} E(\omega) = \frac{2\pi}{< U >} \frac{\|\mathcal{F}(U)\|^2}{N f_s}. \tag{2.16}$$

where $\mathcal{F}(u)$ is the Fourier transform of the times series $u(t)$, N is the number of samples, $f_s = 40000$ is the sampling frequency in Herz.

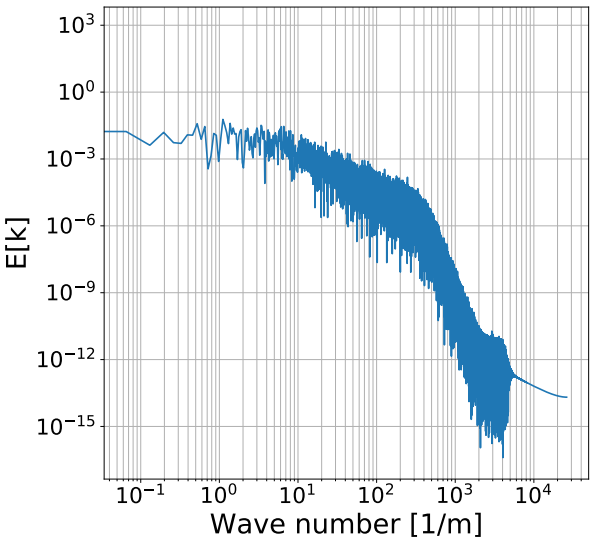

Figure 2.13: Energy spectrum of the velocity data measured by the CNF hot-wire.

Results

A mean velocity of 4.8 m/s, and a R.M.S velocity of $u_{rms} = 0.31$ m/s was measured. The corresponding energy spectrum can be found on Figure 2.13. The data is quite noisy, which can be attributed to low statistics.

The compensated spectrum (according to Kolmogorov's 5/3 law) can be seen on Figure 2.14. In this plot, the inertial range can be distinguished as a flat region. From the inertial range, it is possible to estimate ϵ by solving Equation (1.27). As the data itself is quite noisy, an average over the entire inertial range is performed. From here, the value $\epsilon_{spectra} = 0.085 \mathrm{m}^2/\mathrm{s}^3$ is obtained. Alternatively, one can calculate the energy dissipation rate from the gradient:

$$\epsilon_{gradient} = 15\nu \left\langle \left(\frac{\partial u}{\partial x^2} \right) \right\rangle, \tag{2.17}$$

which is equivalent to:

$$\epsilon_{gradient} = 15\nu \int_0^\infty k_1^2 E_{11}(k_1) dk_1. \tag{2.18}$$

By solving Equation (2.18), the value $\epsilon_{gradient} = 0.073 \mathrm{m}^2/\mathrm{s}^3$ is obtained. On the compensated spectrum, both values of ϵ are plotted as a dashed line, alongside the smoothed spectrum for better visibility. Both values are plausible for the inertial range of the spectrum, but only $\epsilon_{spectra}$ fits the smoothed curve.

The longitudinal second order structure function S_2 (see Equation (1.30))

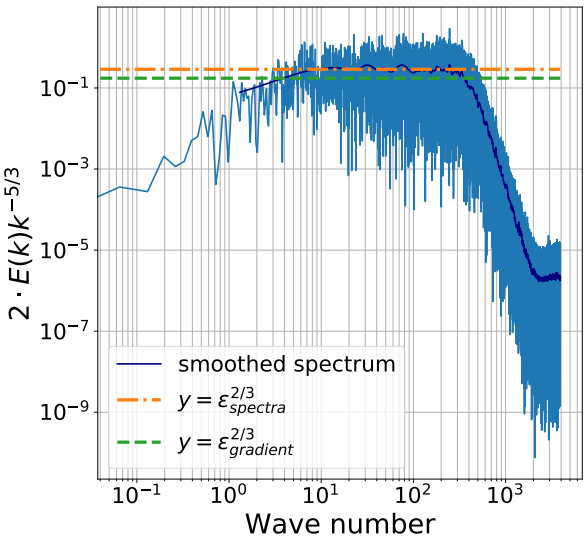

Figure 2.14: Compensated energy spectrum of the data measured by the CNF hot-wire (light blue solid line alongside the energy dissipation rate calculated from K41 $\epsilon_{spectra}$ (orange dashed line), ϵ calculated from the velocity gradient $\epsilon_{gradient}$ (green dash and dot line) and the smoothed compensated spectrum for visual aid (navy blue)

.

has been calculated by applying Taylor's frozen flow hypothesis (see Section 1.5.8) to convert the time series $U(t)$into a distance series $U(x)$. The resulting second order structure function S_2, alongside the $r^{2/3}$ and r^2 power laws can be seen on Figure 2.15.

While r^2 adequately fits the small scales region, it is easy to see that the inertial range does not follow the K41 power law of $r^{3/2}$. This is not unexpected, as the region at a height $h = 62.5$cm might have large velocity gradients generated by the bluff body [89] . Keeping in mind that these results are just an approximation, the second order structure function has been compensated by $r^{2/3}$ and the energy dissipation rate ϵ_{S_2} has been calculated by using the K41 relation:

$$\langle S_2 \rangle_{inertial} = 2(\epsilon_{S_2} \cdot r)^{2/3} \tag{2.19}$$

with $\langle S_2 \rangle_{inertial}$ corresponding to the average of the region which would correspond to the inertial range. A value of $\epsilon_{S_2} = 0.053 \mathrm{m}^2/\mathrm{s}^3$ is obtained. The values $\epsilon_{spectra}$,$\epsilon_{gradient}$ and ϵ_{S_2} are all within the same order of magnitude, the largest difference being a 62.35% between ϵ_{S_2} and $\epsilon_{spectra}$. These results are reasonable considering the experimental conditions and the accuracy of the estimation of ϵ by using the hot-wire spectrum.

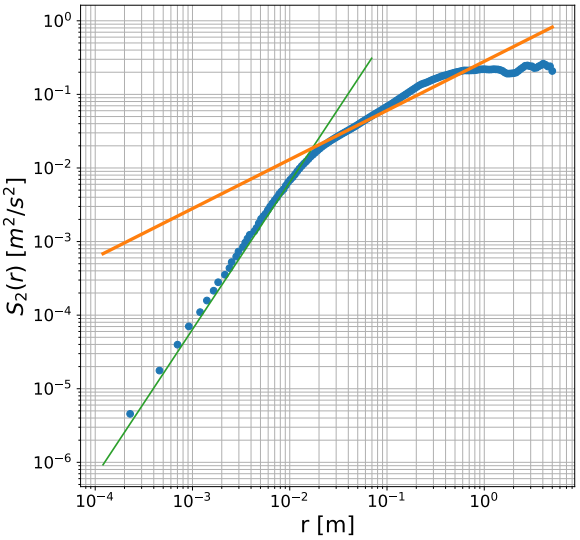

Figure 2.15: Second order structure function (blue) alongside the r^2 power law (green) representing the small range scaling and the $r^{3/2}$ representing the K41 inertial range scaling.

2.7 Discussion

The results observed in this section demonstrate the potential of the CNF as a material for sturdy, fast hot-wire anemometers. In particular, this wire has a similar tensile strength than commercially available Pt plated tungsten hot-wires, while having two times its diameter. The wire robustness has been extensively tested during this thesis work, and it has been found to be superior to conventional W plated wires. The results observed point toward less chances of the wire breaking when exposed to collision to water, ice or dust particles and other small solid particles commonly found in atmospheric conditions, such as hail.

Other adverse effect for a sensor caused by environmental conditions would be corrosion, which could be caused by sea salt in the air. This is typically the case on environmental measurements done in a coastal or maritime environment [13]. The CNF, however, is likely to remain unaffected, as the only known solvent of its base material (carbon nanotubes) is chlorosulfonic acid [65], which is unlikely to be present in the atmosphere, as it quickly reacts with moisture to form sulfuric and hydrochloric acid [90]. Further testing is required, however, as its capabilities have not been studied in full due to time constraints. Doubts remain as to whether the CNF has a linear coefficient of resistivity, and what are the implications of this for the sensing capabilities, as it nevertheless shows sensible results (See Sections 2.6.2 and 2.6.3)

The highest cut off frequency response obtained was $\omega_c = 26$ kHz. This value is higher than DANTECs hot-wire frequency range of 10 kHz and

slightly above the minimum desired frequency of 20 kHz.For $\omega_c = 26$kHz and $\eta = 0.5$mm, the maximum velocity the hot-wire can resolve before filtering occurs is 13 m/s. On the other hand, if the mean velocity is 40m/s, the minimum scale that can be resolved by this hot-wire would be $x \approx 1.5$mm. A higher frequency resolution is desired to properly resolve the smallest scales of a turbulent flow of $U > 13$ m/s. The cut-off frequency ω_c is also above the estimated cut-off frequency ω_p from the end conduction effects. This means that our estimate of ω_p is incorrect, which is not surprising as it was calculated using the heat capacity of graphite. However, it is not clear whether the measured cut-off frequency of the hot-wire is due to end conduction effects or something else. The heat capacity of the CNFs should be measured in order to clear these doubts.The combination of a strong resistance to a variety of effects that would break other hot-wires, with the fast temporal response shown by a CNF hot-wire opens the possibility to high resolution measurements in otherwise impossible conditions. To put things in perspective, recent environmental measurements in adverse environmental conditions found literature have been done either with quartz coated hot film sensors [91] or with nano scaled probes (such as Princeton's NSTAP [16]) that have a minimum chance of particle collision [92].

Quartz sensors, while quite robust, are also quite thicker than high resolution sensors (70 μm) and thus are normally used to keep track of the mean speed of the flow instead of measuring fine scale turbulence. NSTAPs, on the other hand, are extremely delicate probes which require an appropriately careful handling during installation. This could prove inconvenient in a long field campaign. Furthermore, they are made by a complex Si etching process which makes in-field repairs impossible. Furthermore, while being able to survive dust storms, they can be difficult to operate with CTA anemometers, as these nano-scaled wires have a tendency to break when operated with this kind of controller [93]. CCA operated NSTAPs, on the other hand, are much more robust but have a frequency range of $1 - 5$ kHz [94] Most of these problems are overcome with the presented CNF hot-wire, which have a faster frequency response than the reported setups. These hot-wires could be repaired in field, provided a soldering station and magnifying glass are in place. While not ideal due to differences in the frequency response induced by soldering quality, the CNF hot-wires show a similar response to velocity (see Section 2.6.2). Furthermore, they can reliably be operated with commercially available CTAs (such as DANTECs CTA), which ensures a fast temporal response and ease of integration with several pre-existing setups.

A power law is found between the velocity of the flow and the square of the voltage measured by the CTA. The measured exponent $n = 0.36$ differs from most theoretical values that range between 0.45 and 0.5. This is not totally unexpected, as this exponent also depends on the geometry of the wire [95]. In particular, and unlike most hot-wires of similar size, the sensing elements is not located at the very front of the prongs, but instead at several micrometers below the end of the prongs, and attached to one side.

From the coefficients A_1 and B_1 of this power law, the temperature coefficient of resistivity α is estimated. Its value ranges between $(1.5 \cdot 10^{-4})°C^{-1}$ and $(3.0 \cdot 10^{-4})°C^{-1}$. As the overheat ratio $a = 0.45$ is an input parameter, it is possible to calculate the temperature of the wire by combining Equations (2.13) with (2.6). The resulting equation is:

$$\Delta T = T_w - T_0 = \frac{0.45}{\alpha}, \tag{2.20}$$

with T_0 the ambient temperature. The lower estimate for ΔT is around 1500 °C. This value is unrealistically high, as the CNF oxidizes at temperatures lower than 500°C. One possible reason for this high value would be the solder reaching its solidus temperature, and thus changing its properties as it slowly starts melting. This, coupled with the varied square wave response, is evidence that the technique used to bond wire and prongs is not ideal, and either an alternative method of creating an electric and mechanical connection between wire and prongs must be found, or a different solder should be used.

The CNF hot-wire, after calibration, has been tested on a bluff body turbulent flow with a commercially available CTA. The resulting energy spectrum shows a good fit for the K41 theory at the inertial range. By using Taylor frozen flow hypothesis, the longitudinal second order structure function S_2 has been calculated. The predicted power law $C(\epsilon r)^{2/3}$ does not properly fit the inertial range of S_2, which indicates the turbulent flow is not isotropic and homogeneous at these scales. This would also explain the disparity of 30 to 40% between the energy dissipation rates calculated by different methods (velocity gradients, energy spectrum, and second order structure function).

Chapter 3

Lagrangian Particle Tracking on Variable Density Wind Tunnel

This chapter consists of three sections. Section 3.1 presents a review of the current state of the Variable Density Turbulent Tunnel (VDTT) [1], and a description of the experimental setup used for the Lagrangian Particle Tracking (LPT), previously implemented by C. Kuechler [2]. This includes the flow generating setup (active grid, main fan), the camera and illumination system and the particle disperser. A characterization of the particles used is also provided. The LPT setup has been modified to be able to work with particles of 12μm, which is half the diameter used in its previous iteration.

In section 3.2, a description on how the videos are acquired and processed can be found, as well as a first comparison between the velocity measurements previously done by a high resolution hot-wire and the LPT.

Finally, section 3.3 shows the work done when analyzing the particle-pair relative velocity and inter-particle-pair distance in isotropic turbulence. First, a brief introduction of the relevant quantities used is presented, which includes the formulas used to calculate them. Then, a characterization of the relative distance of the particles is presented, followed by the characterization of the relative velocities of the particles in the shape of the second order structure function. The structure function is compared with the longitudinal structure function calculated from previous hot-wire measurements in similar conditions, and a measure of the local anisotropy of the flow is given.

3.1 Experimental setup

3.1.1 Wind Tunnel

The VDTT is a closed-loop wind tunnel, with a mean flow velocity varying from 0.5 to 5.5 m/s. The working gas is SF_6. This gas can be pressurized to pressures of up to 15 bar at the temperature range 15 – 30 °C. By pressurizing the gas, the density of the gas ρ increases, which in turn decreases the value of the kinematic viscosity ν, as ν is inversely proportional to the density of the fluid. Since Re $\sim \frac{1}{\nu}$, tuning the kinematic viscosity allows for larger Reynolds numbers to be achieved without the need of increasing the mean flow velocity. The tunnel consists of two parallel 11.68 m long tubes with an inner diameter of 1.84m. These tubes are parallel, but separated by 3.5 m from center to center, one being above the other. Both tubes are connected on each side by one elbow of inner diameter 1.52 m. The whole setup thus has a total volume of 88 m^3. All tubes are made out of steel, the straight tubes having 20 mm thick walls while the elbows have 18 mm thick walls. The tunnel is also equipped with a bypass circuit that filters out particles from the fluid. The bypass circuit, - when open- draws the fluid from one of the elbows, passing it through a class F9 filter (with an efficiency of 98% for particles of a diameter of 1 μm) before returning it to the other elbow. This bypass filter was always active when performing these experiments. The flow within the VDTT is driven by a fan with 20 blades, which is coupled to a 210 kW motor. The motor allows to set the fan rotational frequency up to 24 Hz, which produces an adjustable flow velocity on the range of 0.5 m/s and 5 m/s with SF_6 at 15 bar. The motor is housed to prevent particles damaging its bearings. This motor is water cooled via a dedicated water line connected to the building. The fan is located at one end of the lower tube, directly upstream of one of its elbows. A heat exchanger is located at the upstream end of the upper tube, removing the motor energy that is dissipated into heat. It is placed right after the flow-driving fan. This heat exchanger consists of two registers of water-cooled plates. The water circuit inside these plates is set up in such a way that the temperature gradient along the cross-section of the tunnel is minimized. The heat exchanger is fitted to the tunnel via a contraction, which is then re-expanded. Three meshes of increasing spacing (0.850 mm, 1.267 mm and 2.833mm) are located alongside the expansion area in order to re-laminarize the flow. More details can be found in [1].

Active Grid

The flow turbulence is modulated by an active grid, which is located close to the 2.833 mm laminarizing grid, downstream from it. This grid consists on 111 winglets of size 11 x 11cm that can be rotated via individual servomotors. The motors allow each one of them to be moved over 180 degrees (with respect to the mean flow velocity) at a speed of up to 400 degrees per second, allowing a generation of a turbulent shear-free region of Re_λ up to 6000.

Its operating principle goes as follows: Each winglet opens and closes independently, creating a wake by blocking or unblocking the flow. Each wake interacts with the ones generated by the other winglets, creating a turbulent flow which is then carried downstream. The opening and closing of the winglets is controlled via an algorithm that updates their position every 0.1 seconds. At each timestep, the position is updated based on a set of random angles and their convolution with the grid history and a predefined kernel, correlating these random positions in both space (a measure of the number of neighbors involved) and time (how many of the previous time steps are considered). The kernel is defined by a certain function, a correlation length for space and time and a RMS absolute angle Φ_{RMS} with respect to the mean flow. For example, a "Long Tail" kernel consists of the superposition of two rectangle functions, one with width 2σ and height h and the other with width σ and height $1-h$. The (normalized) long tail kernel $\mathrm{LT}(x)$ of correlation length σ around an arbitrary value x_0 would follow the equation:

$$\mathrm{LT}_{x_0}(x) \begin{cases} 1 & x \in [x_0 - \sigma, x_0 + \sigma] \\ h & x \in [x_0 - 2\sigma, x_0 - \sigma) \cup (x_0 + \sigma, x_0 + 2\sigma] \\ 0 & \text{otherwise} \end{cases}$$

The grid correlation lengths are related to the large-scale flow properties by mean of a typical correlation volume $V_c = (\sigma_s)(\sigma_s)(U\sigma_t)$, which defines a correlation length $L_c = \sqrt[3]{V_c}$. The Reynolds number of the grid is defined as:

$$\mathrm{Re}_{grid} \sim \frac{UL_c \sin(\Phi_R MS)}{\nu} \tag{3.1}$$

And the Taylor-scale Reynolds number of the tunnel at the measurement volume relates to Re_{grid} by: $\mathrm{Re}_\lambda \approx 0.95\sqrt{\mathrm{Re}_{grid}}$. Further details can be found in [96] [93].

The notation used to mark the experiments is:

$$\mathrm{K}\left(\frac{\sigma_s}{0.11\mathrm{m}}\right)\mathrm{K}\left(\frac{\sigma_t}{0.1\mathrm{s}}\right)$$

Where K denotes the kernel type and the correlation lengths are denoted by σ_s and σ_t, where the subscript signal denote that they are spatial and temporal correlation lengths, respectively. The spatial correlation length σ_s is normalized by the spacing between winglets, while the correlation time σ_t is normalized by the update time-step of 0.1s. For example, LT4LT3 denotes an experiment with a Long Tail correlation kernel for both space and time, with correlation length $\sigma_s = 0.44$m and correlation time $\sigma_t = 0.3$s. As all experiments presented in this thesis were realized with a Long Tail kernel with $h = 0.4$ and $\Phi_{RMS} = 50$, these values are not used to distinguish each dataset.

Illumination

The measurement volume is illuminated by a frequency doubled, green (515 nm wavelength) TruMicro 7240 Yb:YAG laser (Trumpf Laser GmbH, Schramberg, Germany). It has a maximum energy of 7.5 mJ per pulse, releasing 300 ns long pulses at a frequency of 20 to 100 kHz with a maximum power of 300 W. The laser light is guided by a 30 m long optical fiber (LLK-D06, 100mm mrad, Trumpf Laser GmbH) into a light-sealed optical box, before entering the wind tunnel through a pressure-sealed window. The numerical aperture NA of the laser at the fiber end is 0.103 [97].

Optical Box

The laser light has to travel roughly 12 meters before reaching the measurement volume. As both the refractive index of the gas [98] and shape of the tunnel are dependent on the pressure inside, placing lenses at the interior of the tunnel is both difficult and impractical. Therefore, an optical box has been placed right outside the laser inlet to bring the beam in the desired shape at the measurement volume. The box holds 3 lenses which, together, act as a collimator and beam expander system, as seen schematically on Figure 3.1. After passing through this optical setup, the laser beam enters the VDTT through a borosilicate glass window specially manufactured for high pressure usage (METAGLAS® Type 76 SIGHT GLASS). The glass window is protected by an automatic ball valve which, if a leak is detected through its flange,closes to avoid further leaking of gas to the outside and deactivates the

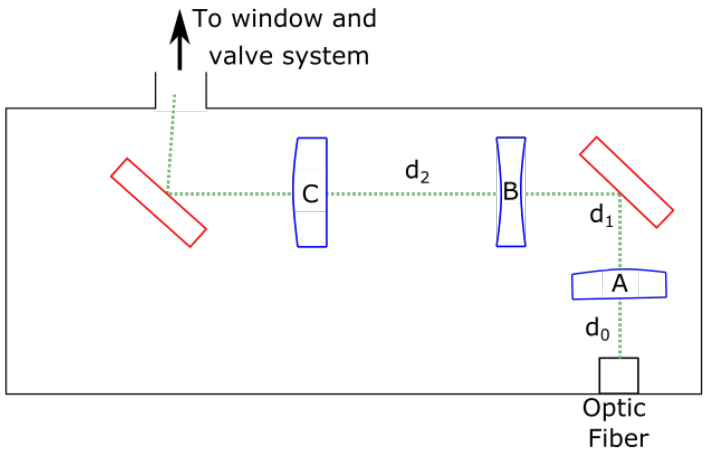

Figure 3.1: Schematic of the lens configuration at the optical box. It consists of three lenses. Lens **A** is a planoconvex lense of focal length f = 50 mm, which is separated by a distance of $d_0 = 50$ mm from the ending of the glass fiber which carries the laser. This lens is slightly tilted at an angle with respect to the beam path in order to avoid the back reflection to hit the glass fiber and potentially damage it. Lens **B** is an f = -25 mm biconcave lens, which is placed roughly $d_1 = 50$ mm after Lens **A**. Finally, and separated by $d_2 = 90$ mm from Lens **B**, an f = 125 mm planoconvex lens (labeled as **C**) is placed. Lenses **B** and **C** together act as a beam expander. Two mirrors (represented as red rectangles) are used to redirect the beam to the opening of the wind tunnel and to make the optical path long enough to be able to place the lenses.

laser. Finally, at the measurement volume, a round and almost parallel beam with a diameter of approximately 4 c can be observed. This size is comparable to the in-plane field of view of 3.58 cm obtained with the current camera setup.

Mirror path

Five mirrors are located inside the tunnel and used to guide the beam to the measurement volume, as shown on Figure 3.2. The first mirror is installed on a remote-controlled servomotor mounting (AC-8823, Newport Optics) located at the side of the VDTT, in front of the laser inlet. This mounting is used to externally realign the laser with the cameras whenever the working pressure is changed, as the optical path changes due to deformations of the tunnel. The second mirror is a two inch diameter mirror mounted on a standard ThorLabs fixed mount. This mirror has an aerodynamically shaped 3D printed hood to both protect the mirror from the strong flow, prevent misalignment caused by said flow, and to minimize its impact to the resulting turbulence at the measurement volume. From here, the beam path goes to one of three mirrors which are around the measurement volume and installed each on a static aluminium profile: two of them fixed on the ground and one

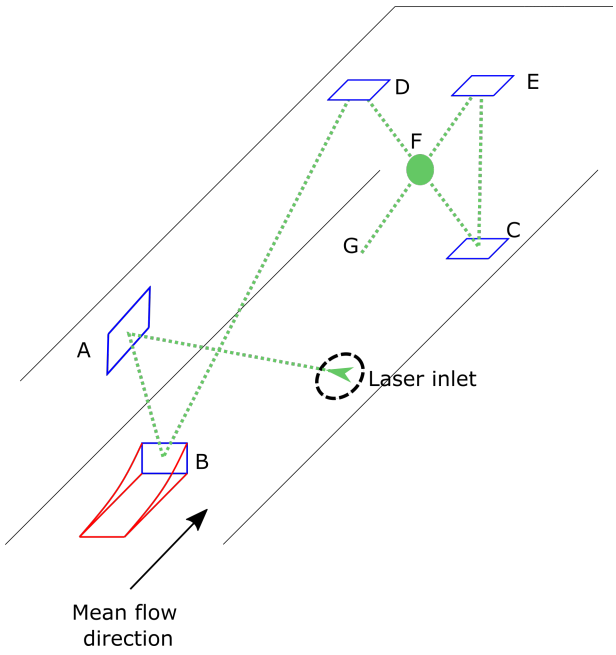

Figure 3.2: Schematic diagram of the mirror path inside the VDTT. From the Laser inlet, the laser beam enters and hits a 2-inch mirror installed on a remote-controlled servomotor mounting **A**. Here, it's redirected to the static mirror on the floor at position **B**. Mirror **B** has an aerodynamically shaped hood (drawn in red) protecting it from the incoming mean flow (shown by a black arrow). Afterwards, the beam hits the three mirrors **C**, **D** and **E**. Both **D** and **E** are at the roof of the tunnel. The three mirrors are positioned in such a way that the beam crosses itself at the measurement point **E**. Finally, the laser impacts the floor of the wind tunnel, at point **G**.

on the ceiling of the measurement section. These are angled from each other in such a way that they make the incoming beam cross itself at the measurement volume, effectively enhancing the signal of the tracers used, as the total light intensity is higher. A schematic picture of the full mirror setup can be seen on Figure 3.2

3.1.2 Camera setup

The camera setup used consists of three externally-triggered Phantom v2511 high-speed cameras, recording at a frequency of 25 kHz with a resolution of 1280x800 pixels. The protective glass on top of the sensor was vented by the manufacturer to avoid breaking due to pressure differences, thus allowing their operation at non-atmospheric pressures. All other electronic devices used here require no other special preparations in order to be operated at the pressure range 1-15 bar of SF_6.

The camera optics are a AF Micro-Nikkor 200 mm 1:4D IF-ED camera lens, with an aperture of $f/11$, and two $2\times$ teleconverters. This results in a

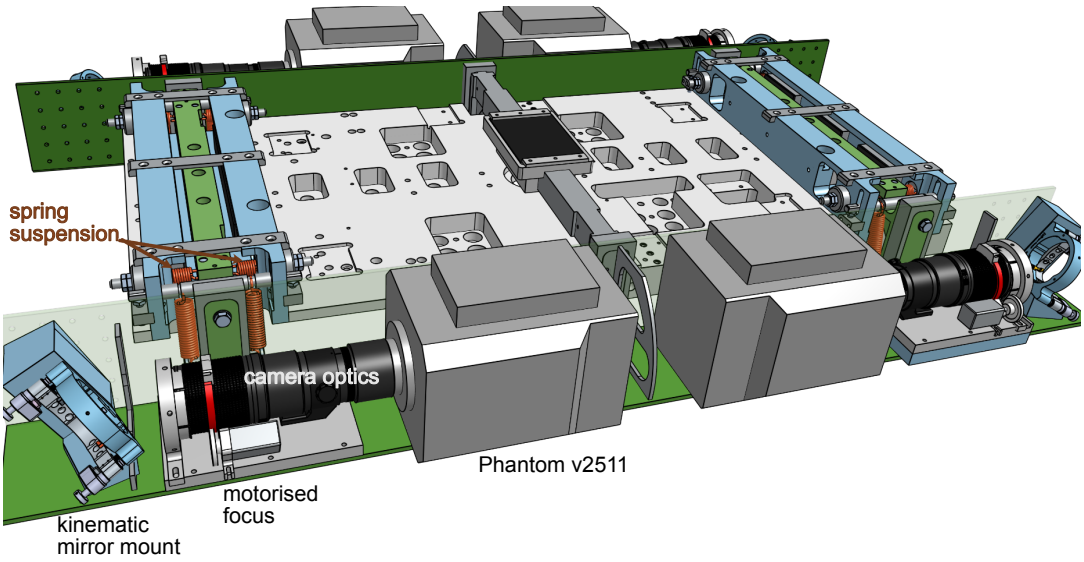

Figure 3.3: 3D rendering of the camera platform. The two camera support structures (green) are connected rigidly with each other, but are otherwise suspended by vibration/damping springs (red). Both the kinematic mirror mounts and the focusing part of the camera optics can be remotely controlled, allowing for adjustments without the need of opening the tunnel. The measurement volume is located approximately 60cm above the center of the platform (dark grey square). Image provided by C. Kuechler.

magnification $M \sim 1$ when focused at the measurement volume. The pixel size of these cameras is 28μm, which corresponds to the size of the light sensing element.

The cameras are located on a spring-suspended movable platform, in order to decouple the imaging from the vibrations on the tunnel induced by the fan driving the flow. As this sled is located below the measurement volume, a mirror is placed in front of each camera, pointing towards the measurement volume. For each camera lens, a servomotor (Trinamic QSH2818-51) are connected to a timing belt coiled around the manual focus ring, allowing external refocusing. Refocusing is necessary when changing the operating pressure, because the refractive index of SF_6 is density dependent. A more detailed description can be found on [2].

3.1.3 Particles

Suitable particles for tracers, as stated before, must have a low Stokes number. As $\mathrm{St} \sim \frac{\rho_p}{\rho_f}\left(\frac{d_p}{\eta}\right)^2$, this means that either small or less dense particles are preferred over larger or heavier ones. Additionally, the tracer particles should have a diameter d_p smaller than the flow length η in order to avoid spatial averaging of the small scales. Reducing the size of the particle, then, is the best way to ensure both conditions are fulfilled. The previous iteration of

this setup used 30μm particles, with an estimated density of $\rho = 1400\text{kg/m}^3$ [93].

The particles used for the experiments as tracers are commercially available KOBO cellulose particles *CELLULOBEADS D-10*. These particles have a nominal diameter of $d_n = 15\mu m$ and a nominal bulk density of $\rho_b = 708\text{kg/m}^3$. These particles are nominally smaller than the minimum flow length scale $\eta \approx 30\mu$m that was used for these experiments. Furthermore, since they are made of cellulose, they do not significantly absorb light at the wavelength of the laser, are biodegradable and pose little risk to the environment and are not a major health hazard. These properties make them suitable for this experiment. However, as seen from 3.4 **C**, the particles are not perfectly full spheres, having instead small cavities on the surface. It is plausible to believe that these cavities manifest as a porosity not only at the surface, but also within the bulk of the particle as well. This porosity is not known, which impedes a straight calculation of the particle density from the bulk density ρ_b. Thus, ρ_p has been measured independently.

Diameter

A Keyence laser confocal VK-x210 microscope was used to acquire a 3D profile of a slide of glass that was left inside the wind tunnel during a typical experiment run. The microscopic image of such a slide can be observed on 3.4 **A** and **B**. The average particle area A_m was obtained from the images using standard algorithms found in ImageJ, and then the mean diameter d_m was estimated by using the equation $A_m = \pi(\frac{d_m}{2})^2$. The resulting histogram can be seen on Figure 3.5 **A**. This histogram of diameters shows a sharp peak centered at $d_m \approx 12\mu$m, which is similar to the nominal value of $d_m = 15\mu$m and would correspond to a single particle. A second, smaller peak appears to be at around $d_{2m} \approx 17\mu$m, which would correspond to a two particle cluster. The probability of finding a two particle cluster is 3.5 tiems lower than finding a single particle, which indicates that the particles are predominantly non-clustered.

Density and Stokes Number

The density of the particles was estimated via its aerodynamic particle size. This quantity is related to the particle density by:

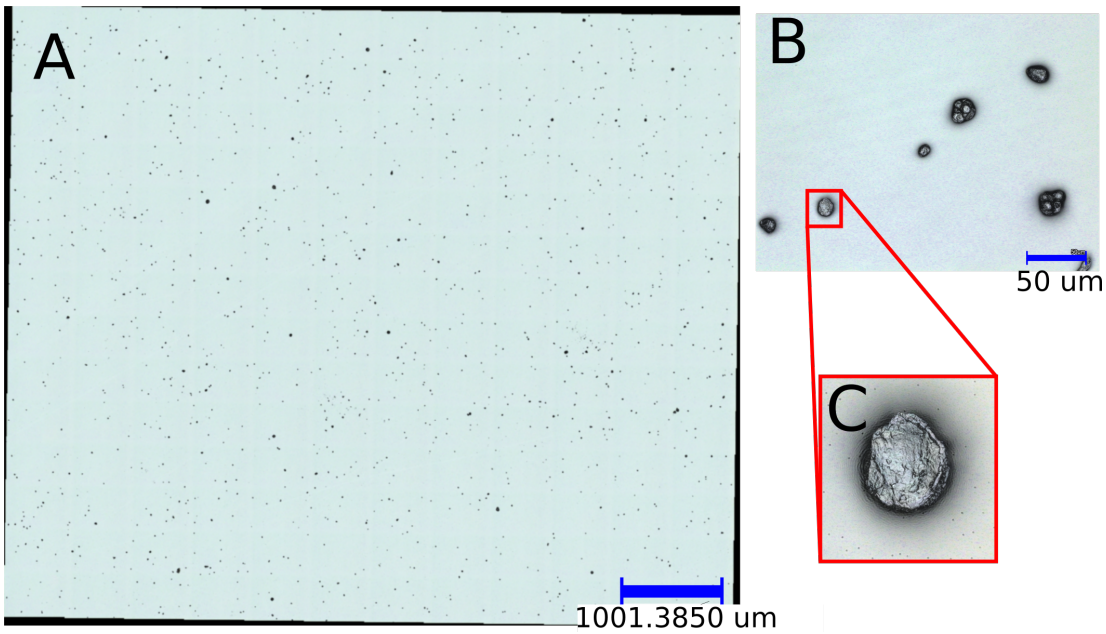

Figure 3.4: Imaging of the settled particles of a typical wind tunnel experiment. **A** shows an overview of the settled particles. **B** shows an image taken on the same sample with a larger magnification, while **C** shows a microscope image of a single particle. In **A** and **B**, the scale is represented as a blue line.

$$d_{ae} = d_p \sqrt{F \frac{\rho_p}{\rho_{Ref}}}, \tag{3.2}$$

Where $\rho_{Ref} = 1.0\text{kg/m}^3$ is a device-specific reference density and F is a shape factor taking into account differences in fluid response for different particle shapes ($F = 1$ in this case, as the particles are approximately spherical). $d_p = 12\mu\text{m}$ is the geometric diameter, which was measured as previously described. The aerodynamic diameter was measured with a TSI Aerodynamic Particle Sizer Model 3321 (APS) in a room of a volume of approximately 200 m^3. This room had several fans running, as well as an InoxAir GmbH air filter with a clean air delivery rate of 1650 $\frac{m^3}{h}$. These devices were used to ensure a homogeneous particle distribution in the local atmosphere as well as to filter out unwanted particles from the air. The full experiment went as follows: First, both fans and air filter were turned on for approximately 10 minutes in order to clean the air of particulate material. Afterwards, the APS started measuring the aerodynamic particle size distribution of this air, in order to characterize the background air of the experiment. After 5 minutes, particles were spread in the by using a commercial airbrush with a nozzle of 1 mm width. The airbrush was connected to a N_2 gas bottle, and discharged towards a fan pointing upwards, which then spread the particles in the air.

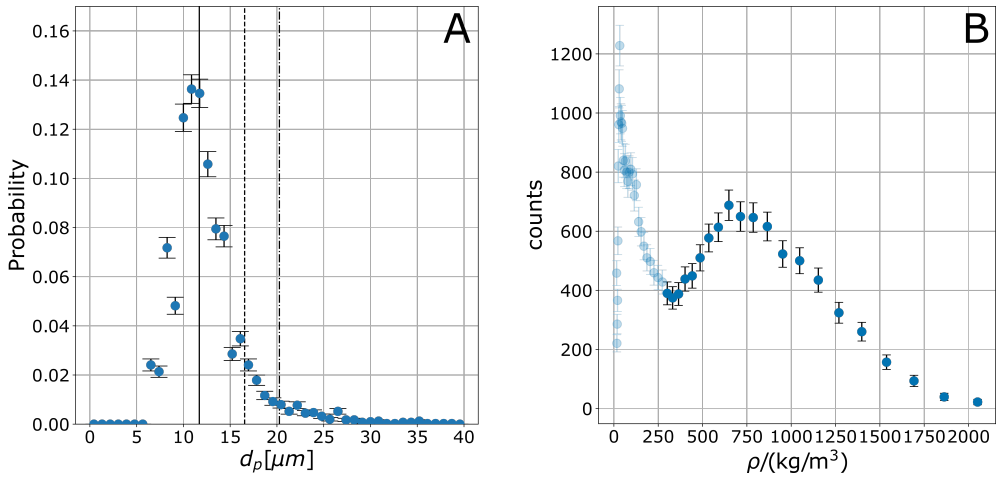

Figure 3.5: D-10 particle properties. **A**: probability of finding a particle of size d_p on the system after an experiment. Vertical lines indicate the expected size of clusters of one (solid line), two (dashed line) and three (dash and dot line) particles. The mean particle diameter for a single particle is $11.7 \pm 0.1\mu$m. **B**: Histogram of the particle density estimated from the aerodynamic particle size. The peak at low values (faded blue color) corresponds to a residue from a previous experiment, and can be ignored. An effective density of $\rho_p = (730 \pm 250)$ kg/m^3 is obtained by averaging the three highest points at the second peak (as well as the FWHM of the curve). By averaging the density bins weighted by their respective counts, a mean value of $\rho_p = 730 \pm 250$ kg/m^3 is obtained.

The aerodynamic particle size distribution measured by the APS was converted to density values, according to Equation (3.2), and the results are shown on Figure 3.5. There is a greyed region on the plot, corresponding to residues of a previous experiment done with a different set of (smaller) particles that were not filtered out completely. In the relevant region, the estimated density is $\rho = 730 \pm 250$kg/m^3.

Acceleration

Electrostatic forces could arise in our system due to friction between the particles or between particle and nozzle when ejected from the particle dispenser. If this is the case, these forces would be made apparent in the particle acceleration statistics. The acceleration of each particle has been calculated from their position as a function of time, following the process described in Sections 3.2.1 and 3.2.2. The average magnitude of the longitudinal acceleration between two particles $(\vec{a}_2 - \vec{a}_1) \cdot \frac{\vec{r}_2 - \vec{r}_1}{\|\vec{r}_2 - \vec{r}_1\|}$ as function of the inter particle pair distance can be seen in Figure 3.6. The average is consistently zero at all measured scales, which means that the particles, down to $r \approx 50\mu$m, are not being directly repelled or attracted to each other. In particular, this quantity does not follow a r^{-2}, as it would be expected from an electrostatic interaction.

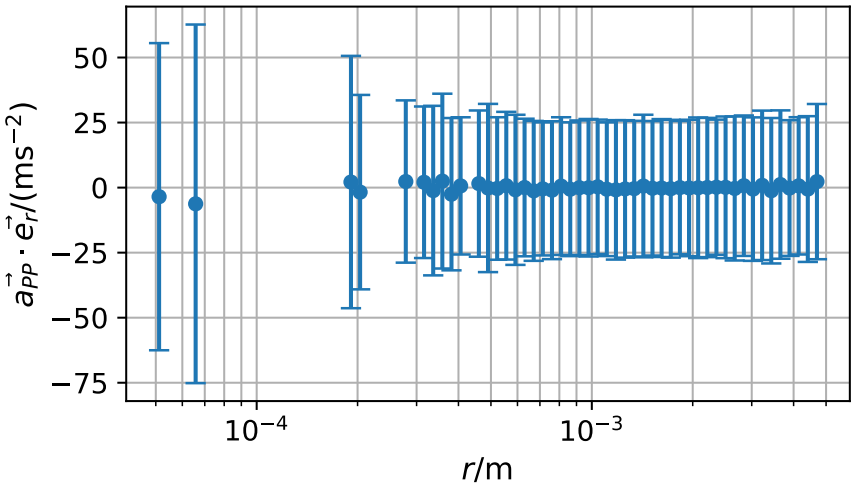

Figure 3.6: Mean particle-particle acceleration $\vec{a}_{pp}$projected to the normalized inter-particle distance vector $\vec{e}_r = \frac{\vec{r}}{\|r\|}$ as function of the particle pair distance r

The histogram of the angle ϕ between the relative acceleration between two particles and their distance vector is plotted in Figure 3.7. The relative acceleration between two particles is predominantly perpendicular with respect to their relative separation, with almost no occurrences of them being parallel or antiparallel. This is expected from incompressible flows, since the field is divergent free in this case.

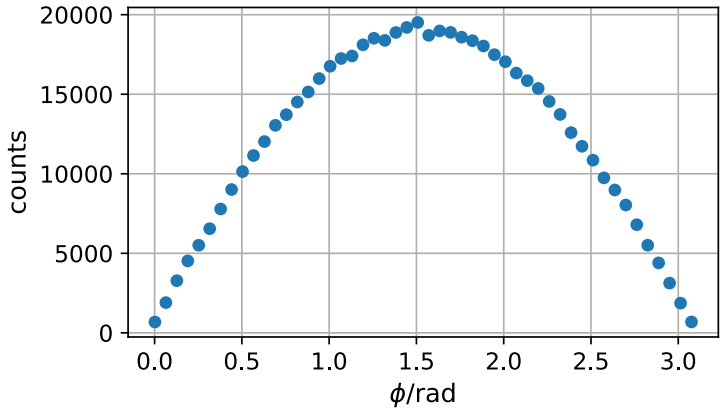

Figure 3.7: Histogram of the relative angle between the inter particle distance vector and their relative acceleration.

3.1.4 Particle disperser

In order to produce a reliable stream of tracers, an in-house particle disperser was designed, which can be seen on Figure 3.8. It consists of a large

cylindrical container of volume $\sim 10L$ which acts as a reservoir, and a small cavity connected to a SF_6 cylinder through a high pressure stainless steel braided hose. Two metal cones, connected to a motor on the upper side of the reservoir, can be moved up and down in order to promote particles to fall from the upper reservoir onto the cavity.

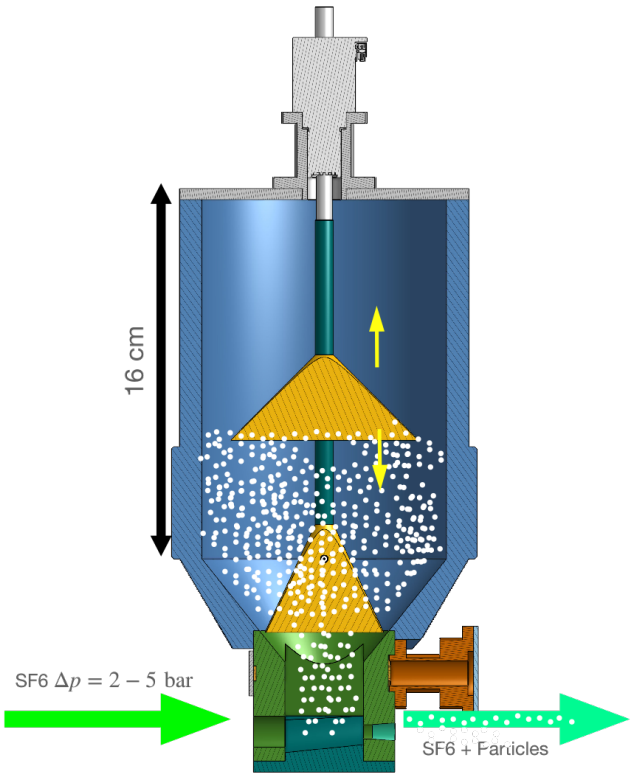

Figure 3.8: 2D rendering of the particle disperser vessel. Most of the particles are contained within the large reservoir (in blue) at the top part of the image, but some fall into the bottom receptacle (in green) by action of both gravity and two motor-controlled structures that stir the powder to avoid clumps (in yellow). An external SF_6 supply (2-5 bar above the VDTT pressure) is connected to the particle receptacle via a high pressure stainless steel braided hose, where the gas flow collects particles housed in the green receptacle. Two valves (not shown) control that the vessel is pressurized, and that the particles are released into the VDTT. Image courtesy of C. Kuechler

Two magnetic valves control the flow of an open SF_6 gas cylinder (set to pressures 2-5 bar above the current working pressure in the VDTT). When both valves are open, an airflow is created inside the bottom receptacle. This flow of air pushes the particles inside the container through another braided hose, carrying them to a small commercial airbrush nozzle, which then releases a cloud of mostly monodisperse particles, as seen from Figure 3.5.

In order to ensure that the particles at the measurement volume are unaffected by the jet flow of the ejection, the nozzle of the disperser is located downstream of the active grid, but upstream of the measurement volume.

Grid Protocol	$\langle U_{HW} \rangle$ [m/s]	$\langle u_{rms,HW} \rangle$ (streamwise) [m/s]	Re_λ	ϵ [$\mathrm{m}^2/\mathrm{s}^3$]	η [μm]	τ_η [ms]	Stokes number
LT1LT1	3.447	0.216	1305	0.062	34.1	2.66	0.14
LT2LT1.5	3.510	0.240	1481	0.068	32.7	2.51	0.15
LT4LT3	3.644	0.345	2233	0.107	27.6	1.92	0.20
LT7LT5	3.609	0.396	2680	0.129	26.4	1.75	0.22

Table 3.1: Turbulent flow parameters for each grid protocol obtained from previous hot-wire data. The Stokes number was calculated with the geometric diameter calculated from the microscope pictures and the density estimated from the aerodynamic particle size.

The nozzle points upwards at an angle $\alpha \approx 40°$, but is otherwise aligned to the main axis of the tunnel, about 15 cm to the left of its center.

3.2 Data acquisition and analysis

3.2.1 Data acquisition

Hot-wire data

The hot-wire data presented here was acquired several months prior to the realization of the LPT experiments [2]. Four different datasets with different grid protocols were taken, all of them with a constant pressure of 5.98 bar and a fan speed of 16.8 Hz for all of them. At this pressure, the kinematic viscosity and fluid density take the values $\nu = 4 \cdot 10^{-7}\mathrm{m}^2/\mathrm{s}$ and $\rho = 38.8\mathrm{kg}/\mathrm{m}^3$, respectively. The grid protocols chosen were LT1LT1, LT2LT1.5, LT4LT3 and LT7LT5. The meaning of this nomenclature can be found on Section 3.1.1. The measured values of Re_λ, as well as other relevant turbulence parameters can be seen on Table **??**. The Stokes number was calculated by using the flow parameters measured by the hot-wire, the fluid parameters corresponding for SF_6 at 6 bar and the mean particle density and diameter calculated on the previous section ($d_p = 12\mu\mathrm{m}$ and $\rho_p = 730\mathrm{kg}/\mathrm{m}^3$).

The hot-wire used were the nano scaled thermal anemometry probes (NSTAP) fabricated by Princeton [16]. The hot-wires were located approximately 2 m downstream from the measurement volume, but otherwise aligned with the measurement volume of the cameras and the major axis of the tunnel.

LPT data

For these experiments, the parameters used were the same as for the hot-wire measurements to allow a direct comparison. That is, same grid protocols

at a working pressure of 5.98 bar and with a fan speed of 16.8 Hz. All four cameras in the setup described previously were used to record videos. A typical frame can be seen on Figure 3.9. A heavy distortion on the shape of the otherwise spherical particles can be observed for one of the cameras (marked as 3 on Figure 3.9). Thus, the videos recorded by camera 3 were not considered for the subsequent tracking and image analysis. It was found that this distortion is related to small stresses in the mirror the camera uses to observe the measurement volume. These stresses slightly bend the mirror, and are caused by the clamping mechanism that affixes the mirrors to the kinematic mount and from small imperfections in the surface of the mirror holder.

The particle tracking has been done with Dr. Jan Molacek's in-house particle tracking code, which provides indexed 3D positions per frame, where the index corresponds to an identification number for each particle. The code provides as well a measure of the tracking errors associated to the particle position. This code is inspired by the Shake The Box algorithm [99]. This involves first extrapolating a position "candidate" from an already existing track. The distance of this candidate positions and the one from a particle position detected on the video is minimized. This is achieved by slightly varying (or "shaking") the coordinates of the candidate position. Once this is performed on each camera, the final particle position is extracted via line of sight triangulation. In this code, this is performed with several candidate positions at once. As this reduces the requirements on the temporal resolution for particle positions, it allows the tracking tracking of particles with higher accelerations or larger position uncertainties.

3.2.2 Data treatment

The raw data contains noise from several sources. These sources includes random noise from the trajectories as well as systematic errors, such as vibrations from the setup that are not fully damped by the suspension system. Another possible source of error are thermal plumes that come out of the camera. This noise must be filtered in order to be able to obtain meaningful statistics. One commonly used technique to filter and de-noise the signal is by Gaussian kernel filtering, due to both its simplicity in implementation [100] and the ease of calculation of the derivatives of the filtered quantities, which is simply using a differentiated Gaussian as a kernel [101]. Unfortunately, this method introduces a selection bias by cutting off the data at the edges of the

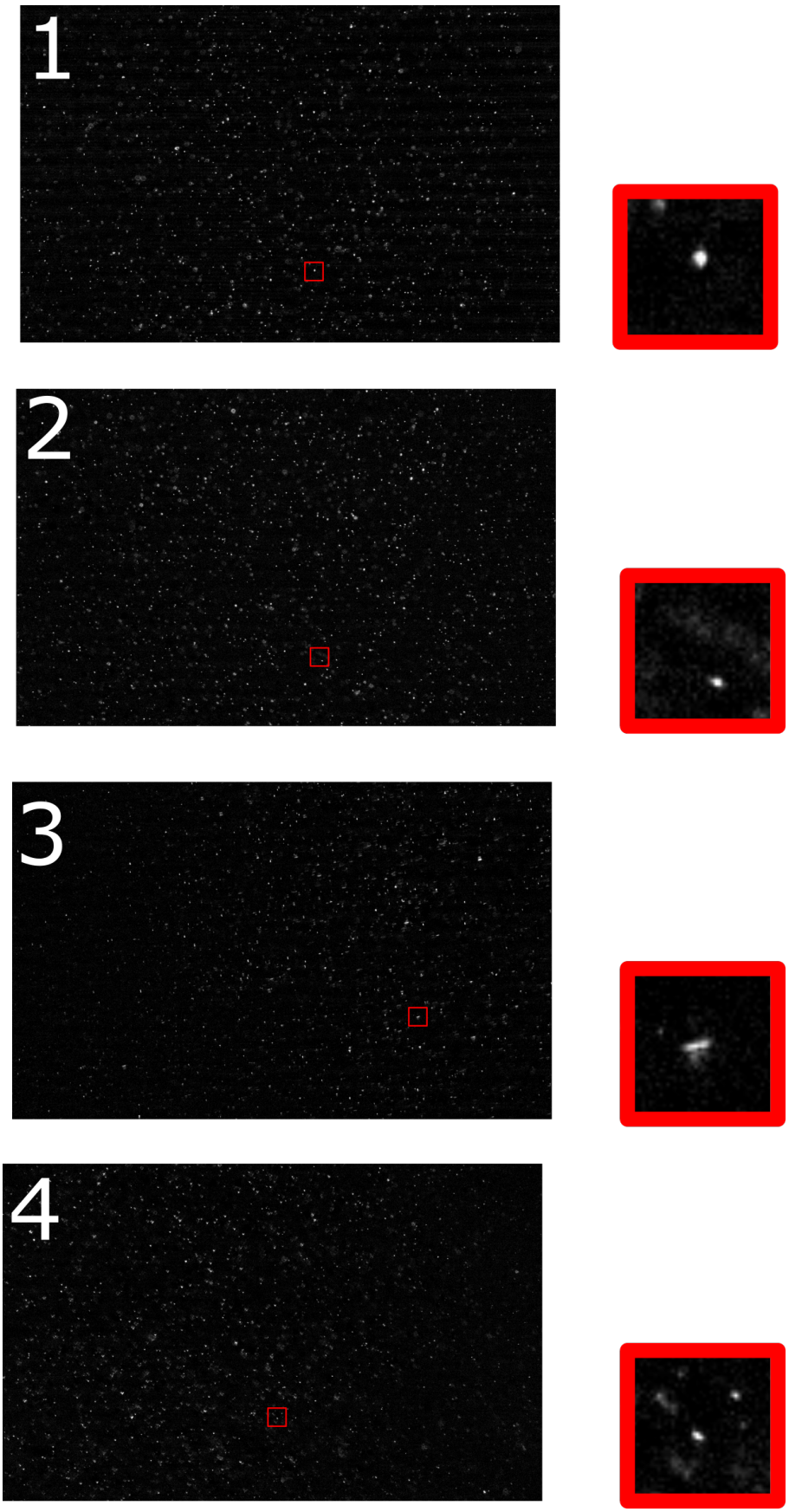

Figure 3.9: Left side: A characteristic frame for each camera in one experiment, with one particle marked by a red square. Right side: Magnification of the marked particle.

tracks, where there is too little data to properly support the filtering. Therefore, only the tracks inside a box shaped region of dimensions $(24, 22, 22)$ mm were considered. This box was centered at $x = 0$mm, $y = 2$mm and $z = -2$mm with respect to the center of the camera coordinate system. On this thesis work, the data has been smoothed by penalized cubic B-splines (or P-splines). As the splines are third order polynomials, we ensure that the smoothed tracks are twice-differentiable. The usage of P-Splines has been exhaustively documented since it's introduction [102] [103] [104].

P-Splines

This section is a brief outline of P-Splines. A full, detailed analysis of them can be found on [105].

In order to understand cubic P-splines, it is necessary to first discuss cubic B-splines. A cubic B-spline is a piecewise function, where each piece is a polynomial of order 3. Now, if a B-spline consisting on a basis matrix $\mathbf{B}$ with coefficients $\hat{\mathbf{a}}$ (so that $f(x) = \sum \mathbf{B_i}(x)\hat{\mathbf{a}}_\mathbf{i}$) is used to fit a curve $\mathbf{y}$, one needs to solve a least squares problem for $\hat{\mathbf{a}}$ with solution:

$$\hat{\mathbf{a}} = \left(\mathbf{B^T B}\right)^{-1} \mathbf{B^T y} \tag{3.3}$$

A P-spline solves a similar equation, but adding a "Penalizing term" $\lambda\mathbf{P}$, where $\mathbf{P}$ has the form $\mathbf{P} = \mathbf{D_3}^T\mathbf{D_3}$ with $\mathbf{D_3}$ that follows the relation

$$(\mathbf{D}_3\mathbf{a})_j = a_j - 3a_{j-1} + 3a_{j-2} - a_{j-3}$$

which add a constraint to the coefficients $\hat{\mathbf{a}}$ to minimize the roughness (defined as $\int |f''(x)|^2$)of the P-spline. The constant λ simply weights the smoothing term. The equation for the P-spline is:

$$\left(\mathbf{B}^T\mathbf{B} + \lambda\mathbf{P}\right)\hat{\mathbf{a}} = \mathbf{B}^T\mathbf{y} \tag{3.4}$$

To account for the error inherent in experimental data $\mathbf{y}$, a diagonal weight matrix $\mathbf{W}$, is also added, which takes into account the tracking error produced by the code. Finally, equation (3.4) becomes:

$$\left(\mathbf{B}^T\mathbf{W}\mathbf{B} + \lambda\mathbf{P}\right)\hat{\mathbf{a}} = \mathbf{B}^T\mathbf{W}\mathbf{y} \tag{3.5}$$

The smoothing code was implemented by Christian Kuechler, using the MATLAB algorithm found in [102]

3.2.3 Characterization

The smoothing algorithm also calculates the root squared error per component (RSE_i) of the new positions. All data with RSE_i larger than 10^{-6} were discarded, as they were deemed too noisy. The discarded data corresponds to roughly 30% of the total. The reasoning behind this, as well as the implications will be discussed in Section 3.4. Table 3.2 has a general overview of the track number before any sort of data discrimination (both by RSE and by considering the box shaped region mentioned in Section 3.2.2).

Grid protocol	N_{tracks} (before cut-off)	N_{tracks} (after cut-off)	<Part. Density> [Tracks/Video]	<T. Len> [s/τ_η]
LT1LT1	681686	413887	20694	1.95
LT2LT1.5	437122	271846	13592	2.16
LT4LT3	703215	439930	20949	2.73
LT7LT5	421464	256928	14273	3.08

Table 3.2: Overview of number of tracks per dataset before and after the error and position cut-offs are applied. The particle density per video, as well as the average track length (in units of τ_η) after the cut-off is applied is also provided

The particle density is not uniform in each video: In several of them, several thousand frames were devoid of particles. While the total particle density per video is rather low, several frames have several thousand of particles. This would mean that there is a systematic bias in these measurements as some parts of the turbulence are underrepresented with respect to others. Due to large scale intermittency, the flow statistics have a fat tailed distribution, which means this sampling bias would greatly affect the overall statistics.

In every case, the maximum track length was close 300 frames, which corresponds to a total travelled distance of $\approx$ 4.2cm. This value is very close to the size of the larger diagonal of the enclosing box $d \approx 3.9cm$, which means that some tracks span the full (valid) field of view. The track length, depending on the grid protocol, corresponds to 4 to 6 Kolmogorov times τ_η. The histograms of track length can be found on Figure 3.10. As both pressure and measurement volume are kept constant, larger values of ϵ leads to smaller τ_η, which in turn means longer normalized track lengths.

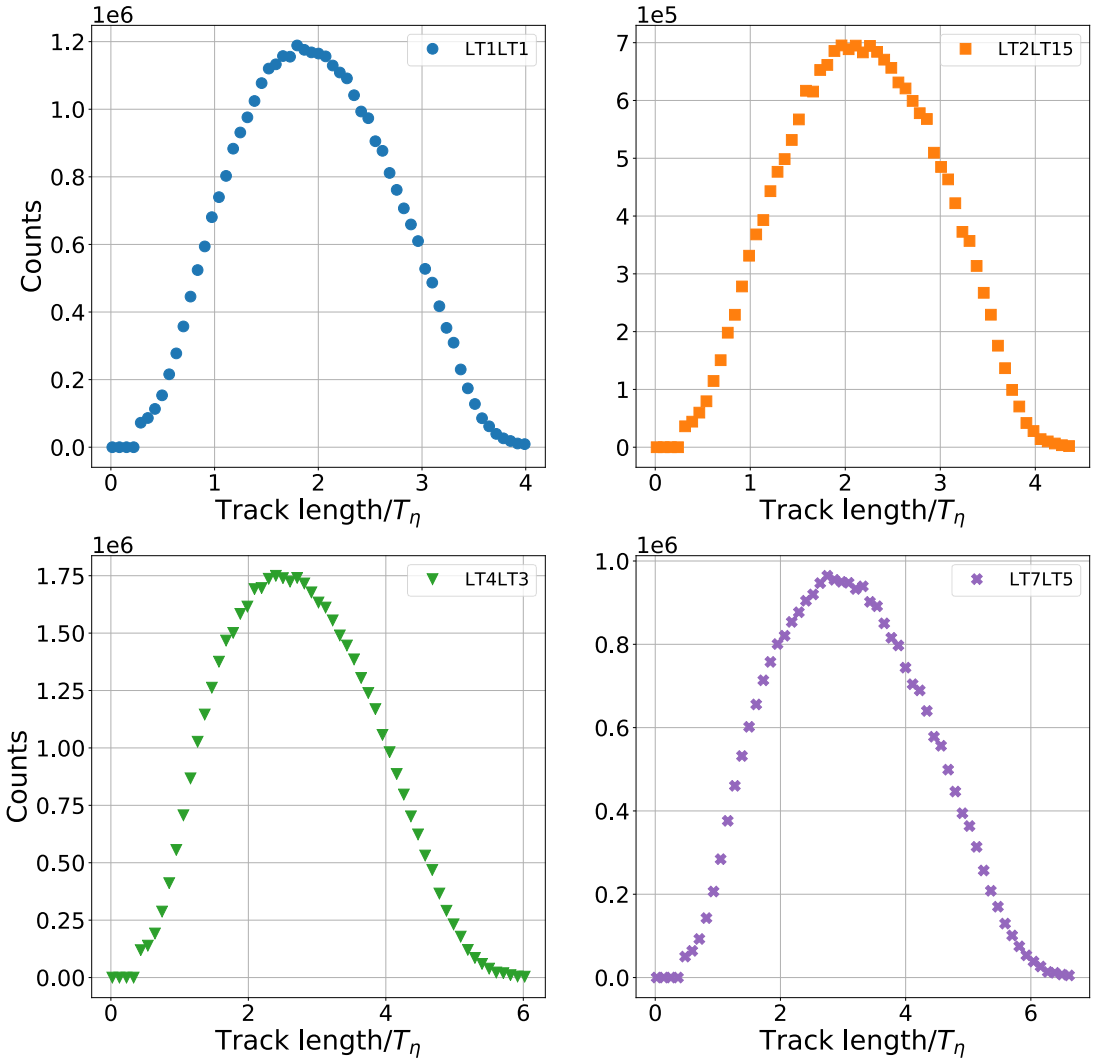

Figure 3.10: Histograms of the track length (in units of the Kolmogorov time τ_η found in each dataset: LT1LT1 (blue ●), LT2LT1.5(orange ■), LT4LT3 (green ▼) and LT7LT5 (purple ×).

As the mean track length is of order $2\tau_\eta$, it would only be possible to measure a part of the Lagrangian second order structure function $S_2^L(r)$:

$$S_2^L(\tau) = \left\langle (u_i(t+\tau) - u_i(t))^2 \right\rangle . \tag{3.6}$$

From a dimensional analysis under the assumptions done by Kolmogorov [30], $S_2^L(\tau)$ has a power law scaling similar to the scaling shown by the inertial range of the Eulerian structure function S_2 (see Section 1.5.2). The scaling has the shape:

$$S_2^L(\tau) = C_2(\epsilon\tau) \tag{3.7}$$

The Lagrangian inertial range begins at $\tau \approx \tau_\eta$ [106], thus it can only be partially observed on the current setup. For $\tau \ll \tau_\eta$:

Grid Protocol	$\langle U_{LPT} \rangle$ [m/s]	$\langle u_{rms,LPT} \rangle_{str}$ [m/s]	$\langle u_{rms,LPT} \rangle_{transv}$ [m/s]	$\langle u_{rms,LPT} \rangle_{str,transv}$ [%]
LT1LT1	3.881	0.171	0.164	4.58
LT2LT1.5	3.966	0.172	0.163	5.58
LT4LT3	4.086	0.241	0.230	4.65
LT7LT5	4.082	0.248	0.257	3.57

Table 3.3: Mean velocity and both streamwise ($\langle u_{rms,LPT} \rangle_{str}$) and transverse ($\langle u_{rms,LPT} \rangle_{transv}$) velocity values obtained from the particle tracks, as well as the relative difference $\langle u_{rms,LPT} \rangle_{str,transv}$ between both R.M.S values.

$$S_2(\tau)^L = a_0 \sqrt{\frac{\epsilon^3}{\nu}} \tau^2, \tag{3.8}$$

where a_0 is the normalized acceleration variance, which is a Re_λ dependent parameter [107].

Velocity Statistics

The total mean velocity, as well as the streamwise and transverse RMS velocities obtained from the LPT data can be seen on Table 3.3.

The normalized histogram of the streamwise velocities can be seen in Figure 3.11 accompanied with its respective hot-wire values. At low turbulence intensities (LT1LT1, LT2LT1.5), the velocity histograms of both LPT and hot-wire data have a similar shape. As the turbulence increases, an inhomogeneity effect starts to appear. This effect is also present in the hot-wire data, and has been previously reported [93]. One possible explanation is the decaying nature of the grid-generated turbulence [108]. It is observed that, for the hot-wire data, the effect is much more prominent, and that the measured mean velocity from the LPT data is systematically higher than the hot-wire measurements (as seen on Table **??**). Furthermore, a secondary velocity peak appears to manifest at a value higher than the mean for the LPT data. This is likely to be due to the previously described non-uniform particle density in each frame, which induces preferential sampling in highly seeded portions of the video.

The transverse and streamwise R.M.S velocity values, as well as the mean velocity obtained from the LPT data are listed in Table 3.3. The relative difference $\langle u_{rms,LPT} \rangle_{str,transv}$ between transverse and streamwise R.M.S values is defined as:

$$\langle u_{rms,LPT} \rangle_{str} = \frac{\| \langle u_{rms,LPT} \rangle_{transv} - \langle u_{rms,LPT} \rangle_{str} \|}{\frac{\langle u_{rms,LPT} \rangle_{str} + \langle u_{rms,LPT} \rangle_{transv}}{2}} \tag{3.9}$$

Grid Protocol	$\langle \overline{u}_{rms,LPT} \rangle$ (streamwise) [m/s]	$\langle \overline{u}_{rms,HW} \rangle$ [m/s]	$\frac{u_{RMS,LPT}}{u_{RMS,HW}}$
LT1LT1	0.171	0.216	0.792
LT2LT1.5	0.172	0.240	0.717
LT4LT3	0.241	0.345	0.699
LT7LT5	0.248	0.396	0.626

Table 3.4: Comparison between the R.M.S values of the stream-wise component measured by different techniques.

A relative difference no larger than 5.5% can be observed between stream-wise and transverse R.M.S velocities. This can be taken as a measure of the anisotropy of the flow.

The (streamwise) turbulence intensity of both LPT and hot-wire data, as well as the relative turbulence intensity with respect to hot-wire are listed in Table 3.4. It can be seen that u_{rms} obtained from hot-wire measurements $u_{rms,HW}$ is 21 to 37% larger than the u_{rms} obtained from LPT data, and the difference increases for increasing turbulence values. One possible reason is both preferential sampling due to both the Stokes number and the limited field of view of the camera setup.

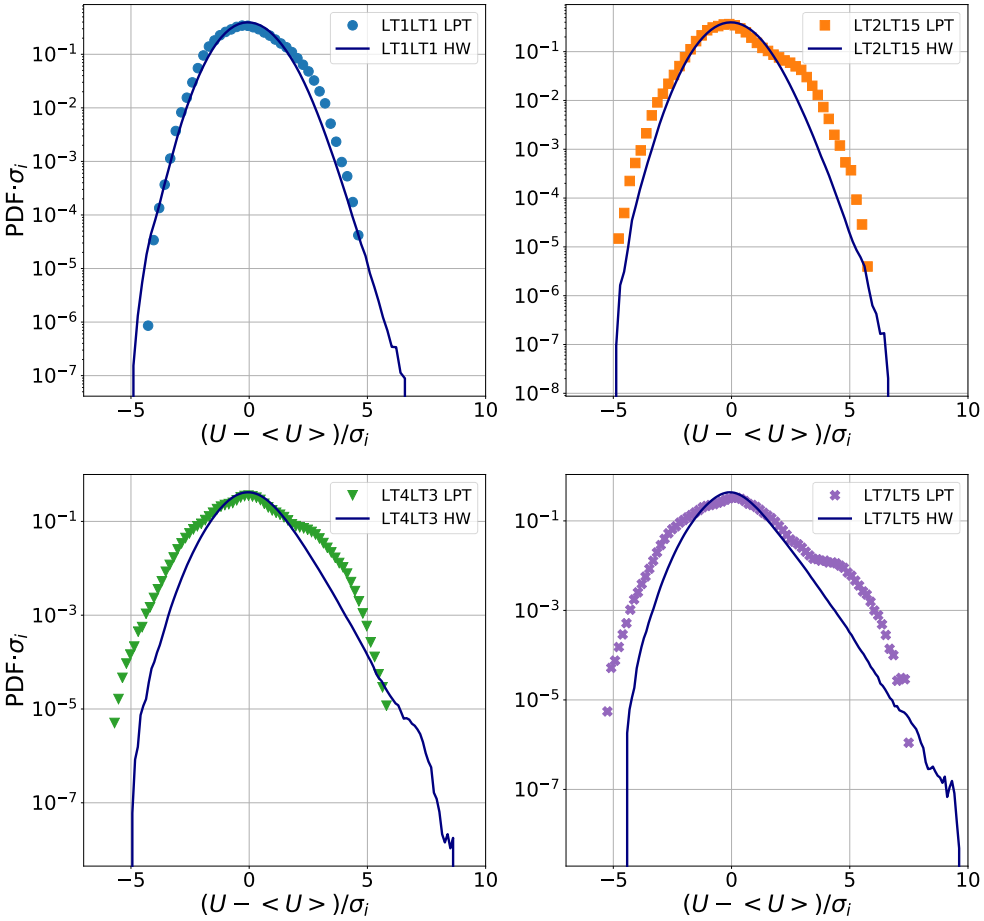

Figure 3.11: Compensated probability distribution function PDF $\cdot\, \sigma_i$ of the normalized streamwise velocity as function of their compensated velocity component ($\frac{\vec{U}-\langle\vec{U}\rangle}{\sigma_i}$) obtained from hot-wire measurements (navy blue) and from LPT for all 4 datasets: LT1LT1 (blue ●), LT2LT1.5(orange ■), LT4LT3 (green ▼) and LT7LT5 (purple ×). In all cases, σ corresponds to the standard deviation of the velocity measured for each experiment. Values for the mean velocity $\langle U \rangle$ for hot-wire and LPT data can be found Tables **??** and 3.3 respectively.

3.3 Particle Tracking Eulerian Statistics

3.3.1 Radial Distribution Function

The radial distribution function (RDF) (first introduced in Equation (1.59)) is an tool not only useful to observe the preferential concentration due to high Stokes number, but also to ascertain whether there are forces acting between the particles, such as electrostatic forces [109]. As the ideal tracer particles do not interact with each other, it is important to ascertain whether these forces are present in the system.

The equation for the RDF $g(r)$, as presented in Section **??**, is:

$$g(r) = \sum_i \frac{N_i}{\rho V_i}$$

where N_i is the number of particles which can be found inside a sphere of volume V_i (and radius r), centered on the particle i. $\rho = \frac{N}{V}$ is the average number density of particles in the entire volume.

This equation can also be defined as a comparison between the probability of a particle-pair having a separation r and a the probability of two particles of a uniform random distribution (Poisson's distribution) having a separation r. That is:

$$g(r) = \frac{P(r)}{P(\text{Poisson}, r)} \tag{3.10}$$

$P(r)$ is the probability of two particles being separated by a distance r. $P(\text{Poisson}, r)$ is the probability of two particles that are randomly and uniformly distributed (that is, they follow a Poissons distribution) being separated by a distance r.

The probability $P(r)$ can be calculated by following the procedure outlined by Saw [110], where $P(r)$ is approximated by the normalized histograms of the particle distances:

$$P(r) = \left\langle \frac{\sum_{sfr} \phi(fr, r)}{N_{fr}} \right\rangle_{fr,vid} \tag{3.11}$$

With $\phi(fr, r)$ being the number of particles in frame fr that are at a distance $(r - \frac{dr}{2}, r + \frac{dr}{2})$ from each other, and N_{fr} being the total number of particles found in frame fr. The brackets symbolize an average over all frames in one video, and of all videos in one dataset.

However, calculating the probability $P(r)$ in this way has the disadvantage of entangling the result with edge effects. The edge effects refers to the fact that the particles near the edges of the measurement volume have less neighbors compared to the particles at the center, which under-represents the larger particle-pair distances. This can be seen schematically on Figure 3.12

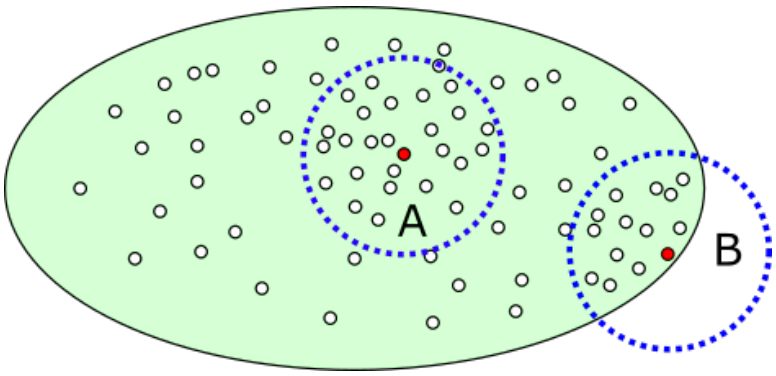

Figure 3.12: Schematic representation of the edge effect. The measurement volume is represented by the green ellipse, while the particles are the small circles. We can see that the colored particle has less neighbors around it at a certain distance R (represented by the blue dashed circle) compared to particle A, which is closer to the center of the measurement volume.

This effect will distort the resulting RDF introducing an artificial decay which grows with r. As this distortion is inherent to the system, it will be present on the Poisson distribution $P(\text{Poisson}, r)$ if it is calculated from the experimental data. As the position of the particles in turbulence is a random variable, this is possible. A Poisson distribution can be recovered from our data as long as many different uncorrelated positions are considered. As this Poisson distribution will be modified by exactly the same edge effects that our probability $P(r)$ has, these effects will cancel out when dividing the two quantities. $P(\text{Poisson}, r)$ has been calculated from the experimental data by first creating a "super-frame" that includes the positions of all particles every 500 frames. As the particles do not stay in the measurement volume for more than 300 frames, this criteria ensures that no particle is considered twice for the generation of this random distribution. From this super-frame, the quantity $P(\text{Poisson}, r)$ is calculated using an expression similar to $P(r)$:

$$P(\text{Poisson}, r) = \left\langle \frac{\sum_{fr} \phi(sfr, r)}{N_{sfr}} \right\rangle_{fr,vid} \tag{3.12}$$

The resulting RDF as function of the normalized distance $\frac{r}{\eta}$ for the different experiments can be seen on Figure 3.14. The maxima of the RDF is not

constant, instead increasing for larger turbulent intensities. Since the particles used for all experiments have similar characteristics, this means that the maxima is proportional to the Stokes number. This has been observed before for monodisperse particles, and is evidence of preferential clustering [111].

The results have been compared by plotting them next to previously published RDFs for "quasi monodisperse" particles in a turbulent flow [110]. The term "quasi monodisperse" refers to particles with a Stokes number with a 0.01 dispersion from their mean value. The resulting RDFs from the LPT data, alongside values from previously published simulation values [110] are plotted in Figure 3.13 for $r = 2\eta$ to $r = 10\eta$. The data was recovered from the publication by using [85]. At low r values, the measured RDF is higher than the simulated values at similar Stokes number, which also points toward preferential concentration effects. At higher r values, both the experimental error and the intrinsic error from the simulation data recovery procedure, it is not clear to which curve adjusts better to the data.

In Figure 3.14, it is observed that RDF decays to 1 at larger r values without a region where $g(r) < 1$. This differs from the expected behavior from charged particles [109] [112], where the RDF is expected to be smaller than 1 at the point where electrostatic forces win over turbulent forces: either by repulsion or by attraction (in which case they would also clump together). This is evidence that the particles are not charged, or that the resulting force is much weaker than the turbulent force.

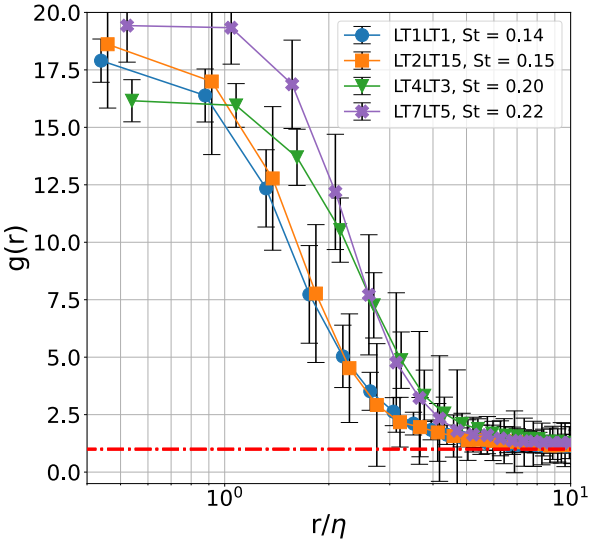

Figure 3.14: RDF as function of the normalized particle pair distance r/η for different grid protocols: LT1LT1 (blue ●), LT2LT1.5(orange ■), LT4LT3 (green ▼) and LT7LT5 (purple ×). The red dashed line equals to $y = 1$.

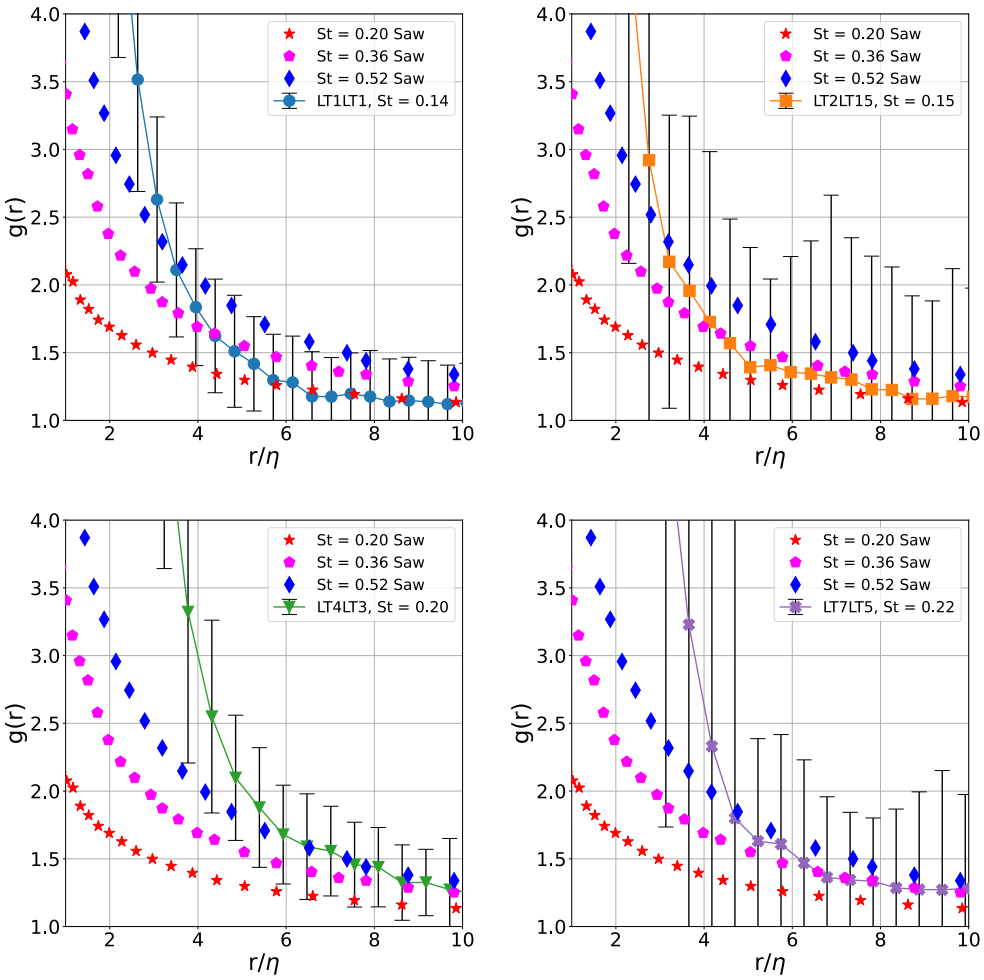

Figure 3.13: RDF obtained from LPT setup at different grid protocols compared to RDFs obtained from simulations at different Stokes number published by Saw (2008). Grid protocols used were LT1LT1 (blue ●), LT2LT1.5(orange ■), LT4LT3 (green ▼) and LT7LT5 (purple ×). Simulation data correspond to quasi mono disperse data at Stokes numbers 0.2 (red ★), 0.36 (magenta ⬟) and 0.52 (dark blue ⧫)

3.3.2 Second order structure function

The second order longitudinal structure functions were calculated from the LPT data and compared with the previously acquired hot-wire data. The goal is to further characterize the LPT statistics when compared to the more standard hot-wire statistics. Note that all quantities shown here are based on the relative particle position r, and as such are Eulerian statistics.
The equation used for calculating the second order, time averaged, longitudinal Eulerian structure function is:

$$S_2(r) = \left\langle \left\langle \Phi_{fr} \left(\left(\Delta\vec{v}_{ij} \cdot \hat{r}_{ij} \right)^2, r \right) \right\rangle_{fr} \right\rangle_{vid} \tag{3.13}$$

Where $\Delta\vec{v}_{ij}$ is the velocity difference between particles i, j, $\hat{r}_{ij} = \frac{\Delta\vec{x}}{\|\vec{x}\|}$ is the normalized distance vector between the pair i, j and $\Phi_{fr}(K_{i,j}, r)$ is the average of the quantity $K_{i,j}$ for all particle pairs in frame fr that are separated by a distance $\left(r - \frac{dr}{2}, r + \frac{dr}{2}\right)$. The brackets $\langle\cdot\rangle_f r$ and $\langle\cdot\rangle_f r$ denote an average per frame and per video, respectively.

Similarly, the second order, time averaged, transverse Eulerian structure function is defined as:

$$S_{2,\perp}(r) = \left\langle \left\langle \Phi_{fr}\left(\left(\Delta\vec{v}_{ij} \times \hat{r}_{ij}\right)^2, r\right)\right\rangle_{fr}\right\rangle_{vid}, \tag{3.14}$$

where $\times$ is the cross product. Note that the second order structure function D_2, defined as:

$$D_{ij}(r) = \left\langle (u_i(r+x) - u_i(r))(u_j(r+x) - u_j(x))\right\rangle, \tag{3.15}$$

is a rank two tensor. For an isotropic flow, this tensor becomes uniquely defined by its diagonal components D_{ii} when evaluated in an orthogonal reference frame aligned to the relative position vector between two particles (as shown in Section 1.5.2.). It is possible to rewrite $\Delta\vec{v}_{ij}$ in this reference frame, obtaining:

$$\Delta\vec{v}_i j = v_0\hat{r}_{ij} + v_1\hat{n}_1 + v_2\hat{n}_2. \tag{3.16}$$

By rewriting $\Delta\vec{v}_{ij}$ in this reference frame, $S_{2,\perp}$ becomes:

$$\begin{aligned}
S_{2,\perp} &= \left\langle \left\langle \Phi_{fr}\left((\Delta\vec{v}_{ij} \times \hat{r}_{ij})^2, r\right)\right\rangle_{fr}\right\rangle_{vid} \\
&= \left\langle \left\langle \Phi_{fr}\left((v_2\hat{n}_1 - v_1\hat{n}_2)^2, r\right)\right\rangle_{fr}\right\rangle_{vid} \\
&= \left\langle \left\langle \Phi_{fr}\left((v_1^2 + v_2^2), r\right)\right\rangle_{fr}\right\rangle_{vid} \\
&= \left\langle \left\langle \Phi_{fr}\left(v_1^2, r\right)\right\rangle_{fr}\right\rangle_{vid} + \left\langle \left\langle \Phi_{fr}\left(v_2^2, r\right)\right\rangle_{fr}\right\rangle_{vid} \\
&= D_{N1} + D_{N2},
\end{aligned} \tag{3.17}$$

where the associativity of the sum has been used to separate the averages $\langle\cdot\rangle$ and $\Phi_{fr}(K, r)$. Note that, if the flow is isotropic and homogeneous, $D_{N1} + D_{N2} = 2D_{NN}$.

Longitudinal second order structure function

The longitudinal second order structure function calculated from the LPT data $S_{2,LPT}$ was calculated following Equation (3.13), and is plotted alongside the longitudinal second order structure function calculated from previous hot-wire measurements ($S_{2,hw}$) on Figure 3.15.

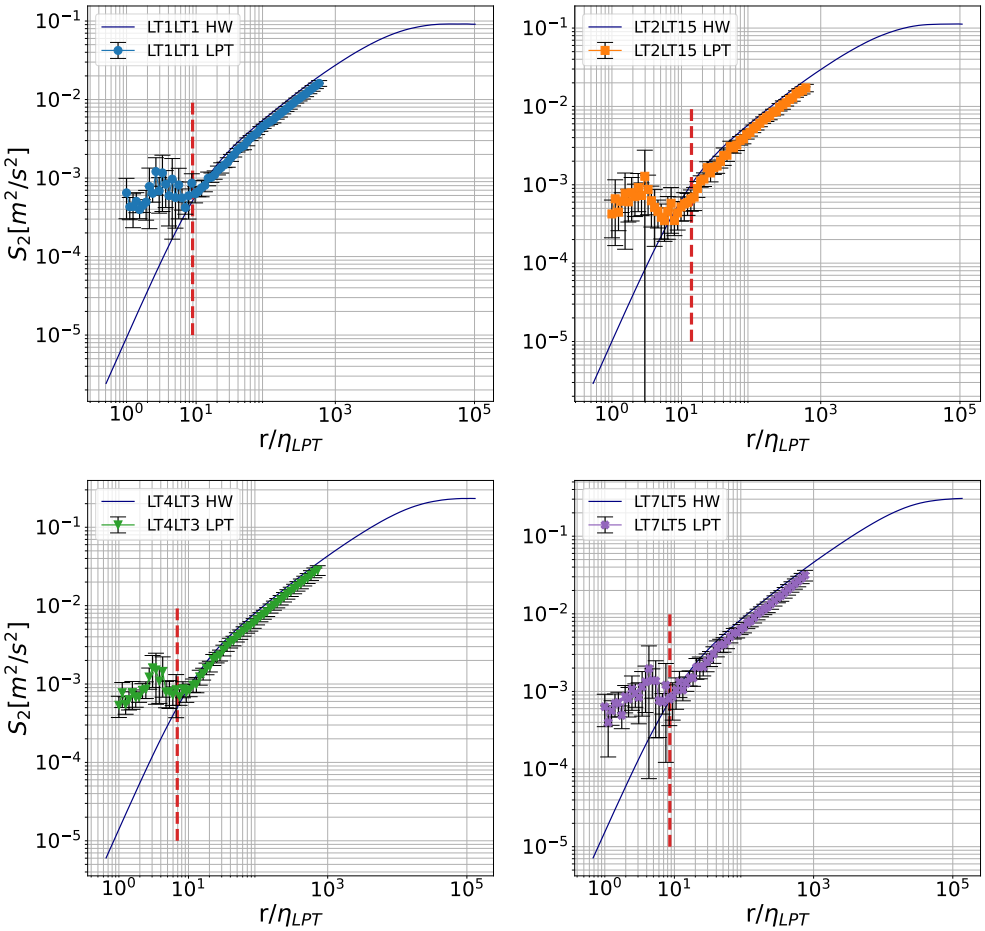

Figure 3.15: Second order longitudinal structure function obtained from the LPT setup $S_{2,LPT}$ for different grid protocols, compared to the second order structure function obtained from hot-wire data $S_{2,HW}$. LT1LT1 (blue ●), LT2LT1.5(red■), LT4LT3 (green ▼) and LT7LT5 (purple ×). The hot-wire data is represented as a solid navy blue line in all cases. Red dashed line marks the point where $S_{2,LPT}$ starts to differ from $S_{2,HW}$ at lower values of r

$S_{2,LPT}$ only extends up to $r \sim 0.02$ m as this corresponds to the diameter of the largest sphere that can fit inside the measurement volume. It can be observed that, down to a certain inter particle distance r_c, the structure function $S_{2,LPT}$ has a similar shape than $S_{2,HW}$, albeit consistently smaller. For $r < r_c$, $S_{2,LPT}$ starts to diverge from the hot-wire data and the expected behavior. In order to estimate r_c, the relative difference was used. For two datasets $S_{2,LPT}$

and $S_{2,HW}$, the (percentual) relative difference R_{diff} is defined as:

$$R_{diff}(r) = 100 \frac{\|S_{2,LPT}(r) - S_{2,HW}(r)\|}{\frac{S_{2,LPT}(r)+S_{2,HW}(r)}{2}}, \tag{3.18}$$

The cut-off value r_c has been defined as the smallest r value such that:

$$\left\langle R_{diff} \right\rangle_{r \geq r_c} \leq 5.7, \tag{3.19}$$

where $\left\langle R_{diff} \right\rangle_{r \geq r_c}$ denotes an average of $R_{diff}(r)$ over all $r \geq r_c$. The r_c obtained for each dataset have been listed on Table 3.5

Grid protocol	r_c [μm]	$\frac{r_c}{\eta}$
LT1LT1	330	9.66
LT2LT1.5	496	15.16
LT4LT3	259	9.30
LT7LT5	251	9.44

Table 3.5: Inter-particle distance where the shape of $S_{2,LPT}$ noticeably differs from $S_{2,HW}$, both in μ m and in units of its respective η

The inertial range, where $S_2 \sim r^{2/3}$ can be clearly distinguished, which permits the caculation of the energy dissipation rate ϵ_{LPT} from Kolmogorovs K41 theory. These values, as well as a comparison with the energy dissipation rate obtained from hot-wire measurements ϵ_{HW} can be seen on Table 3.6.

On Figure 3.16, the structure functions have been compensated by $2(\epsilon r)^{3/2}$, where ϵ corresponds to their respective energy dissipation rate values. The compensated structure functions overlaps down to $r \sim r_c$ (marked as a red vertical line), where the deviation is apparent.

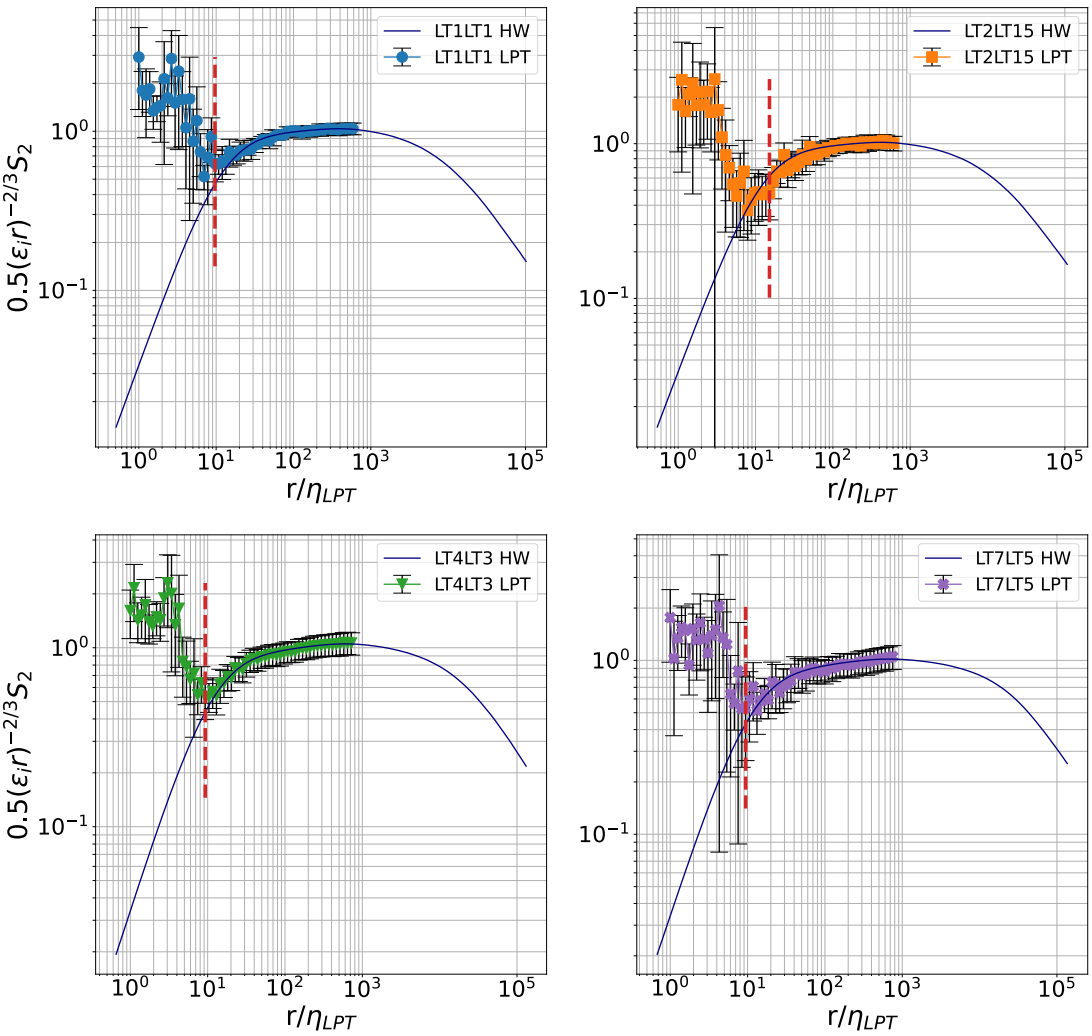

Figure 3.16: $S_{2,LPT}$ compensated by K41 theory for each grid protocol plotted alongside the compensated $S_{2,LPT}$, with the cut-off distance $\frac{r_c}{\eta}$ marked as a red dashed line. LT1LT1 (blue ●), LT2LT1.5(red■), LT4LT3 (green ▼) and LT7LT5 (purple ×). Hot-wire data as a solid navy blue line. Each structure function was compensated using their respective ϵ values.

As stated before, ϵ_{HW} is consistently 20 to 30% larger than ϵ_{LPT}, the difference being larger for larger turbulence intensities. This is consistent with the differences observed in the u_{rms} seen on Table 3.4, as $\epsilon \sim \frac{u_{rms}^3}{L}$, and the underlying causes are the same.

Grid protocol	ϵ_{HW}	ϵ_{LPT}	$\frac{\epsilon_{LPT}}{\epsilon_{HW}}$
LT1LT1	0.047	0.036	0.78
LT2LT1.5	0.056	0.043	0.77
LT4LT3	0.107	0.080	0.75
LT7LT5	0.129	0.094	0.73

Table 3.6: ϵ as function of the grid protocol, as calculated form hot-wire data (ϵ_{HW})and particle tracking ϵ_{LPT}, as well as the fraction between both F = $\frac{\epsilon_{LPT}}{\epsilon_{HW}}$.

Isotropy relationship

By using Equation (3.14), the transverse second order structure function $S_{2,\perp}$ was calculated. If the flow is isotropic and homogeneous, the relationship $S_{2,\perp} = \frac{3}{8}S_{2,LPT}$ must hold. In Figure 3.17, $S_{2,LPT}$ can be seen plotted alongside $\frac{3}{8}S_{2,\perp}$ for all 4 grid parameters, alongside $S_{2,HW}$ for comparison

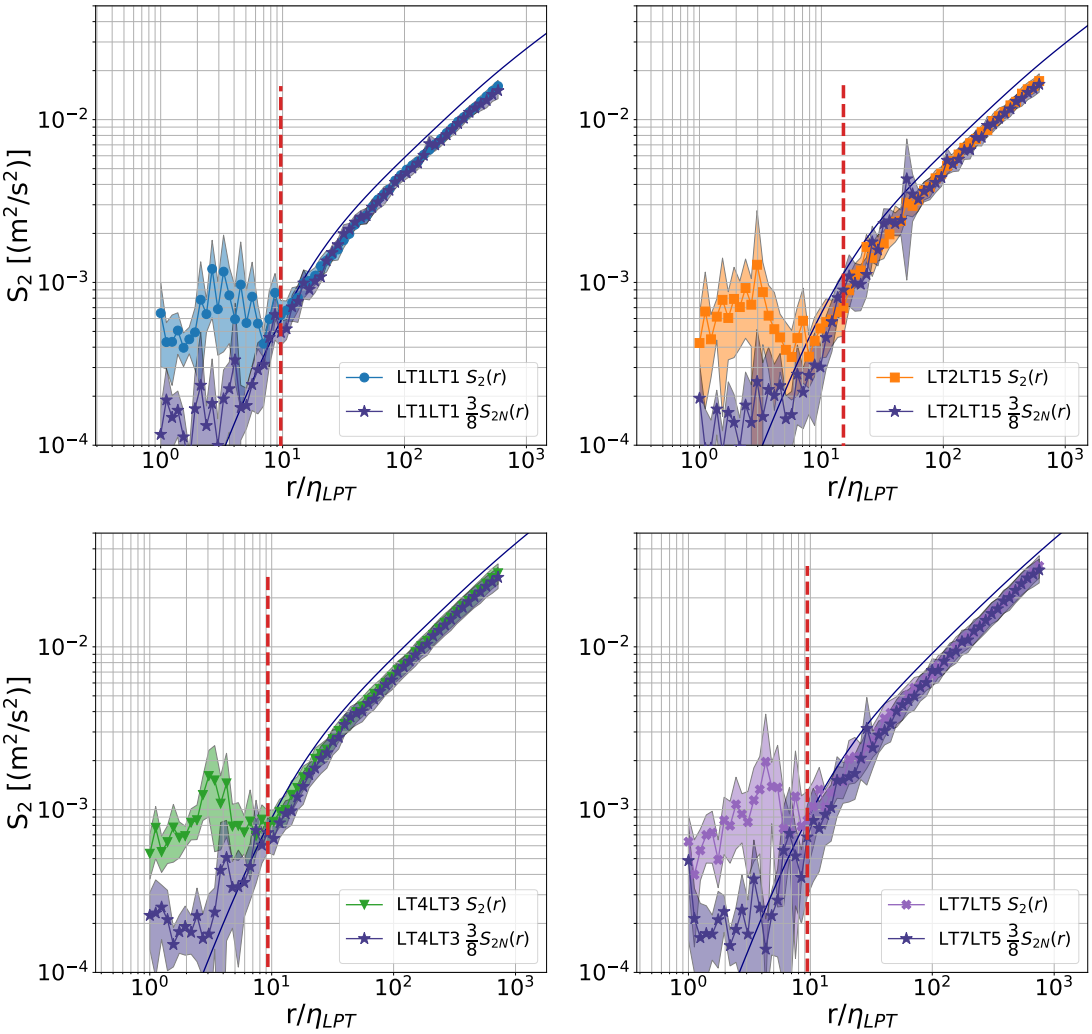

Figure 3.17: $S_{2,LPT}$ plotted alongside its respective $\frac{3}{8}S_{2,\perp}$ and $S_{2,H.W}$ for all grid parameters, with the cut-off value $\frac{r_c}{\eta}$ shown as a vertical red dashed line. For $S_{2,LPT}$ the symbols are: LT1LT1 (blue ●), LT2LT1.5(red■), LT4LT3 (green ▼) and LT7LT5 (purple ×). The hot-wire data is represented as a navy blue line in all cases, while the respective $\frac{3}{8}S_{2,\perp}$ is represented as dark purple ★ in all cases. The error bars of the LPT data has been represented as a shaded area in all cases.

A very good agreement between both $S_{2,\perp}$ and $S_{2,LPT}$ is found for $r > r_c$, within experimental error. At $r < r_c$ (to the left of the vertical dashed line), differences between these two functions arise. It is observed that, if $r < r_c$, the values of $S_{2,\perp}$ appear to be closer to the expected shape of $S_{2,HW}$ than $S_{2,LPT}$, even within experimental error.

The overlap between $S_{2,LPT}$ and $S_{2,\perp}$ has been quantified by the relative difference R_{diff} between both functions. The relative difference can be seen in Figure 3.18. The data for $r < r_c$ has not been considered for this scenario as both results diverge qualitatively from the known behavior observed in $S_{2,HW}$.

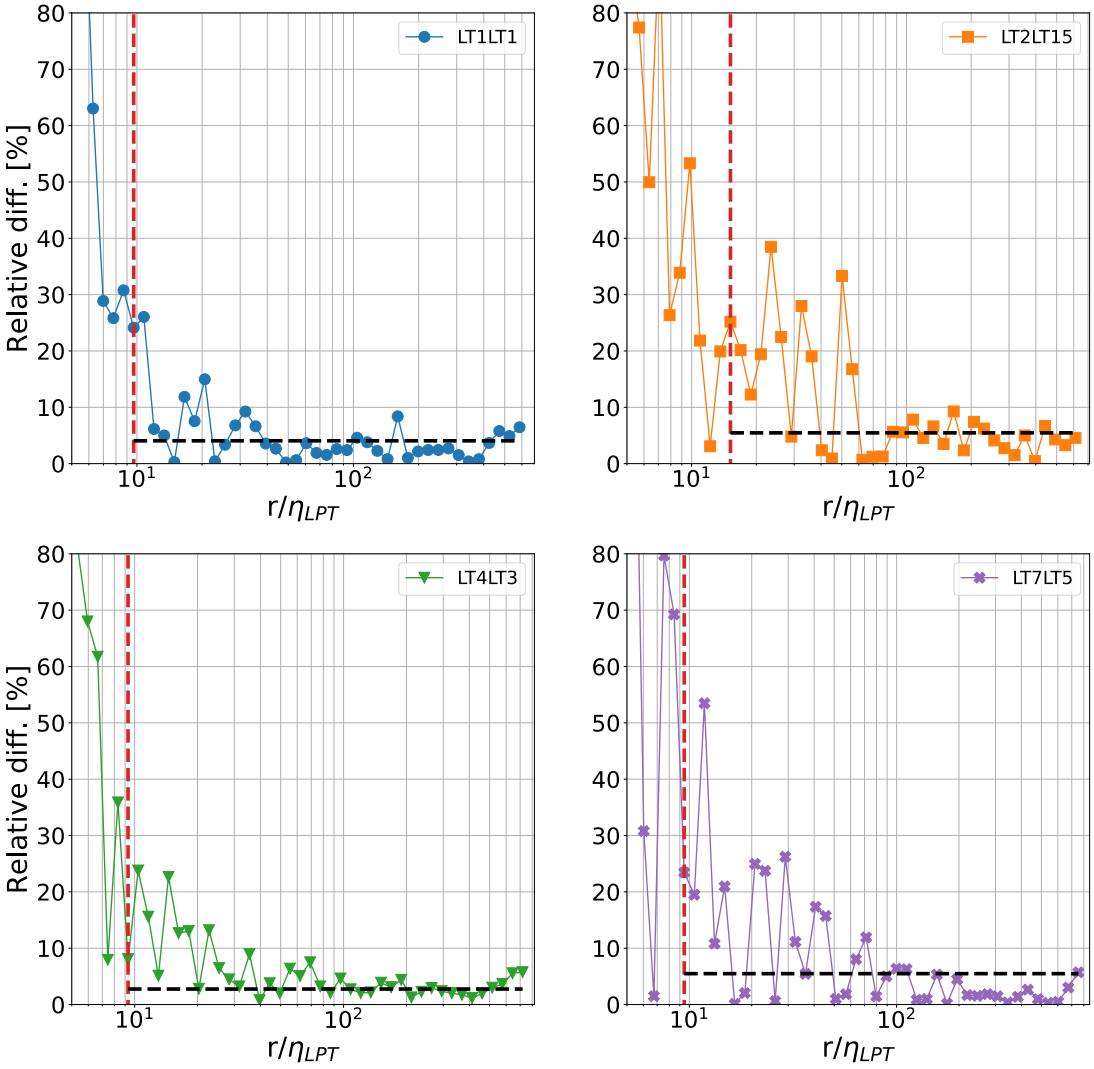

Figure 3.18: Relative difference between $S_{2,LPT}$ and $\frac{3}{8}S_{2,\perp}$ for different grid parameters: LT1LT1 (blue ●), LT2LT1.5(red■), LT4LT3 (green ▼) and LT7LT5 (purple ×). The red dashed line corresponds to $\frac{r_c}{\eta}$, while the black horizontal dashed line corresponds to the average of the relative difference for all values of r larger than r_c $\left\langle R_{diff} \right\rangle_{r \geq r_c}$

Note that the data is noisy for $r < 1$ mm, which means that definite statements regarding the isotropy of the flow require further investigations. However, it is expected [113] that the anisotropy goes down as the scales go down, which is in direct contradiction to what is observed for $r < 1$mm. Thus, this is likely to be caused by the same effect that produces the unexpected behavior at $r = r_c$ exists, which extends up to $r \sim 10^{-3}$. The average $\left\langle R_{diff} \right\rangle_{r \geq r_c}$ for $S_{2,LPT}$ and $S_{2,\perp}$ for all four datasets are shown in Table 3.7.

Grid protocol	$\langle R_{diff} \rangle$ [%]	Standard dev [%]
LT1LT1	4	6
LT2LT1.5	5	6
LT4LT3	3	4
LT7LT5	6	7

Table 3.7: Average and standard deviation of the average relative difference at $r \geq r_c$ $\left\langle R_{diff}(r) \right\rangle_{r \geq r_c}$ between the transverse and longitudinal second order structure function for all grid parameters studied.

3.4 Discussion

Over the course of this thesis, the already existing LPT setup such that particles of $d_p \leq \eta$ can be used. This particles are half the minimum size the previous iteration of the setup was able to resolve, which translates to a particle response time τ around four times smaller, which translates to an improvement in temporal resolution of the same order. Knowing the particle response time is vital, as this value should be negligible when compared to the dissipation time scale τ_η. This requires a precise measurement of the particle size and density (see Section 1.6. This thesis offers a direct measurement of the diameter and size dispersion of the particles used, as well as an improvement over the approximation used in [93]. A density of $\rho = 730 \pm 250 \text{kg/m}^3$ was obtained, which is significantly lower than the bulk density of cellulose [114]. This indicates that the particles are not solid, but instead have several voids in them, which makes them lighter. The large uncertainty on their mean density could be caused by a large porosity distribution in the particles.

With both density and particle diameter, is possible to obtain the Stokes number of the particle laden flow at different parameters (pressure and turbulence energy rate of dissipation). For the experiment, the maximum value calculated was $\text{St} = 0.22$. This number, as observed in the RDF, is enough to manifest preferential concentration effects. This is expected to be more pronounced at larger pressures, as St scales with ν^{-2}. At the extreme case of 15 bar, $\text{St} \leq 0.56$, which means the particles will not behave like ideal tracers.

The data acquired from the process described in Sections 3.2.1 and 3.2.2 is not free from noise. From the second order structure function, one can set a threshold value for the root squared error that minimizes the amount of noise without losing too much data. Selecting a threshold of $RSE = 10^{-6}$ means that $\sim 38.6\%$ of the data is deemed too noisy for analysis. This is a relevant

factor to consider when deciding the minimum number of experiments required to achieve statistical convergence. The analysis behind the choice of threshold has been done based on the comparison of the second order structure function obtained both via hot-wire and the LPT setup, and it can be found later in this section.

For these experiments, the average track length (in units of τ_η) are no larger than 3.08, although larger tracks can be observed, up to a maximum > 6, depending on the turbulence parameters. While insufficient to obtain the complete second order structure functions, (which would require lengths of the order 10 to $100\tau_\eta$ [115]), it is still possible to record part of it (as it starts from $\tau \sim 2\tau_\eta$ [106]) as well as meaningful statistics of Lagrangian accelerations [107] [116]. When observing the LPT streamwise velocity statistics, a consistently lower turbulent intensity was observed when compared to hot-wire data. This phenomenon can be explained by a combination of large scale intermittency, preferential concentration and sampling bias. As discussed in Section 1.5.9, intermittency generates more extreme velocity gradients as turbulence increases, which in turn means that more extreme events are observed. This can be an explanation for the gradual widening of the curves. At the same time, however, the large velocity events are being underrepresented due to a sampling bias inherent to LPT. The tracks of a particle p_1 with mean velocity $\langle u_1 \rangle$ are comparatively shorter than the tracks of a particle p_2 with mean velocity $\langle u_2 \rangle$ if $\langle u_2 \rangle > \langle u_1 \rangle$. This, due to the way the code obtains the particle position, means that the error associated to p_1 is likely to be larger than the error associated to p_2, which could result in a discarded track. As the extreme velocities are filtered out, $u_{rms} = \left\langle (u - \langle U \rangle)^2 \right\rangle$ is also expected to be lower than the hot-wire data. From this, as ϵ is related to u_{rms}^3, the energy dissipation rate is also lower. Another important factor is the fact that the LPT setup can not measure the entire inertial range. Due to the camera maximum field of view, it is only possible to observe quantities spaced $\approx$ 3cm apart. From the hot-wire data, however, it is easy to see that the inertial range end well beyond 5cm for all four grid protocols (as seen in Figures 3.15). The fact that there are scales larger than 5cm and preferential concentration could explain the large amount of empty frames observed in each video (as reported in Section 3.2.3): If an eddy of length of the order of the measurement volume (or larger) passes through the camera, it will be undersampled as most particles are dispersed away from it due to preferential concentration effects.

The longitudinal second order structure function $S_{2,LPT}$ has been calculated from the Lagrangian tracks. The resulting shape reasonably follow

the expected $r^{2/3}$ scaling up to a certain cutoff value r_c, where the function presents a large jump. This behavior is absent from the RDF, which would indicate that is related to velocity problems. A recent publication [117] proposes a scaling for isotropic and inhomogeneous flows which could help to remove some effects that are known to distort the statistics (i.e. particle finite size effects and insufficient statistics for the small scales). From the inertial range observed in $S_{2,LPT}$ (and for $r > r_c$) the energy dissipation rate ϵ_{LPT} was calculated and compared with the energy dissipation rate ϵ_{HW} calculated from hot-wire data using the same technique. It was found that $\frac{\epsilon_{LPT}}{\epsilon_{HW}} < 1$ for all grid protocol values studied. In order to investigate the possible relationship between r_c and the threshold parameter RSE, $\frac{S_{2,LPT}}{S_{2,HW}}$ has been plotted for different values of RSE_{max}, as can be seen on Figure 3.19 for experiment LT7LT5.

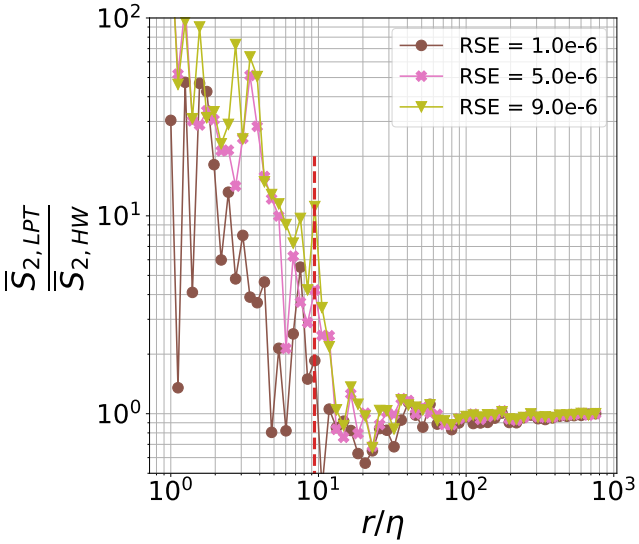

Figure 3.19: $R_{diff}(r)$ between $\frac{S_{2,LPT}}{\epsilon_{LPT}^{2/3}}$ and $\frac{S_{2,HW}}{\epsilon_{HW}^{2/3}}$ calculated for different threshold values of RSE.The red dashed line marks the threshold value for LT7LT5 $r_c = 9.44\eta$.

For the three values of RSE plotted, the lower threshold of $RSE = 10^{-6}$ produces slightly better statistics. To visualize this, $H(RSE) = \langle R_{diff} \rangle$ was calculated after obtaining $S_{2,LPT}$ and $S_{2,HW}$ using different RSE threshold values. RSE ranged from $7 \cdot 10^{-7}$ to $10 \cdot 10^{-6}$. The result can be seen graphically on Figure 3.20. It can be observed that H scales with RSE down to $H(10^{-6})$, which is very similar to $H(0.910^{-6})$. For values lower than $RSE = 10^{-9}$, H increases again, as there is not enough data to ensure statistical convergence of $S_{2,LPT}$ at the smaller scales, and the used averaging algorithm replaces the missing values with zeroes. The described effect of RSE on r_c, H and $\frac{S_{2,LPT}}{S_{2,HW}}$ are similar for different grid protocols.

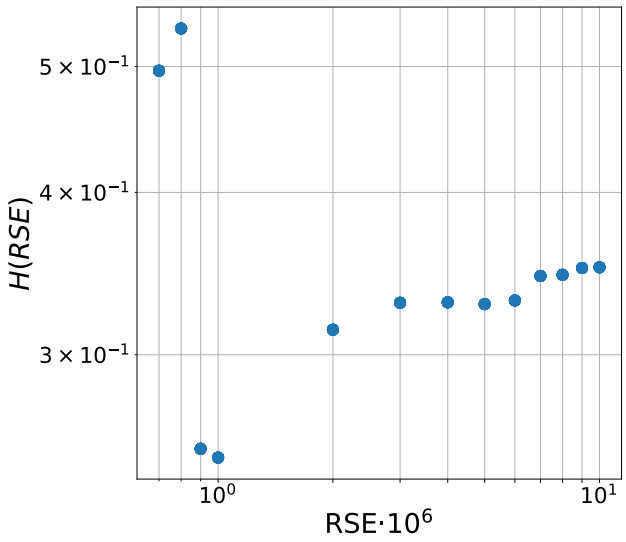

Figure 3.20: Relative difference between $S_{2,LPT}$ and $S_{2,HW}$ as function of the relative standard error threshold.

As r_c, as well as the magnitude of the divergence seem to be dependent on both RSE and the grid protocol studied, its cause is likely to be a sampling bias that needs to be investigated in further detail. Two times the Eulerian second order transverse function was calculated as well, and from this a measure of the isotropy was performed, as it is expected for the transverse and longitudinal structure function to be related by a factor $4/3$. The results show a very low anisotropy (no larger than 6%) at ranges $r > 1$mm, but an increase for smaller values. This is believed to be due to the same effect that causes the existence of r_c, as it is expected for the anisotropy of the system to decrease at smaller relative distances, and further investigation is required to discern the reasons for this. These low anisotropy values are also observed when considering the longitudinal and transverse RMS velocity (as seen on Table 3.4. The author notes that this is the first direct measurement of the degree of anisotropy in the VDTT with an active grid installed. This addresses concerns regarding the presence of strong anisotropies at small scales in the experiment. It is seen that these strong anisotropies are not present neither for moderately correlated grid protocols (such as LT1LT1) nor for strongly correlated grid protocols such as LT7LT5. This is evident as, in all cases, only a little divergence from the expected isotropy relation is present at the inertial scales. The latter is somewhat surprising [118][113], and motivates further research regarding the return to isotropy in flows at large Reynolds number.

Chapter 4

Summary and outlook

Fluid motion is ever present in nature. Despite that, the governing partial differential equations have yet to be solved succesfully, which motivates the acquisition of data via numerical of experimental methods to further refine our existing models. In this context, it seems that high turbulence data cannot be efficiently obtained from numerical experiments [21], which leaves either laboratory experiments or direct environmental measurements as the only viable way to obtain high Re statistics. Environmental measurements offer the advantage of having a readily available source of high Re flows in a variety of boundary conditions that are of scientific interest. At the same time, these experiments are difficult to realize due to both harsh conditions that forbid using most of the sensitive equipment available, and the inherent impossibility of controlling the experimental conditions of the field campaign. This makes the study of a more isolated phenomenon with high resolution data difficult. This motivates the search for both devices capable of working under hostile conditions that similar apparatus would break, as well as contrasting environmental results with well controlled lab experiments. This thesis provides a solution for obtaining velocity statistics in particle laden flows with a high mean velocity $(10 - 30\mathrm{m/s})$[14] [119] [120]), as well as insights on a novel high Re Lagrangian Particle Tracking setup which permits precise control of both the turbulence intesity of the flow as well as the Stokes number used on the system. This setup is proven to be isotropic even at the inertial range, and thus allowing the direct comparison of Eulerian and Lagrangian statistics obtained in laboratory conditions with Eulerian data obtained from environmental measurements.

4.1 Hot-wire for hostile environmental flows

In Chapter 2, the fabrication process of hot-wire using a CNF as its sensing element, alongside preliminary studies of its frequency response and measurement capabilities is presented. This CNF hot-wire is significantly more resistant than conventional hot-wires of similar dimensions, being able to withstand a direct collision with massive (mean diameter larger than 1mm) heavy particles without breaking. Even with non-ideal contact between CNF and prongs, the frequency response of this hot-wire appears to be similar to conventional Pt hot-wires, higher than 10kHz. Its fast response as well as natural sturdiness opens the possibility of measuring environmental flow velocity statistics in hostile weather conditions at a high Re, where conventional hot-wires would fail. In addition, the CNF hot-wire can be both calibrated and operated using already existing CTAs without any further modifications. Bluff body turbulence has been measured as a test case. While the results of this preliminary measurements are promising, further tests must be realized in conjunction with a conventional hot-wire to have a proper comparison of its measurement capabilities and limitations.

The hot-wire manufacturing process has room to improve on the bonding of the sensing element and prongs. The C-solder has a low melting point, which poses a problem as the hot-wire temperature changes and possibly starts melting the solder. On the other hand, the soldering process is not easily reproducible, resulting in hot-wires of different frequency response and maximum frequency range. Furthermore, the positioning of the hot-wire is not ideal, as affixing the sensing element to be perfectly perpendicular to the prongs is not easily reproducible. This is undesirable, as hot-wires are sensitive to their relative angle towards the incoming flow [121]. In order to overcome these problems, the author suggests to use prongs with a small channel-like indentation at their tips in order to properly hold and align the wire. Then, a small amount of a solder compatible with both carbon and stainless steel could be placed on top, and then the system soldered together via spot welding.

A possibility to circumvent the need to use C-Solder would be to plate the CNF with a metal that is easier to solder. One suitable candidate would be Cu, as electrodeposition of this metal on graphite is well known [122]. Another candidate would be Ni, as it is possible to create Ni-plated CNTs via electrodeposition as well [123]. As both Cu wires and Ni plated wires [124] are commonplace in electronics, a wider range of compatible solders exist for

them. Note that, if a different solder is to be used, it should have a higher melting point while being resistant to water corrosion and creating a strong mechanical bond between stainless steel and wire. Examples of suitable high temperature solders are Au based solders [125] and Sn based solders [126]. Nickel plated CNFs could even be subjected to high temperature soldering (brazing) as the metal coating would protect the underlying CNF from oxidation [127]. Suitable metal fillers are Au, Ag or alloys based on these metals [128]. Once properly affixed to the stainless steel prongs, the CNF could be exposed by etching the metallic plating away with acid, in the same way free-standing Pt wires are prepared from Wollaston wires [129]. In summary, this thesis shows the design and construction of a fast response, robust hot-wire that uses a carbon nanofiber as its sensing element. This makes it ideal for measurements in particle laden flows, such as free shear environmental measurements on clouds (ice clouds or otherwise) or boundary layer studies at very large Re. These studies are usually performed in towers [130], and are more susceptible to be laden with dust and other particles. Its sturdiness makes it specially suitable for remote experiments or experiments in isolated locations, where replacing a malfunctioning sensor would be very expensive or inconvenient. One example could be space itself: Lately, there has been a rising interest in anemometry in Mars [131] [132], where conventional hot-wires have been discarded as a possibility due to size or frequency limitations (as conventional sturdy wires are rather slow). While the CNF here presented is likely to be too thin to properly operate in the rarefied atmosphere of Mars (as the mean free path is $\sim 10\lambda$ [133]) a slightly thicker wire (for example, 20μm) is likely to suffice, and in turn offer an even stronger wire. Statistics of extraterrestrial turbulence would not only allow us to possibly study larger Re than in our own atmosphere, but also to better understand some atmospheric phenomena on Earth [134].

4.2 Lagrangian Particle Tracking on Variable Density Wind Tunnel

In Chapter 3, the work done on the LPT setup located at the VDTT, as well as the velocity statistics obtained from Lagrangrian tracks measured at 6 bar and varying turbulence is shown. The setup was improved from its previous iteration, and its current capabilities have been characterized. The illumination system was modified in order for the system to be able to use

$d_p = 12\mu$m tracer particles. This allows to reduce the particle diameter by a factor of two, bringing it close to the smallest Kolmogorov length of $\sim 10\mu$m found in the experiment [93].

With this value, the particle material density was estimated from measurements performed with an aerodynamic particle sizer. A density of $\rho = 730 \pm 250\text{kgm}^3$ was calculated, which is lower than the density of cellulose. This points to the existance of several voids on each particle. Despite the large uncertainty in the density measurement, the Stokes number estimate was improved from the previous iteration. A further improvement to the density estimation could be achieved by carefully measuring the settling velocity of a single particle. A setup capable of achieving this currently exists within the institute [135], although it would require some modifications to its illumination system in order to be able to properly observe the small sized particles.

The particle size could be further reduced if, for example, KOBO USF particles are used. These particles have a nominal diameter of $d = 4\mu$m. This would imply that the Stokes number with this experiment would be a factor of 9 smaller than the $d = 12\mu$m particles used for this thesis. The image size would not change, as the current size is limited by diffraction. A concern, however, would be the required light intensity. The current setup provides just enough illumination to be able to distinguish between the current particles and the various spurious noise sources. By reducing the particle size by a factor of 3, the light intensity should be at least 9 times higher to compensate, as the scattered light scales with the surface of the particle. The current setup would require either a different laser to be installed or a beam focusing system inside the VDTT that is shielded from the turbulent flow and allows external focusing, as both the shape of the tunnel and the refractive index of SF_6 change with the working pressure. Without exchanging the cameras for a different set with a wider field of view that preserves both its sensor size and frequency, Lagrangian velocity statistics remain limited. To the best of the author's knowledge, such cameras are not available.

An alternative to overcome this technological challenge is to install the current camera setup on a sled able to move at the mean speed of the flow. This would allow to follow a particle for a longer duration than the field of view of a stationary camera setup normally permits. This setup poses its own set of challenges, as the acceleration and vibrations of the sled will manifest as strong positional noise in the tracks, which will need to be removed. Also, this method would not increase the lateral field of view, which would remain at ~ 20mm.

A particle disperser was added to automate the particle injection process, which allows for a more consistent number of particles per frame as well as a larger supply of particles per experiment. As seen from the microscope observations, the radial distribution function, the particle pair longitudinal relative acceleration and the relative angle between the acceleration of two particles, the particle disperser successfully produces a cloud of particles with no apparent electrostatic charge. Only a minimal amount of particle pairs could be detected.

If the track of one particle can be determined by two sets of two cameras each, it would not only allow to better find the real position of the particles, but also to characterize the noise of the system in order to remove it [136]. This would greatly improve the accuracy of the tracking code, thus allowing to obtain low noise velocity and acceleration statistics.

The Eulerian second order longitudinal structure function was calculated for four different grid protocols, which produce flows with Re_λ ranging from $Re_\lambda \approx 1300$ to $\mathrm{Re}_\lambda \approx 2700$. The resulting function showed good agreement with K41 theory down to $r_c \approx 9\eta$ in most cases. From the valid inertial range $r > r_c$, the energy dissipation rate ϵ was calculated. The values obtained were systematically lower when compared to hot-wire data measurements in the same conditions, and the fraction $\frac{\epsilon_{LPT}}{\epsilon_{HW}}$ between them ranged from 0.78 to 0.73, decreasing for increasing turbulence. The cause for these phenomena is not yet clear. Twice the transverse structure function $S_{2,\perp}$ was calculated from the data and compared to the predicted relation to the longitudinal structure function given by $S_{2,LPT} = \frac{3}{8} S_{2,\perp}$ (for an isotropic flow). An average difference of less than 6% was found for $r > 10^{-3}$. The larger difference at lower values is likely to be related to the same phenomenon that distorts the statistics for $r < r_c$, as the turbulence is expected to be more isotropic at smaller distances.

Bibliography

[1] E. Bodenschatz et al. "Variable density turbulence tunnel facility". In: *Review of Scientific Instruments* 85.93908 (2014). URL: https://doi.org/10.1007/s00348-019-2698-1.

[2] Christian Kuechler. "Measurements of Turbulence at High Reynolds Numbers". PhD thesis. Goettingen, Germany: Georg August University Goettingen, Oct. 2020.

[3] Arkady Tsinober. *An informal Introduction to Turbulence*. Springer, Dordrecht, 2004, p. xiii. ISBN: 9783540251415. DOI: https://doi.org/10.1007/0-306-48384-X.

[4] Osborne Reynolds. "An experimental investigation of the circumstances which determine whether the motion of water shall be direct or sinuous, and of the law of resistance in parallel channels". In: 35 (1883), pp. 84–99. DOI: 10.1098/rspl.1883.0018.

[5] D. Bluestein and S. Einav. "Transition to Turbulence in Pulsatile Flow Through Heart Valves—A Modified Stability Approach". In: *Journal of Biomechanical Engineering* 116.4 (Nov. 1994), pp. 477–487. ISSN: 0148-0731. DOI: 10.1115/1.2895799.

[6] N. Peters. "Multiscale combustion and turbulence". In: *Proceedings of the Combustion Institute* 32.1 (2009), pp. 1–25. ISSN: 1540-7489. DOI: https://doi.org/10.1016/j.proci.2008.07.044.

[7] Matthew J. Churchfield et al. "A numerical study of the effects of atmospheric and wake turbulence on wind turbine dynamics". In: *Journal of Turbulence* 13 (2012), N14. DOI: 10.1080/14685248.2012.668191.

[8] William David Lubitz. "Impact of ambient turbulence on performance of a small wind turbine". In: *Renewable Energy* 61 (2014). World Renewable Energy Congress – Sweden, 8–13 May, 2011, Linköping, Sweden, pp. 69–73. ISSN: 0960-1481. DOI: https://doi.org/10.1016/j.renene.2012.08.015.

[9] Sten Frandsen. *Turbulence and turbulence-generated structural loading in wind turbine clusters*. 2007.

[10] E. Bodenschatz et al. "Can We Understand Clouds Without Turbulence?" In: *Science* 327.5968 (2010), pp. 970–971. DOI: 10.1126/science.1185138.

[11] A. Peña. "Østerild: A natural laboratory for atmospheric turbulence". In: *Journal of Renewable and Sustainable Energy* 11.6 (2019), p. 063302. DOI: 10.1063/1.5121486.

[12] S. Risius et al. "Schneefernerhaus as a mountain research station for clouds and turbulence". In: *Atmospheric Measurement Techniques* 8.8 (2015), pp. 3209–3218. DOI: 10.5194/amt-8-3209-2015.

[13] Marcel Schröder et al. "Airborne Atmospheric Measurements with the Max Planck CloudKites". In: *EGU General Assembly Conference Abstracts*. EGU General Assembly Conference Abstracts. 2021, EGU21–11608.

[14] B. Stevens et al. "EUREC^{4}A". In: *Earth System Science Data* 13.8 (2021), pp. 4067–4119. DOI: 10.5194/essd-13-4067-2021.

[15] H. Nfaoui. "2.04 - Wind Energy Potential". In: *Comprehensive Renewable Energy*. Ed. by Ali Sayigh. Oxford: Elsevier, 2012, pp. 73–92. ISBN: 978-0-08-087873-7. DOI: https://doi.org/10.1016/B978-0-08-087872-0.00204-3.

[16] M. Vallikivi et al. "Turbulence measurements in pipe flow using a nano-scale thermal anemometry probe". In: *Experiments in Fluids* 51.6 (2011), pp. 1521–1527. DOI: 10.1007/s00348-011-1165-4.

[17] M. Bourgoin et al. "Investigation of the small-scale statistics of turbulence in the Modane S1MA wind tunnel". In: *CEAS Aeronautical Journal* 9.2 (2018), pp. 269–281. DOI: 10.1007/s13272-017-0254-3.

[18] Geoffrey Ingram Taylor. "Statistical theory of turbulence". In: 151 (873 1935). DOI: 10.1098/rspa.1935.0159.

[19] Brindesh R. Dhruva. "An experimental study of high Reynolds number turbulence in the atmosphere". English. Copyright - Database copyright ProQuest LLC; ProQuest does not claim copyright in the individual underlying works; Last updated - 2021-09-28. PhD thesis. 2000, p. 214. ISBN: 978-0-599-79082-7. URL: https://www.proquest.com/dissertations-theses/experimental-study-high-reynolds-number/docview/304640398/se-2?accountid=104741.

[20] Kartik P. Iyer, Katepalli R. Sreenivasan, and P. K. Yeung. "Reynolds number scaling of velocity increments in isotropic turbulence". In: *Phys. Rev. E* 95 (2 2017), p. 021101. DOI: 10.1103/PhysRevE.95.021101.

[21] P. K. Yeung, K. R. Sreenivasan, and S. B. Pope. "Effects of finite spatial and temporal resolution in direct numerical simulations of incompressible isotropic turbulence". In: *Phys. Rev. Fluids* 3 (6 2018), p. 064603. DOI: 10.1103/PhysRevFluids.3.064603.

[22] Javier Jimenez. "Computing high-Reynolds-number turbulence: will simulations ever replace experiments?" In: 4 (2003). DOI: 10.1088/1468-5248/4/1/022.

[23] CHRISTOPHER M. WHITE, ADONIOS N. KARPETIS, and KATEPALLI R. SREENIVASAN. "High-Reynolds-number turbulence in small apparatus: grid turbulence in cryogenic liquids". In: *Journal of Fluid Mechanics* 452 (2002), 189–197. DOI: 10.1017/S0022112001007194.

[24] B. Rousset et al. "Superfluid high REynolds von Kármán experiment". In: *Review of Scientific Instruments* 85.10 (2014), p. 103908. DOI: 10.1063/1.4897542.

[25] S. Pietropinto et al. "Superconducting instrumentation for high Reynolds turbulence experiments with low temperature gaseous helium". In: *Physica C: Superconductivity* 386 (2003), pp. 512–516. ISSN: 0921-4534. DOI: https://doi.org/10.1016/S0921-4534(02)02115-9.

[26] J. Salort, A. Monfardini, and P.-E. Roche. "Cantilever anemometer based on a superconducting micro-resonator: Application to superfluid turbulence". In: *Review of Scientific Instruments* 83.12 (2012), p. 125002. DOI: 10.1063/1.4770119.

[27] Stephen B. Pope. *Turbulent Flows*. Cambridge University Press, 2000. DOI: 10.1017/CBO9780511840531.

[28] M Hamdi et al. "Comparison of different tracers for PIV measurements in EHD airflow". In: *Experiments in fluids* 55.4 (2014), pp. 1–12.

[29] Lewis Fry Richardson. *Weather prediction by numerical process*. Cambridge university press, 2007.

[30] Andrej Nikolaevich Kolmogorov. "Dissipation of energy in isotropic turbulence". In: *Dokl. Akad. Nauk SSSR*. Vol. 32. 1941, pp. 325–327.

[31] Katepalli R. Sreenivasan. "An update on the energy dissipation rate in isotropic turbulence". In: *Physics of Fluids* 10.2 (1998), pp. 528–529. DOI: 10.1063/1.869575.

[32] Katepalli R. Sreenivasan. "On the universality of the Kolmogorov constant". In: *Physics of Fluids* 7.11 (1995), pp. 2778–2784. DOI: 10.1063/1.868656.

[33] Andreĭ Sergeevich Monin and Akiva M Yaglom. *Statistical fluid mechanics, volume II: mechanics of turbulence*. Vol. 2. Courier Corporation, 2013.

[34] George Keith Batchelor and Albert Alan Townsend. "The nature of turbulent motion at large wave-numbers". In: *Proceedings of the Royal Society of London. Series A. Mathematical and Physical Sciences* 199.1057 (1949), pp. 238–255.

[35] H. Kahalerras et al. "Intermittency and Reynolds number". In: *Physics of Fluids* 10.4 (1998), pp. 910–921. DOI: 10.1063/1.869613.

[36] ANDREAS MUSCHINSKI, ROD G. FREHLICH, and BEN B. BALSLEY. "Small-scale and large-scale intermittency in the nocturnal boundary layer and the residual layer". In: *Journal of Fluid Mechanics* 515 (2004), 319–351. DOI: 10.1017/S0022112004000412.

[37] M. Krstić. "Chapter 9 - MIXING CONTROL FOR JET FLOWS". In: *Combustion Processes in Propulsion*. Ed. by Gabriel D. Roy. Burlington: Butterworth-Heinemann, 2006, pp. 87–96. ISBN: 978-0-12-369394-5. DOI: https://doi.org/10.1016/B978-012369394-5/50013-5.

[38] Kyle D Squires and John K Eaton. "Preferential concentration of particles by turbulence". In: *Physics of Fluids A: Fluid Dynamics* 3.5 (1991), pp. 1169–1178.

[39] Lian-Ping Wang and Martin R. Maxey. "Settling velocity and concentration distribution of heavy particles in homogeneous isotropic turbulence". In: *Journal of Fluid Mechanics* 256 (1993), 27–68. DOI: 10.1017/S0022112093002708.

[40] D. C. Collis and M. J. Williams. "Two-dimensional convection from heated wires at low Reynolds numbers". In: *Journal of Fluid Mechanics* 6.3 (1959), 357–384. DOI: 10.1017/S0022112059000696.

[41] H. Kramers. "Heat transfer from spheres to flowing media". In: *Physica* 12.2 (1946), pp. 61–80. ISSN: 0031-8914. DOI: https://doi.org/10.1016/S0031-8914(46)80024-7.

[42] Loius Vessot King. "XII. On the convection of heat from small cylinders in a stream of fluid: Determination of the convection constants of small platinum wires with applications to hot-wire anemometry". In: *Royal Society* 214 (509-522 1914). ISSN: 0264-3952. DOI: 10.1098/rsta.1914.0023.

[43] B Gebhart et al. "Buoyancy-induced flows and transport". In: (1988).

[44] A. E. Perry, A. J. Smits, and M. S. Chong. "The effects of certain low frequency phenomena on the calibration of hot wires". In: *Journal of Fluid Mechanics* 90.3 (1979), 415–431. DOI: 10.1017/S0022112079002329.

[45] M. Samie, N. Hutchins, and I. Marusic. "Revisiting end conduction effects in constant temperature hot-wire anemometry". In: *Experiments in Fluids* 59.9 (2018), p. 133. DOI: 10.1007/s00348-018-2587-z.

[46] P. M. Ligrani and P Bradshaw. "Spatial resolution and measurement of turbulence in the viscous sublayer using subminiature hot-wire probes". In: *Experiments in Fluids* 5.6 (1987), 407—417. DOI: 10.1007/BF00264405.

[47] J D Li et al. "The response of hot wires in high Reynolds-number turbulent pipe flow". In: 15.5 (2004), pp. 789–798. DOI: 10.1088/0957-0233/15/5/003.

[48] Marcus Hultmark, Anand Ashok, and Alexander J Smits. "A new criterion for end-conduction effects in hot-wire anemometry". In: 22.5 (2011), p. 055401. DOI: 10.1088/0957-0233/22/5/055401.

[49] J D Li. "Dynamic response of constant temperature hot-wire system in turbulence velocity measurements". In: 15.9 (2004), pp. 1835–1847. DOI: 10.1088/0957-0233/15/9/022.

[50] D. Bestion, J. Gaviglio, and J. P. Bonnet. "Comparison between constant-current and constant-temperature hot-wire anemometers in high-speed flows". In: *Review of Scientific Instruments* 54.11 (1983), pp. 1513–1524. DOI: 10.1063/1.1137279.

[51] N. Hutchins et al. "A direct measure of the frequency response of hot-wire anemometers: temporal resolution issues in wall-bounded turbulence". In: *Experiments in Fluids* 56.1 (2015), p. 18. DOI: 10.1007/s00348-014-1856-8.

[52] J. Weiss, H. Knauss, and S. Wagner. "Method for the determination of frequency response and signal to noise ratio for constant-temperature hot-wire anemometers". In: *Review of Scientific Instruments* 72.3 (2001), pp. 1904–1909. DOI: 10.1063/1.1347970.

[53] P Freymuth. "Frequency response and electronic testing for constant-temperature hot-wire anemometers". In: 10.7 (1977), pp. 705–710. DOI: 10.1088/0022-3735/10/7/012.

[54] J. P. Bonnet and T. Alziary de Roquefort. "Determination and optimization of frequency response of constant temperature hot-wire anemometers in supersonic flows". In: *Review of Scientific Instruments* 51.2 (1980), pp. 234–239. DOI: 10.1063/1.1136180.

[55] A J Smits, A E Perry, and P H Hoffmann. "The response to temperature fluctuations of a constant-current hot-wire anemometer". In: 11.9 (1978), pp. 909–914. DOI: 10.1088/0022-3735/11/9/012.

[56] R S Azad. In: 4.3 (1993), pp. 405–410. DOI: 10.1088/0957-0233/4/3/023.

[57] S.B. Lyon. "3.16 - Corrosion of Tungsten and its Alloys". In: *Shreir's Corrosion*. Ed. by Bob Cottis et al. Oxford: Elsevier, 2010, pp. 2151–2156. ISBN: 978-0-444-52787-5. DOI: https://doi.org/10.1016/B978-044452787-5.00105-0. URL: https://www.sciencedirect.com/science/article/pii/B9780444527875001050.

[58] Reinaldo A. Gomes and Reinhard Niehuis. "Development of a novel anemometry technique for velocity and temperature measurement". In: *Experiments in Fluids* 59.9 (2018), p. 142. DOI: 10.1007/s00348-018-2595-z.

[59] P. Avouris et al. "Carbon nanotube electronics". In: *Proceedings of the IEEE* 91.11 (2003), pp. 1772–1784. DOI: 10.1109/JPROC.2003.818338.

[60] B.G Demczyk et al. "Direct mechanical measurement of the tensile strength and elastic modulus of multiwalled carbon nanotubes". In: *Materials Science and Engineering: A* 334.1 (2002), pp. 173–178. ISSN: 0921-5093. DOI: https://doi.org/10.1016/S0921-5093(01)01807-X.

[61] Erik Lassner and Schubert Wolf-Dieter. *Tungsten Properties, Chemistry, Technology of the Element, Alloys, and Chemical Compounds*. Springer US, 1999, p. 27. ISBN: 978-1-4613-7225-7. DOI: 10.1007/978-1-4615-4907-9.

[62] Jing Kong et al. "Synthesis of individual single-walled carbon nanotubes on patterned silicon wafers". In: *Nature* 395.6705 (1998), pp. 878–881. DOI: 10.1038/27632.

[63] ObasogieOyema E. et al. In: *Carbon letters* 28 (2018), pp. 72–80.

[64] Natnael Behabtu et al. “Strong, Light, Multifunctional Fibers of Carbon Nanotubes with Ultrahigh Conductivity”. In: *Science* 339.6116 (2013), pp. 182–186. DOI: 10.1126/science.1228061.

[65] Natnael Behabtu et al. “Strong, Light, Multifunctional Fibers of Carbon Nanotubes with Ultrahigh Conductivity”. In: *Science* 339.6116 (2013), pp. 182–186. DOI: 10.1126/science.1228061.

[66] P. D. Desai et al. “Electrical Resistivity of Selected Elements”. In: *Journal of Physical and Chemical Reference Data* 13.4 (1984), pp. 1069–1096. DOI: 10.1063/1.555723.

[67] Paul A. Tipler. *Physics for Scientists and Engineers*. W. H. Freeman, 1999. ISBN: 071673821X, 9780716738213.

[68] Lin Hu, Brian D. Wirth, and Dimitrios Maroudas. “Thermal conductivity of tungsten: Effects of plasma-related structural defects from molecular-dynamics simulations”. In: *Applied Physics Letters* 111.8 (2017), p. 081902. DOI: 10.1063/1.4986956.

[69] Engineering ToolBox. *Resistivity and Conductivity - Temperature Coefficients for Common Materials*. https://www.engineeringtoolbox.com/resistivity-conductivity-d_418.html. Accessed: 2021-11-08. 2003.

[70] John R. Rumble. *CRC Handbook of Chemistry and Physics, 102nd Edition (Internet Version 2021)*. Accessed: 2021-11-08. 2021.

[71] L. A. Cornish et al. “The Platinum Development Initiative: Platinum-Based Alloys for High Temperature and Special Applications: Part III”. In: *Platinum Metals Review* 53.3 (2009), pp. 155–163. ISSN: 0032-1400. DOI: doi:10.1595/147106709X464371.

[72] DexMat incorporated. *Supplied by manufacturer*. dexmat.com. Accessed: 2021-10-06. 2020.

[73] Eric Mayhew and Vikas Prakash. “Thermal conductivity of high performance carbon nanotube yarn-like fibers”. In: *Journal of Applied Physics* 115.17 (2014), p. 174306. DOI: 10.1063/1.4874737.

[74] Qin-Yi Li et al. “Measurement of specific heat and thermal conductivity of supported and suspended graphene by a comprehensive Raman optothermal method”. In: *Nanoscale* 9 (30 2017), pp. 10784–10793. DOI: 10.1039/C7NR01695F. URL: http://dx.doi.org/10.1039/C7NR01695F.

[75] J. Boylan. Vol. 4. Institute of Materials, Mineral & Mining, 1994, pp. 707–708.

[76] Jian-Jun Sun et al. "Heated graphite cylinder electrodes". In: *Electrochemistry Communications* 9.2 (2007), pp. 283–288. ISSN: 1388-2481. DOI: https://doi.org/10.1016/j.elecom.2006.09.018.

[77] Andrea G. Chiariello, Giovanni Miano, and Antonio Maffucci. "Size and temperature effects on the resistance of copper and carbon nanotubes nano-interconnects". In: *19th Topical Meeting on Electrical Performance of Electronic Packaging and Systems*. 2010, pp. 97–100. DOI: 10.1109/EPEPS.2010.5642555.

[78] J. Hone et al. "Thermal properties of carbon nanotubes and nanotube-based materials". In: *Applied Physics A* 74.3 (2002), pp. 339–343. DOI: 10.1007/s003390201277.

[79] W. Yi et al. "Linear specific heat of carbon nanotubes". In: *Phys. Rev. B* 59 (14 1999), R9015–R9018. DOI: 10.1103/PhysRevB.59.R9015.

[80] Ch. Laurent, E. Flahaut, and A. Peigney. "The weight and density of carbon nanotubes versus the number of walls and diameter". In: *Carbon* 48.10 (2010), pp. 2994–2996. ISSN: 0008-6223. DOI: https://doi.org/10.1016/j.carbon.2010.04.010. URL: https://www.sciencedirect.com/science/article/pii/S0008622310002617.

[81] T. W. Ebbesen et al. "Electrical conductivity of individual carbon nanotubes". In: *Nature* 382.6586 (1996), pp. 54–56. DOI: 10.1038/382054a0.

[82] Da Jiang Yang et al. "Thermal conductivity of multiwalled carbon nanotubes". In: *Phys. Rev. B* 66 (16 2002), p. 165440. DOI: 10.1103/PhysRevB.66.165440. URL: https://link.aps.org/doi/10.1103/PhysRevB.66.165440.

[83] Jennifer R. Lukes and Hongliang Zhong. "Thermal Conductivity of Individual Single-Wall Carbon Nanotubes". In: *Journal of Heat Transfer* 129.6 (Sept. 2006), pp. 705–716. ISSN: 0022-1481. DOI: 10.1115/1.2717242.

[84] James M Gere and Barry J Goodno. *Mechanics of materials*. Cengage learning, 2012.

[85] Ankit Rohatgi. *WebPlotDigitizer*. Version 4.3, accessed 22/11/21. 2020. URL: https://automeris.io/WebPlotDigitizer.

[86] K M Talluru et al. "A calibration technique to correct sensor drift issues in hot-wire anemometry". In: 25.10 (2014), p. 105304. DOI: 10.1088/0957-0233/25/10/105304.

[87] Eberhard Bodenschatz and Michael Eckert. "Prandtl and the Göttingen school". In: *A Voyage Through Turbulence*. Ed. by Peter A. Davidson et al. Cambridge University Press, 2011, 40–100. DOI: 10.1017/CBO9781139018241.003.

[88] Giuseppe Gabriele Nunnari. "Experimental investigation of a sheared thermally unstable boundary layer". PhD thesis. Goettingen, Germany: Georg August University Goettingen, 2021.

[89] Muhammet Ozdogan et al. "Comparative study of turbulent flow around a bluff body by using two-and three-dimensional CFD". In: *Wind and Structures* 25.6 (2017), pp. 537–549.

[90] CE McDonald. "Chlorosulfuric Acid". In: *Kirk-Othmer Encyclopedia of Chemical Technology* (2000).

[91] Michele Guala, M Metzger, and Beverley J McKeon. "Interactions within the turbulent boundary layer at high Reynolds number". In: *Journal of Fluid Mechanics* 666 (2011), pp. 573–604.

[92] KY Huang et al. "Investigation of the atmospheric surface layer using a novel high-resolution sensor array". In: *Experiments in Fluids* 62.4 (2021), pp. 1–13.

[93] C. Kuechler, G. Bewley, and E. Bodenschatz. "Experimental Study of the Bottleneck in Fully Developed Turbulence". In: *Journal of Statistical Physics* 175.3 (2019), pp. 617–639. URL: https://doi.org/10.1007/s10955-019-02251-1.

[94] Yi-Chun Huang. "Experimental Methods for Understanding Turbulence in the Lower Atmosphere". PhD thesis. Princeton University, 2021.

[95] HH Bruun. "Interpretation of a hot wire signal using a universal calibration law". In: *Journal of Physics E: Scientific Instruments* 4.3 (1971), p. 225.

[96] K.P. Griffin, N.J Wei, and E. Bodenschatz. "Control of long-range correlations in turbulence". In: *Experiments in Fluids* 60.4 (2019), p. 55. URL: https://doi.org/10.1007/s00348-019-2698-1.

[97] Augustinus Bertens. personal communication.

[98] Michael E. Thomas and Tristan J. Tayag. "Refractive index of He, SF6, and CO2 at 0.63299 μm as a function of temperature and pressure". In: *Appl. Opt.* 27.16 (Aug. 1988), pp. 3317–3318. DOI: 10.1364/AO.27.003317.

[99] Daniel Schanz, Sebastian Gesemann, and Andreas Schröder. "Shake-The-Box: Lagrangian particle tracking at high particle image densities". In: 57.5 (2016), p. 70. DOI: 10.1007/s00348-016-2157-1.

[100] Moo K. Chung. *Gaussian kernel smoothing*. 2021. arXiv: 2007.09539 [stat.ME].

[101] N. Mordant, A.M. Crawford, and E. Bodenschatz. "Experimental Lagrangian acceleration probability density function measurement". In: *Physica D: Nonlinear Phenomena* 193.1 (2004), pp. 245–251. DOI: https://doi.org/10.1016/j.physd.2004.01.041.

[102] Paul H. C. Eilers and Brian D. Marx. "Flexible Smoothing with *B*-splines and Penalties". In: *Statistical Science* 11.2 (1996), pp. 89–102. ISSN: 08834237. URL: http://www.jstor.org/stable/2246049.

[103] Paul Eilers, Brian Marx, and María Durbán. "Twenty years of P-splines". In: *SORT (Statistics and Operations Research Transactions)* 39 (Jan. 2015), pp. 149–186.

[104] Sebastian Gesemann. *From Particle Tracks to Velocity and Acceleration Fields Using B-Splines and Penalties*. 2015. arXiv: 1510.09034 [physics.flu-dyn].

[105] Paul H. C. Eilers and Brian D. Marx. "Splines, knots, and penalties". In: *WIREs Computational Statistics* 2.6 (2010), pp. 637–653. DOI: https://doi.org/10.1002/wics.125.

[106] Federico Toschi and Eberhard Bodenschatz. "Lagrangian properties of particles in turbulence". In: *Annual review of fluid mechanics* 41 (2009), pp. 375–404.

[107] Greg Anthony Voth. *Lagrangian acceleration measurements in turbulence at large Reynolds numbers*. Cornell University, 2000.

[108] MR Maxey. "The velocity skewness measured in grid turbulence". In: *The Physics of fluids* 30.4 (1987), pp. 935–938.

[109] Jiang Lu, Freja Nordsiek, and Raymond A. Shaw. "Clustering of settling charged particles in turbulence: theory and experiments". In: *New Journal of Physics* 12.12, 123030 (Dec. 2010), p. 123030. DOI: 10.1088/1367-2630/12/12/123030.

[110] Ewe Wei Saw. *Studies of spatial clustering of inertial particles in turbulence*. 2008. DOI: 10.37099/mtu.dc.etds/118.

[111] JUAN P. L. C. SALAZAR et al. "Experimental and numerical investigation of inertial particle clustering in isotropic turbulence". In: *Journal of Fluid Mechanics* 600 (2008), 245–256. DOI: 10.1017/S0022112008000372.

[112] Jiang Lu and Raymond A. Shaw. "Charged particle dynamics in turbulence: Theory and direct numerical simulations". In: *Physics of Fluids* 27.6 (2015), p. 065111. DOI: 10.1063/1.4922645.

[113] Z. Warhaft and X. Shen. "On the higher order mixed structure functions in laboratory shear flow". In: *Physics of Fluids* 14.7 (2002), pp. 2432–2438. DOI: 10.1063/1.1478561.

[114] *PubChem Compound Summary for CID 16211032*. Retrieved November 28. 2021. URL: https://pubchem.ncbi.nlm.nih.gov/compound/Deae-cellulose..

[115] P. K. Yeung and S. B. Pope. "Lagrangian statistics from direct numerical simulations of isotropic turbulence". In: *Journal of Fluid Mechanics* 207 (1989), 531–586. DOI: 10.1017/S0022112089002697.

[116] Greg A. Voth, K. Satyanarayan, and Eberhard Bodenschatz. "Lagrangian acceleration measurements at large Reynolds numbers". In: *Physics of Fluids* 10.9 (1998), pp. 2268–2280. DOI: 10.1063/1.869748.

[117] Bianca Viggiano et al. "Lagrangian diffusion properties of a free shear turbulent jet". In: *Journal of Fluid Mechanics* 918 (2021), A25. DOI: 10.1017/jfm.2021.325.

[118] X. Shen and Z. Warhaft. "The anisotropy of the small scale structure in high Reynolds number (R$\lambda \sim 1000$) turbulent shear flow". In: *Physics of Fluids* 12.11 (2000), pp. 2976–2989. DOI: 10.1063/1.1313552.

[119] Wenhai Sun, Ning Huang, and Wei He. "Turbulence burst over four micro-topographies in the wind tunnel". In: *CATENA* 148 (2017). Achieving sustainability through conservation in a changing world, pp. 138–144. ISSN: 0341-8162. DOI: https://doi.org/10.1016/j.catena.2016.04.017.

[120] G-J Van Zadelhoff et al. "Retrieving hurricane wind speeds using cross-polarization C-band measurements". In: *Atmospheric Measurement Techniques* 7.2 (2014), pp. 437–449.

[121] L Di Mare, TO Jelly, and IJ Day. "Angular response of hot wire probes". In: *Measurement Science and Technology* 28.3 (2017), p. 035303.

[122] Ouassim Ghodbane, Lionel Roué, and Daniel Bélanger. "Copper electrodeposition on pyrolytic graphite electrodes: Effect of the copper salt on the electrodeposition process". In: *Electrochimica Acta* 52.19 (2007), pp. 5843–5855. ISSN: 0013-4686. DOI: https://doi.org/10.1016/j.electacta.2007.03.009.

[123] Susumu Arai, Morinobu Endo, and Norio Kaneko. "Ni-deposited multi-walled carbon nanotubes by electrodeposition". In: *Carbon* 42.3 (2004), pp. 641–644. ISSN: 0008-6223. DOI: https://doi.org/10.1016/j.carbon.2003.12.084. URL: https://www.sciencedirect.com/science/article/pii/S0008622304000053.

[124] Selcuk Harput. "Fields of application of nickel-plated copper conductor". In: *Wire journal international* 39.12 (2006), pp. 65–68.

[125] Guang Zeng, Stuart McDonald, and Kazuhiro Nogita. "Development of high-temperature solders: Review". In: *Microelectronics Reliability* 52.7 (2012), pp. 1306–1322. DOI: https://doi.org/10.1016/j.microrel.2012.02.018.

[126] Yu. Plevachuk et al. "Experimental study of density, surface tension, and contact angle of Sn–Sb-based alloys for high temperature soldering". In: *Journal of Materials Science* 45.8 (2010), pp. 2051–2056. DOI: 10.1007/s10853-009-4120-5.

[127] OSI Fayomi, IG Akande, and AA Sode. "Corrosion Prevention of Metals via Electroless Nickel Coating: A review". In: *Journal of Physics: Conference Series*. Vol. 1378. 2. IOP Publishing. 2019, p. 022063.

[128] Dheerendra Kumar Dwivedi. *Fundamentals of Metal Joining*. Springer.

[129] C. Dames et al. "A hot-wire probe for thermal measurements of nanowires and nanotubes inside a transmission electron microscope". In: *Review of Scientific Instruments* 78.10 (2007), p. 104903. DOI: 10.1063/1.2785848.

[130] XiaoJing Zheng et al. "Investigation on very large scale motions (VLSMs) and their influence in a dust storm". In: *Science China Physics, Mechanics and Astronomy* 56.2 (2013), pp. 306–314.

[131] Don Banfield and Richard Dissly. "A Martian sonic anemometer". In: *2005 IEEE aerospace conference*. IEEE. 2005, pp. 641–647.

[132] Lukasz Kowalski. "Contribution to advanced hot wire wind sensing". In: (2016).

[133] Norbert Schörghofer. "Subsurface air flow on Mars". In: *Nature Physics* 10.1 (2014), pp. 14–15.

[134] James D Iversen, R Greeley, and James B Pollack. “Windblown dust on earth, Mars and Venus”. In: *Journal of the Atmospheric Sciences* 33.12 (1976), pp. 2425–2429.

[135] Johannes Milan Guettler. “Experimental Investigation of Micrometric Droplets and Artificial Particles”. PhD thesis. Goettingen, Germany: Georg August University Goettingen, 2021.

[136] John M Lawson et al. “Bias in particle tracking acceleration measurement”. In: *Experiments in Fluids* 59.11 (2018), pp. 1–14.

Acknowledgements

This work, has been made possible only thanks to the support of my superiors, colleagues, friends and family.
My thesis work was supervised by Prof. Eberhard Bodenschatz. I thank him for giving me the opportunity to work at the MPI and his dedicated support even before I arrived in Germany. The independence he gave me was a new and challenging scenario that gave me the opportunity to grow into and develop. I also thank him for his endless patience and understanding with the many mishaps that occurred during these four years.

Prof. Konrad Samwer and Prof. Andreas Janshoff were being part of my thesis committee, and gave useful insights and observations (scientific and otherwise) during our meetings. The suggestions and contacts they provided for experimental work proved instrumental for the development of my thesis.

I thank Prof. Dillman for agreeing to be the co-referee of my thesis in such a short notice, as well as Prof. Parlitz and Prof. Klump for being part of thesis examination board.

Dr. Christian Kuechler developed and implemented the first iteration of the Lagrangian Particle Tracking setup. He also got me up to date on the status of said experiment, as well as taking the time to share the knowledge he accrued regarding both hot-wires and the VDTT. I wholeheartedly thank him for the patience and constant scientific support during the development of the third chapter of my thesis, and the many corrections to the complete manuscript. Your open and calm demeanor when discussing and ironing out the various details on my thesis was truly motivating. Without your help, it is unlikely that this thesis would have come to fruition.

Dr Jan Molacek has been constantly improving the code used for the Lagrangian Particle Tracking setup, and being very willing to discuss and implement suggestions our team had regarding the workings of the code, as well as taking the time to slowly explain some of the intricacies of the code used.

Dr Oliver Schlenczek and Dr Gholamhossein Bagheri provided their help during the measurement of the density of the particles. They lent me their

particle sizing equipment, even at the moment when it was under heavy use. Dr Freja Nordsiek gave me her insights regarding radial distribution functions, charged particles, hot wires and a variety of topics that served as an inspiration for the design of the experiments.

Guus Bertens helped me to set up several experiments performed during the development of this thesis. Your honest (if a bit blunt) opinions were often welcome and always helpful.

Andreas Renner, Arthur Kubiczek, Andreas Kopp and Marcel Meyer, the technicians of the experimental hall were of huge help at various stages of my thesis. Be it construction or maintenance, their pooled knowledge about technical details of everything Experimental Hall related was invaluable to the development of this thesis.

Many thanks to Laura Diaz, Dr Holder Nobach, Jens-Peter Kroll and the electronics workshop team for their useful comments and willingness to help me design and create some of the circuitry I required during my thesis, as well as offering their technical support, knowledge and equipment regarding several instruments. Their soldering tips made the challenging task of soldering the carbon nanofiber a possibility, as well.

Thanks to Udo Schminke and the machine shop team for the quick manufacturing of several large pieces needed for the VDTT, as well as smaller, even clock-work like parts and modification for various hot-wire experiments. Despite the language barrier and my lack of knowledge regarding preparing schematics, everything was made exactly as I wanted it to be. I also thank Johannes Guettler for the early help with the 3D printer, as well as the many interesting scientific discussions, either at the office or during the many project conferences we had to attend.

Marcel Wedi and Marcel Schroeder proofread parts of my thesis.

This has been my first time so far away of my home country, and thus the emotional support and friendship of my close colleagues and friends has been invaluable. Many thanks (in no particular order!) to Baltasar, Johannes, Guus, Tefa, Jasmin, Rodrigo, Freja and my workplace colleagues for the many boardgame evenings, friendly talks, serious talks, chances to unwind and the help provided to navigate a foreign country without full mastery of the language.

Valentina has put up with me being on the other side of the world for two years, and eventually came all the way from the southern hemisphere to be here with me. I am extremely lucky to have you as my partner.

Finally, but no less important, thank to my parents and family. Coming

from a country where, unfortunately, dedicating oneself to science has very little future prospects, it would have been impossible to be here without their unwavering support.

Funding: This project has received funding from the Marie - Sklodowska Curie Actions (MSCA) under the European Union's Horizon 2020 research and innovation programme (grant agreement no. 675675).

Appendix A: Plasmonic and Semiconductor Nanoparticles Interfere with Stereolithographic 3D Printing

This chapter is a reprint of the paper "Plasmonic and Semiconductor Nanoparticles Interfere with Stereolithographic 3D Printing". which has been published in ACS Applied Matter and Interfaces. Reprinted with permission from [1]. Copyright 2021 American. Further permissions related to the material excerpted should be directed to the ACS.

The author of this thesis designed all 3D models used for this study, as well as performing the printing process of the test parts, and assessed the quality of the 3D printed parts by using a confocal laser microscope for visual inspection. The author also wrote one section of the manuscript (Printing with a Nanoscribe 3D Printer). The coauthors synthethized the nanoparticles used in this work, developed and realized the technique that permits the integration of the nanoparticles onto the printer's resin. They also performed all the characterization techniques described in the article, organized the research and wrote most of the manuscript.

[1]Rebecca Momper, Antonio Ibanez Landeta, Long Yang, Henry Halim, Heloise Therien-Aubin, Eberhard Bodenschatz, Katharina Landfester, and Andreas Riedinger ACS Applied Materials & Interfaces 2020 12 (45), 50834-50843 DOI: 10.1021/acsami.0c14546, URL: https://pubs.acs.org/doi/10.1021/acsami.0c14546

ACS APPLIED MATERIALS & INTERFACES

www.acsami.org

Research Article

Plasmonic and Semiconductor Nanoparticles Interfere with Stereolithographic 3D Printing

Rebecca Momper, Antonio Ibanez Landeta, Long Yang, Henry Halim, Heloise Therien-Aubin, Eberhard Bodenschatz, Katharina Landfester,* and Andreas Riedinger*

Cite This: *ACS Appl. Mater. Interfaces* 2020, 12, 50834−50843

Read Online

ACCESS | Metrics & More | Article Recommendations | Supporting Information

ABSTRACT: Two-photon polymerization stereolithographic three-dimensional (3D) printing is used for manufacturing a variety of structures ranging from microdevices to refractive optics. Incorporation of nanoparticles in 3D printing offers huge potential to create even more functional nanocomposite structures. However, this is difficult to achieve since the agglomeration of the nanoparticles can occur. Agglomeration not only leads to an uneven distribution of nanoparticles in the photoresin but also induces scattering of the excitation beam and altered absorption profiles due to interparticle coupling. Thus, it is crucial to ensure that the nanoparticles do not agglomerate during any stage of the process. To achieve noninteracting and well-dispersed nanoparticles on the 3D printing process, first, the stabilization of nanoparticles in the 3D printing resin is indispensable. We achieve this by functionalizing the nanoparticles with surface-bound ligands that are chemically similar to the photoresin that allows increased nanoparticle loadings without inducing agglomeration. By systematically studying the effect of different nanomaterials (Au nanoparticles, Ag nanoparticles, and CdSe/CdZnS nanoplatelets) in the resin on the 3D printing process, we observe that both, material-specific (absorption profiles) and unspecific (radical quenching at nanoparticle surfaces) pathways co-exist by which the photopolymerization procedure is altered. This can be exploited to increase the printing resolution leading to a reduction of the minimum feature size.

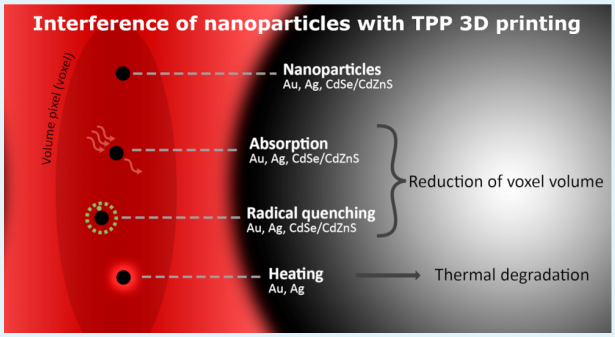

KEYWORDS: *3-D printing, stereolithography, plasmonic nanoparticles, semiconductor nanoparticles, radical quenching*

INTRODUCTION

Three-dimensional (3D) printing enables the quick production of complex geometries.[1] Among existing 3D printing techniques, two-photon polymerization (TPP, see Scheme S1) stereolithography stands out for producing a large variety of micro- and nanosized structures,[2] e.g., for photonics,[3] microoptics,[4] micromachines,[5] biomedicine,[6] or microfluidics[7] applications. Here a spatially controlled fs-pulsed long-wavelength (e.g., 780 nm) laser is used to cross-link a photoresin via two-photon absorption to build complex polymeric structures. Due to the nonlinearity of the two-photon absorption process for curing, the resolution is improved compared to ultraviolet (UV) curing.[8]

Commonly used purely organic photoresins for TPP mainly ensure the good structural integrity of the printed object but lack a more specific functionality, such as optical, electrical, or magnetic activity. To further expand the library of printable, functional materials and to access even more fields of applications, like micro- and nanomachines, and (opto)-electronics, the integration of different materials is a widely used method.[1,9] Depending on the properties of the filler material, properties like conductivity,[10] magnetism,[11] or piezoelectricity,[12] can be integrated. Especially, the combination of 3D printing and nanotechnology opens new ways toward materials with tunable properties and functionality. For example, Ceylan et al. constructed a polymeric microrobot loaded with iron oxide nanoparticles (NPs), which allow the magnetically driven motion of the swimmers due to the superparamagnetic behavior of the NPs.[11]

The integration of nanomaterials in a printable resin not only introduces functionality to the printed device but may also affect the printability and processability of the resin.[13] Especially the stereolithographic technique, which is based on optical excitations, can be strongly affected by nanomaterials since the integrated materials can interact with the light source by absorption or scattering. Jonusauskas et al. showed this in plasmon-assisted 3D microstructuring of gold-doped poly-

Received: August 12, 2020
Accepted: October 14, 2020
Published: October 28, 2020

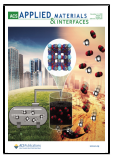

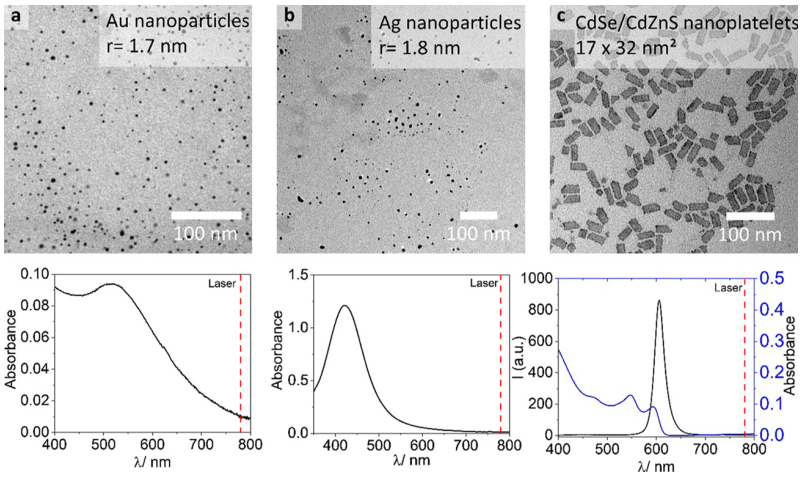

Figure 1. NPs used in this study in conjunction with a commercial acrylate-based resin for 3D printing NP/polymer composites. Upper row: transmission electron microscopy (TEM) micrographs of NPs, for higher magnification micrographs see Figure S17; lower row: corresponding absorption spectra and in case of CdSe/CdZnS NPLs the emission spectra. The dashed vertical line represents the pulsed laser wavelength at 780 nm for TPP; (a) Au NPs; (b) Ag NPs; and (c) CdSe/CdZnS NPLs.

mers.[14,15] The printed linewidth strongly depended on the concentration of Au NPs. Increasing the Au NP concentration increased the printed feature size, whereas for small concentrations the linewidth decreased. This observation led to the suggestion that Au NPs could replace the photoinitiator to some extent. The effect was explained by the plasmon effect of Au NPs.[16,17] Also, for CdSe quantum dots, an improvement of the resolution and simultaneously a reduction of monomer conversion was observed by Peng et al. upon the integration of quantum dots to a photocurable resin.[18] Liu et al. developed a method to produce 3D printed structures loaded with silver nanowires to realize electrical conductivity.[19] Again, a decrease of the linewidth was observed but not further analyzed.

In TPP 3D printing, plasmonic and semiconductor NPs can interact with the light excitation either via 1 photon absorption (1PA) or 2 photon absorption (2PA, see Scheme S1)[20−22] hindering the efficient formation of photogenerated radicals.[18] Furthermore, NPs can also quench the polymerization directly when radical species come in contact with their surface.[23−25] Both processes influence the TPP 3D printing process significantly. This is further complicated if NPs agglomerate in the photoresin. Especially, plasmonic NPs exhibit altered optical responses depending on their colloidal state, i.e., agglomeration-induced plasmonic coupling can shift the plasmon resonance substantially. The dispersion of NPs in the photoresin at high loadings without agglomeration is often a nontrivial and challenging task due to attractive forces between NPs that drive the agglomeration process. Notably, agglomeration can occur even before the printing process is started, e.g., when the NPs are introduced in the uncured photoresin.[26,27] As agglomeration can influence the properties of the NPs[26] (e.g., through plasmonic coupling), not only the final properties of the printed structures are affected but also interference with the printing process itself is expected. Therefore, especially agglomeration-induced scattering or absorption of the curing laser light by the agglomerates have to be considered. So far, the agglomeration of nanoparticles upon dispersion in the photoresin or upon printing has not been studied systematically. Hence, to date, it is still challenging to assess whether the previously reported effects of NPs on the 3D printing process stem from interactions of individual noninteracting NPs or from NP agglomerates with the curing laser.

For the successful printing of a resin with individual nanoparticles in a TPP 3D printing process, we first ensured the dispersibility of NPs in the uncured resin. By modifying the surface with tailor-made acrylate surfactants, we enhanced the dispersibility in the photoresin, allowing for significantly increased NP loadings compared to pristine NPs. Three different types of NPs (see Figure 1) with complementary optical properties—Au NPs (diameter ∼1.7 nm), Ag NPs (diameter ∼1.8 nm) and CdSe/CdZnS core/shell NPLs (17 nm × 32 nm)—could be successfully used in the photoresin in volume concentrations between 0.0013 and 0.06 v/v%.

RESULTS AND DISCUSSION

Dispersion of Nanoparticles in the Uncured Resin. First, we assessed the dispersibility and colloidal stability in the uncured photoresin to allow for the homogeneous distribution of the NPs and to exclude effects caused by particle agglomerates. A commercial acrylate-based resin (IP-Dip, Nanoscribe) was used for the study. The resin consists of a mixture of multifunctional acrylates. Either the dispersion of NPs can be problematic, due to incompatible solubility of the nanoparticles' surfactants in the resin or agglomeration can occur through depletion forces induced by the oligomeric components in the photoresin.[28]

Pristine NPs are coated with dodecanethiol (Ag and Au NPs) or oleic acid (CdSe/CdZnS NPLs). To mix NPs with the photoresin different procedures are tested: (i) the NPs and the resin were both dissolved in dichloromethane (DCM) and mixed, the DCM is removed afterward, (ii) the NPs dispersed in DCM were mixed with the pure photoresin, the DCM is removed afterward, and (iii) dried NPs are mixed with undiluted photoresin. When pristine NPs are mixed with the photoresin, agglomeration occurs immediately independent of the mixing procedure. This is obvious for high loadings of NPs where agglomeration is macroscopically visible. At seemingly low loadings, particle−particle interactions could occur without being macroscopically visible. To test this in detail, we used the optical signal of Au NPs. Au NPs have distinctly

https://dx.doi.org/10.1021/acsami.0c14546
ACS Appl. Mater. Interfaces 2020, 12, 50834−50843

different absorption spectra when in close contact with neighboring NPs due to plasmonic coupling and a consequent red shift and broadening of the plasmon band.[29] Indeed, we observed a red shift and broadening of the absorption spectra agglomerates even for the NP-loading contents around 0.1 v/v % when Au NPs stabilized with dodecanethiol were used (see Figure 2a). This means that even though the sample seems

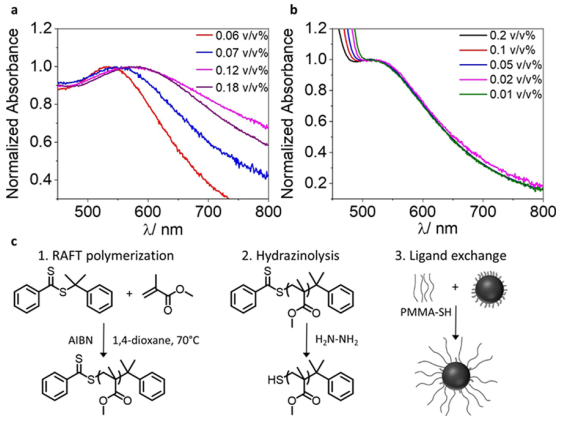

Figure 2. Absorption spectra of Au NPs stabilized with dodecanethiol (a) or PMMA-SH (b) dispersed in the IP-Dip photoresin. (a) Spectra broaden and red shift with increasing concentration, indicating the NP-concentration-dependent agglomeration tendency of Au NPs in the photoresin; (b) spectra are not shifted or broadened and no agglomeration is observed; and (c) reaction scheme of PMMA-SH synthesis and ligand exchange for particle modification.

optically clear to the eye, there is a significant particle−particle interaction and formation of agglomerates, which leads to altered optical properties of the final composite material. We note that depending on the degree of agglomeration, there should be significantly more interaction with the near infrared (NIR) laser with the Au NP-loaded photoresin. Hence, the TPP printing process will depend on the agglomeration degree of the NP in the photoresin. Since the dispersibility of the NPs depends on the solubility of the surfactant covering the NPs in the photoresin and pure dodecanethiol and oleic acid are not soluble in the photoresin, we conclude that the observed agglomeration of NPs is likely induced by the chemical incompatibility of the NP's surfactant shell with the photoresin. Having the surfactant of the same material as the photoresin should reduce the agglomeration tendency since both components, the surfactant and the photoresin, are chemically nearly identical. Thus, attractive forces between the NPs could be reduced. Indeed, the grafting of polymer chains of the same composition as the matrix is known to form a "brush" around the NPs and to decrease the attractive forces between the NPs.[30,31] Therefore, to obtain a better dispersibility of the NPs in the resin by minimizing the attractive forces between particles and enhance the compatibility of the NP's surfactant shell, the particles were modified with thiol-terminated poly(methyl methacrylate) (PMMA-SH) (M_n ~ 5000 g/mol) (see Methods for experimental details, see Figure S1 for the NMR spectrum). The synthesis of the polymer ligand is a two-step process, first reversible addition fragmentation chain transfer (RAFT) polymerization is used to polymerize the methyl methacrylate monomer (Figure 2c, left), and then the RAFT end group is cleaved by hydrazinolysis to obtain the thiol end group (Figure 2c, middle). Thiols are known to have a strong affinity to metals and are widely used as surfactants for metal NPs.[32−34] With a ligand exchange step, the pristine surfactants (oleic acid and dodecanethiol) are replaced by the PMMA-SH surfactant (see Figure 2c right, and Figure S18 for thermogravimetric analysis after ligand exchange). The plasmon resonance peak of the modified Au NPs does not shift upon dispersion in the resin, indicating a lack of agglomeration (see Figure 2b). Indeed, high volume percentages up to 0.8 v/v% are possible with no detectable agglomeration, and the loading content is only limited by an increase in viscosity, hampering the photoresin's processability. Thus, our strategy allows for significantly increased loading content and should generally be applicable to all other NP materials. Therefore, we used this method to modify Ag NPs and CdSe/CdZnS NPLs with the same polymeric surfactant and test the colloidal stability by absorption spectroscopy. Since the absorption band of Ag NPs overlaps with the absorption band of the resin (see Figure S2a) shifts of plasmon resonances are masked by the resin's absorption and CdSe/CdZnS NPL absorption features do not shift when agglomerated, we assess the dispersibility of Ag NPs and CdSe/CdZnS NPLs by checking for scattering contributions ($1/\lambda^4$) in the absorption spectra (see Figure S2). In both cases, we do not observe agglomeration, highlighting the general applicability of our strategy for eliminating depletion attraction forces leading to colloidally stable NPs in the photoresin even at high loading contents. After having solved this fundamental challenge, we study the influence of well-separated NPs embedded in the photoresin in the TPP 3D printing process.

Dispersion of Nanoparticles in 3D Printed Objects. Even if NPs are well dispersed in the uncured photoresin, the printing process could induce agglomeration or phase separation of the NPs, due to temperature gradients, viscosity changes, or shrinkage of the material. To assess this, we first estimate the diffusion rates of the NPs in the resin (see Table S2). For the following calculations, we assume continuous mode printing (10 mm/s) and the voxel diameter to be in the order of 350 μm in the $x-y$ plane (see Figure S9). With these assumptions, the dwell time of the laser per voxel is 0.03 ms; Au and Ag NP diffusion on average ~1.9 nm and CdSe/CdZnS NPLs ~0.62 nm within this time frame. For the chosen volume fractions of the PMMA-SH modified NPs (between 0.02 and 0.002 v/v% for Au NPs; between 0.013 and 0.0013 v/v% for Ag NPs; and between 0.06 and 0.013 v/v% for CdSe/CdZnS NPLs) the average center-to-center interparticle distance is between 45 and 125 nm for Au and Ag NPs and 250−435 nm for CdSe/CdZnS NPLs (see Figure S8). We further analyzed the composition of the pure photoresin by NMR spectroscopy (see Figure S11) and gel permeation chromatography (GPC, see Figure S10). ^{1}H NMR spectroscopy revealed that the resin is composed mainly of multifunctional acrylates for cross-linking (signals between 4 and 6.5 ppm) and that the photoinitiator (signals between 8 and 6.75 ppm) is present in high concentrations. This was further confirmed by GPC analysis, which shows only oligomeric macromolecules with a maximum molecular weight of ~1200 g/mol. This lets us conclude that TPP printing should lead to a high cross-linking density and little chain-growth toward higher molecular weight polymers. Due to the short dwell time, the resulting short diffusion distance and the high concentration of initiator molecules (see Figure S11), we thus expect that the NPs should be trapped in the resin by the

https://dx.doi.org/10.1021/acsami.0c14546
ACS Appl. Mater. Interfaces 2020, 12, 50834−50843

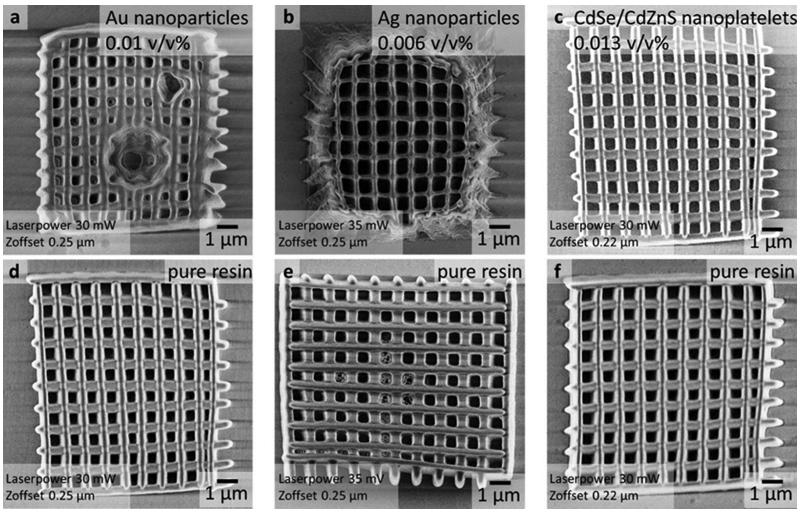

Figure 3. Scanning electron microscopy (SEM) micrographs of 3D printed woodpile structures with and without integrated NPs. (a) For the woodpile structure loaded with Au NPs, a strong tendency for thermal degradation in comparison to pure resin at the same printing parameters (d) is observable; (b) for the woodpile structure loaded with Ag NPs, polymerization and cross-linking are insufficient in comparison to pure resin (e); (c) woodpile structure loaded with CdSe/CdZnS nanoplatelets print nearly indistinguishably compared to the pure resin (f).

cross-linking before they can agglomerate to exerted attractive forces induced by the printing process.

To prove these assumptions, we assess the distribution of the PMMA-SH modified NPs in 3D printed pyramids (10 μm × 10 μm × 5 μm). After printing using a commercial TPP 3D printer (Photonic Professional GT2 photonic, Nanoscribe), we used a focused ion beam (FIB) to prepare a thin lamella (~100 nm) of the 3D printed pyramids (see Figure S12) embedded in a Pd matrix. We consecutively analyzed these lamellae using transmission electron microscopy (TEM). In all cases, the NPs (Au, Ag, and CdSe/CdZnS) are well separated and stochastically distributed inside the cured resin (see Figures S13–S16 for EDX). Since we know the thickness of our lamella and the visible area in our TEM micrographs, we could estimate the observable volume. Thus, by determining the number of NPs per TEM image we can estimate the volume concentration of the NPs integrated into the TPP 3D-printed resin (see the Supporting Information, Table S3). For all NP/polymer composites, the NP concentration estimated by TEM is in good agreement with the initial concentration in the photoresin. Thus, we can conclude that the printing process with PMMA-SH modified NPs does not lead to agglomeration or phase separation, e.g., at the surface of the printed structures. After having confirmed the colloidal stability of NPs in the photoresin and their stochastic distribution in the 3D-printed structure, we now discuss how the presence of the different types of NPs influences the printing process via absorption and radical quenching processes.

Effects of Nanoparticles on Stereolithographic TPP 3D Printing. In stereolithographic TPP 3D-printing, solidification of the photoresin is based on radical polymerization and the cross-linking of, e.g., acrylate-based monomers and oligomers.[35] Using a pulsed laser, the photoinitiator is activated via 2PA and radicals are formed allowing for radical polymerization and cross-linking. For sufficient laser power (LP), the generated radical concentration is sufficiently high and the resin is polymerized. On the one hand, if the absorbed energy in the volume where the polymerization is to occur, the so-called voxel (volume pixel), is too high, thermal degradation can occur. On the other hand, if the energy input in the voxel is too low, the polymerization does not start or is terminated prematurely, e.g., due to termination by dissolved oxygen.

By the integration of the NPs, the energy density can be affected in various ways. NPs can absorb the laser excitation either directly via 1PA (Au NPs) or via 2PA (Au and Ag NPs, and CdSe/CdZnS NPLs). Upon excitation, plasmonic NPs dissipate the absorbed energy in the form of heat, CdSe/CdZnS NPLs predominantly by the emission of photons. While both processes decrease the available photon flux in the voxel for activation of the initiator, the influence on the TPP 3D printing process is expected to be distinctly different. Heat dissipation can cause additional thermal degradation of the organic materials in the proximity of plasmonic NPs, while energy dissipation via fluorescence from semiconductor NPs such as CdSe/CdZnS should not hamper the integrity of the polymeric matrix material. Additionally, the large surface-to-volume ratio of NPs can lead to direct radical quenching when the radical-bearing (macro)molecules are in close proximity to the NPs' surfaces. To investigate these effects on the stereolithographic TPP 3D printing process, we printed and compared woodpile structures (10 μm × 10 μm; 1 μm spacing, 10 layers) with and without NPs at various laser powers and z-offsets (see Figure 3 and Figure S3). The z-offset determines the shift of the focal point along the surface normal. Within the tested parameter space, three regions can be identified: (i) the material is not or not well polymerized, (ii) the material shows a good printing quality, and (iii) thermal degradation of the material (see Figure S3). As expected, for the pure photoresin, a large variety of parameters allow for printing with good quality. Only at the highest laser power a tendency to thermal degradation of the material is observable. In the presence of Au NPs, a pronounced thermal decomposition is observed even for a relatively low laser power (see Figures 3a,d and S3). Only a small laser power and a small z-offset lead to a good printing result. In comparison to Au NP/photoresin composites, in the presence of Ag NPs, much higher laser powers are required to obtain a good printing result. Lower laser powers lead to incomplete polymerization and cross-linking (see Figure 3b,e).

https://dx.doi.org/10.1021/acsami.0c14546
ACS Appl. Mater. Interfaces 2020, 12, 50834−50843

In clear contrast to the plasmonic NPs, the integration of semiconductor CdSe/CdZnS NPLs does not change the useful printing parameter space significantly (see Figures 3c,f and S3). Hence, in summary of the above, plasmonic NPs require high laser powers to obtain fully polymerized structures, however, high laser powers could lead to thermal degradation. Thus, for a given laser power, only a small amount of plasmonic NPs in the photoresin will allow sufficient polymerization without thermal degradation. For semiconductor NPs the thermal degradation is less problematic since they dissipate absorbed light via fluorescence. This shows that the type of material embedded in the photoresin is important not only in terms of direct interaction with the excitation beam, which alters the voxel volume, but the secondary effects after excitation similarly play a crucial role and must be considered.

To characterize the effect of PMMA-SH stabilized NPs on the printing process more in detail, we analyzed the linewidth of the woodpile structures (see Figure 4). In all cases, the

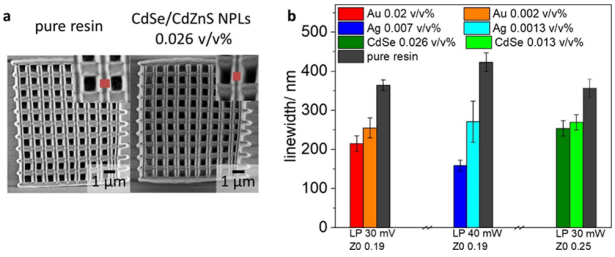

Figure 4. Decrease of the linewidth in the presence of NPs. (a) SEM micrograph of woodpile structures in the absence and the presence of CdSe/CdZnS NPLs (0.026 v/v%); (b) measured linewidths with all types of NPs at various concentrations.

presence of NPs decreases the linewidth significantly (28−62%). Furthermore, for all NPs increasing the NP concentration decreases the linewidth in a concentration-dependent manner (up to a 62% decrease). Notably, Ag NPs lead to the strongest effect. Here, even for relatively low volume fractions (0.007 v/v%), the decrease in linewidth of up to 62% is observed, whereas for the highest Au NPs (0.02 v/v%) and CdSe/CdZnS NPL concentrations (0.026 v/v%), the maximum decrease is 41 and 28%, respectively.

Interference of NPs with the Stereolithographic TPP 3D Printing Process. Depending on the NP material, we observed different onsets of effects on the printing. The main observations are (i) earlier thermal degradation of the resin in the presence of Au NPs, (ii) higher laser power required for the polymerization of the resin in the presence of Ag NPs in comparison to all other NP-loaded photoresins, and (iii) a general concentration-dependent tendency of decreasing the linewidth of the woodpile structures in the presence of all studied NPs. The NPs can mainly cause three different processes, which all affect the 3D printing process (see Scheme 1).

The NPs can absorb light, either by 2PA (mainly in or near the focal volume where the photon flux is sufficiently high. This happens for plasmonic NPs[20,22] and CdSe/CdZnS NPLs[21]) or 1PA if there is a direct spectral overlap of the NP absorption profile with the laser line (in the whole pathway of the laser beam). In our case, only Au NPs can undergo 1PA (see Figure 1 for absorption spectra, the red dashed line indicates the laser wavelength). For both types of absorption

Scheme 1. Interference Pathways of NPs with the TPP 3D Printing Process[a]

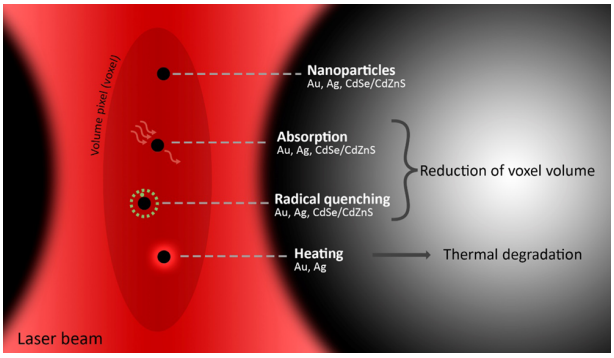

[a]NPs can absorb the laser light either via 1PA or 2PA, quench radicals created by the photoinitiator, and dissipation of the absorbed energy in the form of heat. Both absorption of laser light and quenching of radicals lead to a reduction of the voxel volume, while heating leads to thermal degradation of the material.

pathways, the absorption of light reduces the photon flux in the focal volume and therefore fewer radicals are generated. Thus, the voxel volume shrinks with increasing NP concentrations because the photon flux is not high enough to generate sufficient concentrations of radicals over a larger volume for radical polymerization. This directly leads to a reduction of the minimum printable linewidth while at the same time higher laser powers are required to generate enough radicals. Moreover, the absorption of light can induce heating of the Au and Ag NPs.[36] This explains the strong thermal decomposition of the resin in the presence of Au NPs since they absorb the laser light predominantly via direct 1PA. For Ag NPs the thermal decomposition effect is less prominent because fewer photons are absorbed since 2PA is a nonlinear effect that requires a high density of coherent photons (as found in the focal point, but not further away from the focus). Similarly, the semiconductor CdSe/CdZnS NPL-loaded photoresin leads to a reduction in the voxel volume due to 2PA in the focal spot. However, the energy is dissipated as fluorescence and thermal decomposition is mitigated. While these findings can explain our observation regarding the concentration-dependent reduction of the minimal printable feature size and the tendency for thermal decomposition of some NPs, other material specific effects play a similarly important role.

Besides the absorption of light, also direct interaction of the NPs with the radicals in their proximity is possible.[23−25] Indeed, radicals can be quenched simply by the presence of NPs. Thus, this effect can also reduce the voxel volume. This could be material specific in our case since for the three different NPs we observe different extents of printing linewidth reduction. We observe the strongest effect for Ag NPs and the weakest effect for CdSe/CdZnS NPLs. To analyze the quenching effect decoupled from the 1PA or 2PA absorption effect described above, we assessed the degree of conversion of methacrylate monomers by the conversion of the double bond in the NP-loaded photoresins relative to the pure resin under direct UV-light curing by Fourier transform infrared spectroscopy (FTIR, see the Supporting Information, Figures S4−S7). Here, the absorption of NPs does not hamper the photopolymerization significantly because the photoinitiators (and

https://dx.doi.org/10.1021/acsami.0c14546
ACS Appl. Mater. Interfaces 2020, 12, 50834−50843

the NPs present) are excited homogeneously throughout the sample directly via 1PA at high intensities. Thus, even in the presence of NPs there is always sufficient UV-light to excite the photoinitiator. Vibrational bands associated with CH_2=CH, C=O, and C−O groups,[37] could be assigned in all spectra. All spectra were normalized to the C=O peak (stemming from the carbonyl groups in the acrylate resin), since this signal remains constant during the polymerization reaction. The intensity of the bands assigned to the double bond decreases upon reaction (see Figure 5a). The degree of relative

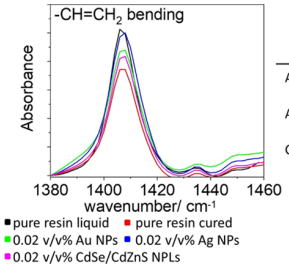

	Relative degree of conversion
Au NPs	10.9
Ag NPs	5.7
CdSe/CdZnS NPLs	56.9

Figure 5. Fourier transform infrared (FTIR) spectra of the cured and uncured resin with and without NPs. By comparing the integrated peak intensities of the C=O stretching and the C=C bending mode, the relative degree of conversion is determined.

conversion was calculated by comparing the −CH=CH_2 bending mode band to the C=O band before and after UV curing for the NP-loaded photoresins compared to the pure resin[37] (see Figure 5b and Table S1). The relative degree of conversion under UV-light is the highest for the resin loaded with CdSe/CdZnS NPLs (57%), followed by Au NP (11%) and Ag NP-loaded resins (6%). This finding is well in line with our observed trends of linewidth reduction as a function of the NP material. Our experiment shows that Ag NPs have the strongest direct radical quenching effect, followed by Au NPs and CdSe/CdZnS NPLs.

In addition to the different absorption behaviors and the quenching properties, the difference in the interparticle distance at a given volume fraction of NPs in the resin must also be taken into account. Since the size of the used NPs are different, the interparticle distance varied for the same volume concentration (see Figure S9). For the same volume concentration (0.013 v/v%), the interparticle distance of CdSe/CdZnS NPLs (436 nm) is much larger compared to Au NPs or Ag NPs (53 and 56 nm) (see Figure S8). Hence, the number of NPs in the voxel volume of CdSe/CdZnS NPLs is around 10 times smaller than for Au NPs and Ag NPs (see Figure S9) and the observed direct radical quenching effects are expected to be less prominent.

CONCLUSIONS

For the integration of plasmonic and semiconductor NPs in the stereolithographic 3D printing, we could successfully show how NPs can be stabilized in the uncured photoresin and how this stability can be maintained throughout the printing process. For stabilizing the NPs in the resin, a PMMA-SH polymer was used as the surfactant. Following this approach, all NPs studied could be dispersed without agglomeration in the uncured resin. Importantly, the colloidal stability was preserved throughout the printing process: the NPs do not agglomerate or phase separate since the cross-linking is much faster than the diffusion rate of the NPs, and therefore the NPs are trapped as isolated particles within the cured resin. Being certain that individual NPs and not agglomerates are printed in the NP/photoresin composites allowed us to study the influence of the NP material's properties on the TPP printing process in a concentration-dependent manner. For this, printed test structures were analyzed for their minimum feature size and three main conclusions can be drawn: (i) in the presence of Au NPs, strong thermal decomposition was observed due to their 1PA; (ii) in the presence of Ag NPs, the heating effect was less pronounced since Ag NPs can only absorb laser light via 2PA, but at the same time Ag NPs exhibit the highest tendency for direct radical quenching; (iii) the decrease of the linewidth for CdSe/CdZnS NPLs is to a large extent due to 2PA, mitigating at the same time thermal degradation due to dissipation of energy in the form of photoluminescence. This fundamental understanding of how to integrate NPs in the resin and how NPs interfere the printing must be considered when creating NP-enriched, functional polymeric structures via TPP 3D printing. Furthermore, our findings allow for increasing the printing resolution by adding NPs, leading to a reduction of the minimum feature size. Our results will allow for finer 3D-printed refractive optics utilizing the properties of the embedded noninteracting nanoparticles.

METHODS

Characterization. For optical spectroscopy, NP/NPL dispersions were transferred to a quartz glass cuvette (10 mm). The NP-loaded uncured resins were deposited on a glass slide and covered with a glass coverslip. Absorption spectra were recorded on a Cary 60 spectrophotometer. Photoluminescence spectra (for NPL dispersions) were recorded using a Prizmatix Silver high-power light-emitting diode (LED) (emission peak 369 nm) for excitation and an Avantes SensLine AvaSpec-HSC-TEC for data collection.

To analyze the printed structures using TEM, the samples were coated with a Pd layer and a thin lamella was prepared using a focused ion beam (FIB) system (FEI Nova 600 NanoLab FIB). Transmission electron microscopy was performed using a JEOL1400 or Tecnai FEI 20 microscope (acceleration voltage 120 and 200 kV, respectively). EDX spectra were recorded using an EDAX detector unit. The samples were deposited on carbon-coated copper grids (400 mesh) by drop-casting or using the focused ion beam. Scanning electron microscopy was performed on a Hitachi SU8000 with an acceleration voltage between 0.100 and 0.187 kV.

^{1}H NMR spectra were recorded with a Bruker Avance spectrometer operating at 300 MHz. The molecular mass of the IP-DIP resin was determined by GPC using a PSS SECcurity device (Agilent Technologies 1260 Infinity). The resin was dissolved in tetrahydrofuran (THF) and a calibration curve for PMMA in THF was applied.

ICP-OES measurements were performed with an ACTIVA M spectrometer (Horiba Jobin Yvon, Bernsheim, Germany) equipped with a Meinhardt-type nebulizer, a cyclone chamber, and controlled by ACTIVAnalyst 5.4 software. The forward plasma power was set at 1200 W, the Ar flow to 12 L/min, and the pump flow to 15 rpm. Measurements were performed three times per emission line, using three different elemental emission lines.

For the FTIR study, a drop of the uncured resin with and without nanoparticles was placed on a glass substrate and cured under a commercial UV-lamp (Model E0101, UV-A lamp type 3, 9 W) for 6 min. Afterward, the non-polymerized resin was washed away and a thin polymerized film remained. The film was analyzed using a Perkin Elmer Spectrum Bx IR spectrometer (16 scans).

Chemicals. 1-Octadecene (technical grade 90%, O806-1L), oleic acid (technical grade 90%, 364525-1L), cadmium nitrate tetrahydrate ($CdNO_3(H_2O)_4$, 98%, 642045-100G), zinc nitrate hydrate ($ZnNO_3(H_2O)$, 99.999%, 230006-25G), hydrochloric acid (puriss p.a. ≥37%), nitric acid (puriss p.a., 30709-1L-GL), 1,4-dioxane

https://dx.doi.org/10.1021/acsami.0c14546
ACS Appl. Mater. Interfaces 2020, 12, 50834−50843

(anhydrous, 99.8%), 2,2′-azobis(isobutyronitrile) (AIBN, 98%), propylene glycol methyl ether acetate (PGMEA) (99.5%), and methyl methacrylate (contains <30 ppm MEHQ as the inhibitor, 99%) were purchased from Sigma Aldrich. Cadmium acetate dihydrate ($Cd(OAc)_2(H_2O)_2$, 98%, 317131000) and sodium borohydride (99%) were purchased from Acros Organics. Selenium powder −200 mesh (Se, 99.999%, 36208), hydrazine monohydrate (98+%), and 1-octylamine (99%, B24193) were purchased from Alfa Aesar. Hexane (95% *n*-hexane, analytical reagent grade, H/0355/21), toluene (≥99.8%), tetrahydrofurane (THF) (analytical reagent grade, T/070/17), and dichloromethane (DCM) (HPLC grade) were purchased from Fisher Chemical. Chloroform, stabilized with amylene (100%, 83627.290) and absolute ethanol (20821.330) were purchased from VWR Chemicals. Thioacetamide (TAA, >98%, T0187) was purchased from TCI. Silver nitrate (≥99%) and NaOH 0.01 M were purchased from Roth. Gold acid ($HAuCl_4$ (99.9%-Au)) was purchased from STREM chemicals. Tetra-*n*-octyl ammonium bromide (TBOA) (for synthesis), 2-propanol (99.5%), and 1-dodecanethiol (for synthesis) were purchased from Merck. 2-Phenyl-2-propyl benzodithioate (95%) was purchased from Acros Pharmatech Limited. The printing resins (IP-D and IP-S) were purchased from Nanoscribe. Methyl methacrylate was passed through a column of inhibitor remover prior to use. All other chemicals were used without further purification.

Thiol-Terminated Poly(methyl methacrylate) (PMMA-SH). *Raft Polymerization of PMMA (PMMA-Raft).* The PMMA polymer was synthesized according to a described procedure by Roth et al.[38] 25 g (250 mmol) of methyl methacrylate, 1.36 g (5 mmol) of 2-phenyl-2-propyl benzodithioate, 102.5 mg (0.625 mmol) of AIBN, and 25 mL of freshly distilled dioxane were combined in a dry Schlenk flask, the mixture was degassed by three freeze−pump−thaw cycles and then heated at 70 °C for 9 h. The polymer (monomer conversion = 80%; M_n = 4727 g/mol, M_w/M_n = 1.49) was precipitated three times in cold methanol.

Hydrazinolysis (PMMA-SH). The RAFT group of the synthesized polymer was cleaved according to a slightly modified procedure by Fan et al.[39] The PMMA-Raft polymer (4.339 g, 0.92 mmol) was dissolved in dimethylformamide (DMF) (30 mL). The solution was degassed by three freeze−pump−thaw cycles. At RT, hydrazine monohydrate (0.4 mL, 8.23 mmol) was added. After stirring for 2 h at RT, the polymer was precipitated in excess of cold 1.2 M HCl aqueous solution. The product was filtered, washed several times with cold methanol and dried in vacuo at 45 °C overnight. The successful cleavage of the RAFT group was proven by NMR (see the SI 1).

Synthesis of Au NPs. Au NPs were synthesized by a liquid−liquid synthesis route according to a described procedure by Riedinger et al.[40] Briefly, $HAuCl_4$ (300 mg, 0.88 mmol) was dissolved in MilliQ water (25 mL). Tetraoctylammoniumbromide (TOAB) (2.17 g, 3.97 mmol) was dissolved in toluene (80 mL). Both solutions were combined in a 500 mL separation funnel and shaken for 5 min. The gold precursor was transferred from the aqueous phase to the organic phase indicated by a color change from colorless to dark red. After complete separation, the aqueous solution was discarded. The organic phase was transferred to a 250 mL flask. Under stirring, $NaBH_4$ (334 mg, 8.83 mmol) dissolved in 20 mL of MilliQ water was added dropwise to the organic phase. A color change from red to violet could be observed due to the reduction of Au^{3+} to Au^0. The suspension was stirred for 60 min and then transferred to a separation funnel. The suspension was washed once with 25 mL of 10 mM HCl, once with 25 mL of 10 mM NaOH, and four times with 25 mL of MilliQ water. The aqueous phase was discarded and the organic phase was stirred overnight.

To stabilize the nanoparticles further, either 1-dodecanethiol or a PMMA-SH polymer was used. To stabilize the nanoparticles with 1-dodecanethiol, 1-dodecanethiol (10 mL, 41.8 mmol) was added and the suspension was heated to 65 °C under stirring for 2 h. The suspension was centrifuged at 2000 rpm (416 rcf) for 5 min to remove bigger aggregates. The suspension was divided into four 50 mL centrifugation tubes and filled up with methanol to precipitate the NPs. The suspension was centrifuged at 2000 rpm (416 rcf) for 5 min. The precipitate was redispersed in 8 mL of chloroform. To functionalize the Au NPs with the PMMA-SH polymer, 10 mL of the Au NP containing suspension was mixed with the polymer (825 mg) and stirred for 30 min at RT. The suspension was heated up to 65 °C under stirring for 2 h. Then, it was stirred overnight at RT. The Au NPs were precipitated with methanol. The solution was kept in the fridge for several days and was then centrifuged at 2000 rpm (416 rcf) for 5 min. The precipitate was redispersed in DCM.

Synthesis of Ag NPs. Ag NPs were synthesized according to a slightly modified protocol of Niskanen et al.[41] The Ag NPs were stabilized with the synthesized thiol-terminated PMMA polymer. The polymer (0.189 g, 0.04 mmol) was dissolved in 200 mL of ethanol/THF (1:1 v/v). $AgNO_3$ (0.0679 g, 0.4 mmol) dissolved in 0.4 mL of MilliQ water and $NaBH_4$ (0.152 g, 4 mmol) dissolved in 1.6 mL of MilliQ water were added under stirring. Immediately after the addition, hexane was added to precipitate the formed Ag NPs. The suspension was centrifuged at 4000 rpm (1664 rcf) for 5 min and redispersed in DCM.

Synthesis of Core/Shell CdSe Nanoplatelets. *Synthesis of CdSe NPLs.* 4 monolayer (ML) thick CdSe NPLs were synthesized by a modified procedure published by Mahler et al.[42] Briefly, 60 mL of 1-octadecene, 320 mg (1.20 mmol) of $Cd(OAc)_2(H_2O)_2$, and 879 μL (787 mg, 2.79 mmol) of oleic acid were combined inside a 100 mL three-necked flask attached to a water-cooled condenser. The mixture was stirred and degassed under vacuum at 110 °C for 90 min. After stopping the vacuum line, the flask was filled with argon and 48 mg (0.607 mmol) of Se powder was swiftly added into the flask. Then, the temperature was set to 240 °C. When the temperature in the flask reached 205 °C, 160 mg (0.600 mmol) of $Cd(OAc)_2(H_2O)_2$ was added into the mixture and the reaction proceeded for 15 min at 240 °C. Afterward, the flask was cooled to room temperature using a water bath and 6.7 mL of oleic acid was injected. The mixture was centrifuged for 10 min at 5000 rpm (2599 rcf), the supernatant was discarded. Finally, the precipitated NPLs were redispersed in 12 mL of hexane.

Synthesis of CdSe/$Cd_{0.33}Zn_{0.67}S$ Core/Shell NPLs. The $Cd_{0.33}Zn_{0.67}S$ shell was synthesized using a one-pot method, modified from an existing procedure.[42] Briefly, 6 mL of the as-synthesized 4ML NPLs (with an optical density at 510 nm = 30) was added into a 50 mL round bottom flask containing a stir bar. In a separate flask, 300 mg (3.99 mmol) of TAA, 3 mL (18.2 mmol) of octylamine, and 9 mL of chloroform were gently mixed and then sonicated in an ultrasound bath until all of the TAA dissolved. The TAA solution was added to the NPL solution while stirring. After a couple of minutes, 500 μL of $CdNO_3$ solution (0.2 M in ethanol) and 1000 μL of $ZnNO_3$ solution (0.2 M in ethanol) were added into the mixture. The flask was sealed with a glass stopper and left to stir for 24 h under ambient conditions.

To be able to precipitate the NPLs, the mixture was first concentrated by evaporating a portion of the solvent using a rotary evaporator at approximately 280 mbar, 40 °C for a couple of minutes. Then, the concentrated mixture (volume approx. 15 mL) was centrifuged for 10 min at 8000 rpm (6654*g*), the supernatant was discarded, and the precipitated NPLs were resuspended in 15 mL of chloroform. To better stabilize the NPLs, 300 μL of $ZnNO_3$ solution (0.2 M in ethanol) and 600 μL of oleic acid were added into the NPL dispersion while stirring and the mixture was kept under ambient conditions for a couple of days for photoluminescence recovery.

To remove the excess oleic acid introduced in this step, methyl acetate was added to the chloroform dispersion of core/shell NPLs (in the ratio of chloroform:methyl acetate = 1:1 v/v). The NPLs were precipitated by centrifugation and redispersed in chloroform.

Surface Functionalization of CdSe/CdZnS NPLs with PMMA-SH. To modify the surface of the NPLs, PMMA-SH (7 mg) was mixed with the NPL dispersion (100 μL, 4.5 mg/mL, theoretical 23000 chains/nm^2) and stirred for 20 min at RT. Afterward, the mixture was heated up to 60 °C under stirring for 1 h. The mixture was allowed to cool down to room temperature and stirred for an additional 20 min. Afterward, methanol was added (methanol:reaction mixture 1:2 v/v) to precipitate the NPLs. The precipitate was centrifuged at 6500 rpm (4393 rcf) for 5 min and redispersed in 100 μL of DCM.

https://dx.doi.org/10.1021/acsami.0c14546
ACS Appl. Mater. Interfaces 2020, 12, 50834−50843

Adjustment of the Concentration of the Nanoparticle Dispersion. To determine the concentration of Au NPs and Ag NPs, ICP-OES was performed to determine the concentration of metals. Therefore, the dried NPs (Au and Ag) were dissolved in aqua regia and later diluted with MilliQ water, to reach a metal concentration range between 2 and 20 mg/L. The concentration of the Au and Ag NP dispersions were set to 10 mg/mL. The concentration of the NPL dispersion was determined by measuring the absorbance and applying a calibration curve (absorbance vs determined weight concentration by ICP). Therefore, the concentration of core/shell NPLs were measured using ICP-OES.[43] The weight concentration of the NPLs in dispersion can be calculated by adding the metal ion concentration measured by ICP to Se and S concentration based on the stoichiometry

$$\text{NPL concentration}\left(\frac{\text{mg}}{\text{mL}}\right) = \text{measured } Cd^{2+}\text{concentration} + \text{measured } Zn^{2+}\text{ concentration} + \text{estimated } Se^{2-}\text{concentration} + \text{estimated } S^{2-}\text{concentration}$$

Dispersion of NPs in the Resin. The resin was diluted in DCM (1 mL of resin in 1 mL of DCM) to lower the viscosity. A certain volume of the NPs/NPL dispersion was added to reach a set final concentration (see Table 1). To facilitate the dispersion of the flat CdSe/CdZnS NPLs, the dispersion was diluted and the resin was slightly heated. After mixing using a vortex mixer, the solvents were removed using a rotary evaporator. The prepared resins were stored in the dark at 5 °C in the fridge.

Table 1. NPs/NPLs Dispersed in the Resin for 3D Printing in Various Concentrations

Ag NPs in IP-Dip (v/v%)	Au NPs in IP-Dip (v/v%)	CdSe/CdZnS NPLs in IP-Dip (v/v%)
0.013	0.02	0.06
0.007	0.01	0.026
0.0013	0.002	0.013

Printing with a Nanoscribe 3D Printer. The structures printed were pyramids and woodpile structures. All were fabricated using a NanoScribe Photonic Professional (GT) 3D-printer. To start printing a desired structure, it is needed to either convert a 3D-model (in. stl format) into a printer-readable format or directly program a printer-readable file. Both can be done using software DeScribe, which is supplied by NanoScribe GmbH. The pyramids were processed from an already existing. stl file, whereas the woodpile structures were directly programmed. The woodpile structure is composed of 10 stacked layers. Each layer has 15 consecutive parallel lines, each 1 μm apart from each other, and each consecutive layer is rotated by 90°, creating a grid. The pyramid array consists of nine square pyramids, each having a dimension of 10 μm × 10 μm × 5 μm. The structures were printed inside a droplet of negative photoresin (IP-Dip) using dip-in laser lithography (DiLL), where the objective is immersed directly onto the photoresin. The 63× N.A 1.4 immersion objective and 700 μm thick fused silica slide as the substrate was used. Afterward, the excess photoresin was rinsed off of the structure via immersion in propylene glycol methyl ether acetate (PGMEA) for 30 min, followed by immersion in isopropanol for 5 min and gentle drying with nitrogen flow. Depending on the structure, shape, and size, different parameters must be used for printing: the laser power (LP) determines the size of the individual voxels that compose the structure, which in turn determines the minimum in-plane distance each printed line must have. If the distance between the lines is too short, bubbles appear on the printed area due to local overheating,[44] destroying the sample. If the distance is too large, the lines are unconnected. This is desirable in the in-plane direction for the woodpile structure, but not for the "continuous" pyramid. On the vertical axis, on both cases connected voxels are desired. If they are not properly connected, the voxels will float on the uncured resin and be washed away alongside the excess resin during the development process. On the continuous structures, the in-plane line distance is governed by the hatching distance (HD) parameter, which gives the distance in micrometers that the center of two consecutive lines will be spaced apart. The vertical distance between two voxels is controlled by the slicing distance (SD) parameter, whereas for the woodpile and grating structures this is controlled by the z-offset parameter. Since the voxel size not only depends on the LP, but also on the photoresin and NP loading, a parameter sweep of not only voxel distances, but also LP is needed for each NP-doped photoresin.

■ ASSOCIATED CONTENT

Supporting Information

The Supporting Information is available free of charge at https://pubs.acs.org/doi/10.1021/acsami.0c14546.

General scheme of TPP 3D printing; NMR of the PMMA polymer; further characterization of modified nanoparticles (TEM and spectroscopy); further characterization of printed objects (SEM, TEM, EDX, and IR); estimations of the interparticle distance; diffusion length and voxel volume; characterization of the photoresin (GPC, NMR) (PDF)

■ AUTHOR INFORMATION

Corresponding Authors

Katharina Landfester − *Max Planck Institute for Polymer Research, 55128 Mainz, Germany;* orcid.org/0000-0001-9591-4638; Email: landfester@mpip-mainz.mpg.de

Andreas Riedinger − *Max Planck Institute for Polymer Research, 55128 Mainz, Germany;* orcid.org/0000-0002-7732-0606; Email: riedinger@mpip-mainz.mpg.de

Authors

Rebecca Momper − *Max Planck Institute for Polymer Research, 55128 Mainz, Germany*

Antonio Ibanez Landeta − *Max Planck Institute for Dynamics and Self-Organization, 37077 Göttingen, Germany*

Long Yang − *Max Planck Institute for Polymer Research, 55128 Mainz, Germany*

Henry Halim − *Max Planck Institute for Polymer Research, 55128 Mainz, Germany*

Heloise Therien-Aubin − *Max Planck Institute for Polymer Research, 55128 Mainz, Germany;* orcid.org/0000-0003-4567-516X

Eberhard Bodenschatz − *Max Planck Institute for Dynamics and Self-Organization, 37077 Göttingen, Germany*

Complete contact information is available at: https://pubs.acs.org/10.1021/acsami.0c14546

Author Contributions

R.M., A.R., and K.L. conceived the project. Syntheses were performed by R.M., L.Y., and H.H. 3D printing was performed by R.M. and A.I.L. Characterization of 3D printed structures were performed by R.M., A.R., and K.L. wrote the manuscript. All authors contributed to the discussion of the results and to the revision of the manuscript.

Notes

The authors declare no competing financial interest.

https://dx.doi.org/10.1021/acsami.0c14546
ACS Appl. Mater. Interfaces 2020, 12, 50834−50843

■ ACKNOWLEDGMENTS

The authors are grateful for the financial support of the Max Planck Center for Complex Fluid Dynamics. H.H. was supported by a fellowship from the Max Planck Graduate Center (MPGC), Mainz, Germany. We thank Gunnar Glasser and Katrin Kirchhoff for help with electron microscopy, Maren Müller for the preparation of the TEM lamella, and Anke Kaltbeitzel and Andreas Best for help with optical microscopy.

■ REFERENCES

(1) Manapat, J. Z.; Chen, Q.; Ye, P.; Advincula, R. C. 3D Printing of Polymer Nanocomposites via Stereolithography. *Macromol. Mater. Eng.* **2017**, *302*, No. 1600553.
(2) Sugioka, K.; Cheng, Y. Femtosecond Laser Three-Dimensional Micro- and Nanofabrication. *Appl. Phys. Rev.* **2014**, *1*, No. 041303.
(3) Straub, M.; Nguyen, L. H.; Fazlic, A.; Gu, M. Complex-shaped Three-Dimensional Microstructures and Photonic Crystals Generated in a Polysiloxane Polymer by Two-Photon Microstereolithography. *Opt. Mater.* **2004**, *27*, 359−364.
(4) Malinauskas, M.; Žukauskas, A.; Purlys, V.; Gaidukevičiūtė, A.; Balevičius, Z.; Piskarskas, A.; Fotakis, C.; Pissadakis, S.; Gray, D.; Gadonas, R.; Vamvakaki, M.; Farsari, M. 3D Microoptical Elements formed in a Photostructurable Germanium Silicate by Direct Laser Writing. *Opt. Lasers Eng.* **2012**, *50*, 1785−1788.
(5) Schizas, C.; Melissinaki, V.; Gaidukeviciute, A.; Reinhardt, C.; Ohrt, C.; Dedoussis, V.; Chichkov, B. N.; Fotakis, C.; Farsari, M.; Karalekas, D. On the Design and Fabrication by Two-Photon Polymerization of a readily Assembled Micro-Valve. *Int. J. Adv. Manuf. Technol.* **2010**, *48*, 435−441.
(6) Danilevicius, P.; Rezende, R. A.; Pereira, F. D. A. S.; Selimis, A.; Kasyanov, V.; Noritomi, P. Y.; Silva, J. V. L. d.; Chatzinikolaidou, M.; Farsari, M.; Mironov, V. Burr-like, laser-made 3D Microscaffolds for Tissue Spheroid Encagement. *Biointerphases* **2015**, *10*, No. 021011.
(7) Sakellari, I.; Kabouraki, E.; Gray, D.; Purlys, V.; Fotakis, C.; Pikulin, A.; Bityurin, N.; Vamvakaki, M.; Farsari, M. Diffusion-Assisted High-Resolution Direct Femtosecond Laser Writing. *ACS Nano* **2012**, *6*, 2302−2311.
(8) Ovsianikov, A.; Chichkov, B. N. Two-Photon Polymerization—High Resolution 3D Laser Technology and Its Applications. In *Nanoelectronics and Photonics: From Atoms to Materials, Devices, and Architectures*; Korkin, A.; Rosei, F., Eds.; Springer New York: New York, NY, 2008; pp. 427−446.
(9) Carlotti, M.; Mattoli, V. Functional Materials for Two-Photon Polymerization in Microfabrication. *Small* **2019**, *15*, No. 1902687.
(10) Leigh, S. J.; Bradley, R. J.; Purssell, C. P.; Billson, D. R.; Hutchins, D. A. A Simple, Low-Cost Conductive Composite Material for 3D Printing of Electronic Sensors. *PLoS One* **2012**, *7*, No. e49365.
(11) Ceylan, H.; Yasa, I. C.; Yasa, O.; Tabak, A. F.; Giltinan, J.; Sitti, M. 3D-Printed Biodegradable Microswimmer for Theranostic Cargo Delivery and Release. *ACS Nano* **2019**, *13*, 3353−3362.
(12) Marino, A.; Barsotti, J.; de Vito, G.; Filippeschi, C.; Mazzolai, B.; Piazza, V.; Labardi, M.; Mattoli, V.; Ciofani, G. Two-Photon Lithography of 3D Nanocomposite Piezoelectric Scaffolds for Cell Stimulation. *ACS Appl. Mater. Interfaces* **2015**, *7*, 25574−25579.
(13) Farahani, R. D.; Dubé, M.; Therriault, D. Three-Dimensional Printing of Multifunctional Nanocomposites: Manufacturing Techniques and Applications. *Adv. Mater.* **2016**, *28*, 5794−5821.
(14) Jonušauskas, L.; Lau, M.; Gruber, P.; Gökce, B.; Barcikowski, S.; Malinauskas, M.; Ovsianikov, A. Plasmon assisted 3D Microstructuring of Gold Nanoparticle-doped Polymers. *Nanotechnology* **2016**, *27*, No. 154001.
(15) Jonušauskas, L.; Varapnickas, S.; Rimšelis, G.; Malinauskas, M. In *Plasmonically Enhanced 3D Laser Lithography for High-Throughput Nanoprecision Fabrication*, SPIE LASE San Francisco, 2017.
(16) Ueno, K.; Juodkazis, S.; Shibuya, T.; Mizeikis, V.; Yokota, Y.; Misawa, H. Nanoparticle-Enhanced Photopolymerization. *J. Phys. Chem. C* **2009**, *113*, 11720−11724.
(17) Murazawa, N.; Ueno, K.; Mizeikis, V.; Juodkazis, S.; Misawa, H. Spatially Selective Nonlinear Photopolymerization Induced by the Near-Field of Surface Plasmons Localized on Rectangular Gold Nanorods. *J. Phys. Chem. C* **2009**, *113*, 1147−1149.
(18) Peng, Y.; Jradi, S.; Yang, X.; Dupont, M.; Hamie, F.; Dinh, X. Q.; Sun, X. W.; Xu, T.; Bachelot, R. 3D Photoluminescent Nanostructures Containing Quantum Dots Fabricated by Two-Photon Polymerization: Influence of Quantum Dots on the Spatial Resolution of Laser Writing. *Adv. Mater. Technol.* **2019**, *4*, No. 1800522.
(19) Liu, Y.; Xiong, W.; Li, D. W.; Lu, Y.; Huang, X.; Liu, H.; Fan, L. S.; Jiang, L.; Silvain, J.-F.; Lu, Y. F. Precise Assembly and Joining of Silver Nanowires in Three Dimensions for highly conductive Composite Structures. *Int. J. Extreme Manuf.* **2019**, *1*, No. 025001.
(20) Bhushan, B.; Kundu, T.; Singh, B. P. Two-photon Absorption Spectrum of Silver Nanoparticles. *Opt. Commun.* **2012**, *285*, 5420−5424.
(21) Scott, R.; Achtstein, A. W.; Prudnikau, A.; Antanovich, A.; Christodoulou, S.; Moreels, I.; Artemyev, M.; Woggon, U. Two Photon Absorption in II−VI Semiconductors: The Influence of Dimensionality and Size. *Nano Lett.* **2015**, *15*, 4985−4992.
(22) Olesiak-Banska, J.; Waszkielewicz, M.; Obstarczyk, P.; Samoc, M. Two-photon Absorption and Photoluminescence of Colloidal Gold Nanoparticles and Nanoclusters. *Chem. Soc. Rev.* **2019**, *48*, 4087−4117.
(23) Zhang, Z.; Berg, A.; Levanon, H.; Fessenden, R. W.; Meisel, D. On the Interactions of Free Radicals with Gold Nanoparticles. *J. Am. Chem. Soc.* **2003**, *125*, 7959−7963.
(24) Chappell, M. A.; Miller, L. F.; Price, C. L. Reversible Exchange of Stable Nitroxyl Radicals on Nanosilver Particles. *Environ. Chem.* **2015**, *12*, 198−203.
(25) Maurel, V.; Laferrière, M.; Billone, P.; Godin, R.; Scaiano, J. C. Free Radical Sensor Based on CdSe Quantum Dots with Added 4-Amino-2,2,6,6-Tetramethylpiperidine Oxide Functionality. *J. Phys. Chem. B* **2006**, *110*, 16353−16358.
(26) Kumar, S. K.; Krishnamoorti, R. Nanocomposites: Structure, Phase Behavior, and Properties. *Annu. Rev. Chem. Biomol. Eng.* **2010**, *1*, 37−58.
(27) Schaefer, D. W.; Justice, R. S. How Nano Are Nanocomposites? *Macromolecules* **2007**, *40*, 8501−8517.
(28) Asakura, S.; Oosawa, F. On Interaction between Two Bodies Immersed in a Solution of Macromolecules. *J. Chem. Phys.* **1954**, *22*, 1255−1256.
(29) Wei, Q. H.; Su, K. H.; Durant, S.; Zhang, X. Plasmon Resonance of Finite One-Dimensional Au Nanoparticle Chains. *Nano Lett.* **2004**, *4*, 1067−1071.
(30) Corbierre, M. K.; Cameron, N. S.; Sutton, M.; Laaziri, K.; Lennox, R. B. Gold Nanoparticle/Polymer Nanocomposites: Dispersion of Nanoparticles as a Function of Capping Agent Molecular Weight and Grafting Density. *Langmuir* **2005**, *21*, 6063−6072.
(31) Smith, G. D.; Bedrov, D. Dispersing Nanoparticles in a Polymer Matrix: Are Long, Dense Polymer Tethers Really Necessary? *Langmuir* **2009**, *25*, 11239−11243.
(32) Zhao, P. X.; Li, N.; Astruc, D. State of the Art in Gold Nanoparticle Synthesis. *Coord. Chem. Rev.* **2013**, *257*, 638−665.
(33) Battocchio, C.; Meneghini, C.; Fratoddi, I.; Venditti, I.; Russo, M. V.; Aquilanti, G.; Maurizio, C.; Bondino, F.; Matassa, R.; Rossi, M.; Mobilio, S.; Polzonetti, G. Silver Nanoparticles Stabilized with Thiols: A Close Look at the Local Chemistry and Chemical Structure. *J. Phys. Chem. C* **2012**, *116*, 19571−19578.
(34) Rogach, A. L.; Kornowski, A.; Gao, M.; Eychmüller, A.; Weller, H. Synthesis and Characterization of a Size Series of Extremely Small Thiol-Stabilized CdSe Nanocrystals. *J. Phys. Chem. B* **1999**, *103*, 3065−3069.
(35) Bagheri, A.; Jin, J. Photopolymerization in 3D Printing. *ACS Appl. Polym. Mater.* **2019**, *1*, 593−611.
(36) Govorov, A. O.; Richardson, H. H. Generating Heat with Metal Nanoparticles. *Nano Today* **2007**, *2*, 30−38.

https://dx.doi.org/10.1021/acsami.0c14546
ACS Appl. Mater. Interfaces 2020, 12, 50834−50843

(37) Liu, Y.; Campbell, J. H.; Stein, O.; Jiang, L.; Hund, J.; Lu, Y. Deformation Behavior of Foam Laser Targets Fabricated by Two-Photon Polymerization. *Nanomaterials* **2018**, *8*, 498.
(38) Roth, P. J.; Kessler, D.; Zentel, R.; Theato, P. A Method for Obtaining Defined End Groups of Polymethacrylates Prepared by the RAFT Process during Aminolysis. *Macromolecules* **2008**, *41*, 8316−8319.
(39) Fan, Z.; Serrano, M. K.; Schaper, A.; Agarwal, S.; Greiner, A. Polymer/Nanoparticle Hybrid Materials of Precise Dimensions by Size-Exclusive Fishing of Metal Nanoparticles. *Adv. Mater.* **2015**, *27*, 3888−3893.
(40) Riedinger, A.; Zhang, F.; Dommershausen, F.; Röcker, C.; Brandholt, S.; Nienhaus, G. U.; Koert, U.; Parak, W. J. Ratiometric Optical Sensing of Chloride Ions with Organic Fluorophore−Gold Nanoparticle Hybrids: A Systematic Study of Design Parameters and Surface Charge Effects. *Small* **2010**, *6*, 2590−2597.
(41) Niskanen, J.; Shan, J.; Tenhu, H.; Jiang, H.; Kauppinen, E.; Barranco, V.; Picó, F.; Yliniemi, K.; Kontturi, K. Synthesis of Copolymer-Stabilized Silver Nanoparticles for Coating Materials. *Colloid Polym. Sci.* **2010**, *288*, 543−553.
(42) Mahler, B.; Nadal, B.; Bouet, C.; Patriarche, G.; Dubertret, B. Core/Shell Colloidal Semiconductor Nanoplatelets. *J. Am. Chem. Soc.* **2012**, *134*, 18591−18598.
(43) Halim, H.; Simon, J.; Lieberwirth, I.; Mailaender, V.; Koynov, K.; Riedinger, A. Water-dispersed Semiconductor Nanoplatelets with high fluorescence Brightness, chemical and colloidal Stability. *J. Mater. Chem. B* **2020**, *8*, 146−154.
(44) Guney, M. G.; Fedder, G. K. Estimation of Line Dimensions in 3D Direct Laser Writing Lithography. *J. Micromech. Microeng.* **2016**, *26*, No. 105011.

https://dx.doi.org/10.1021/acsami.0c14546
ACS Appl. Mater. Interfaces 2020, 12, 50834−50843